Starting from the voltaic pile explored by Alessandro Volta around 1800, continuous improvements in batteries led to the use of rechargeable *Nickel Cadmium alkaline batteries* developed in the 1960s and modern-day *Nickel-metal hydride (NiMH)* and *lithium-ion batteries* in the 1990s. Figure 4.1 shows the energy density of various types of batteries. Note that batteries typically have an energy density that is at least one to two orders of magnitude smaller than that of liquid fuels like gasoline (13000 Wh/kg, 9500 Wh/l).

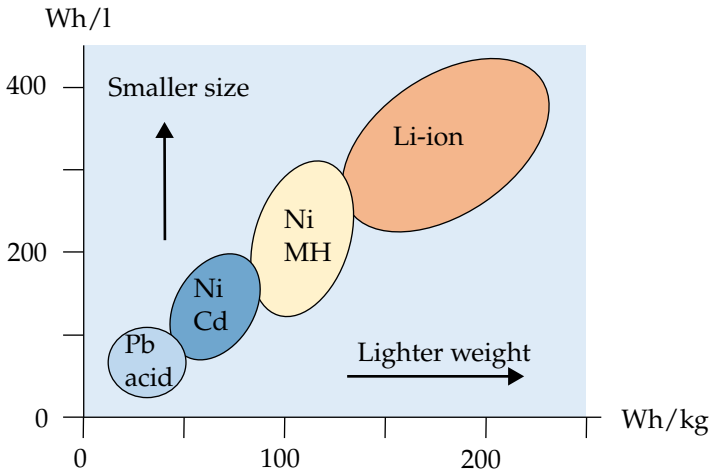

Figure 4.1: *Specific energy density [Wh/kg] as a function of volumetric energy density [Wh/l]. Along the horizontal axis, a higher energy density indicates lighter batteries; along the vertical axis, a higher energy density indicates that batteries can be made smaller.*

Often, liquid binary electrolytes are used in batteries, including:

- Potassium hydroxide (K^+OH^-) in alkaline (Zn/MnO_2), Ni-Cd, and Ag-Zn batteries
- Sulphuric acid ($(H^+)_2SO_4^{2-}$) in lead-acid batteries, and
- Lithium hexafluorophosphate ($Li^+PF_6^-$) in Li-ion batteries

State-of-the-art lithium-ion batteries use an electrolyte like $LiPF_6$ in an organic solvent, a $LiCoO_2$ cathode, and a carbon graphite anode with reactions that can be represented during discharging as, at the anode[1]

[1]Note that during discharging, oxidation takes place at the anode and reduction at the cathode, as in any other electrochemical cell. However, in batteries, the anode and cathode during discharging remain the anode and cathode during charging. Therefore, only during the charging of batteries can oxidation take place at the cathode and reduction at the anode.

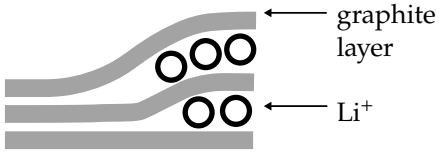

Figure 4.2: *The intercalation of Lithium ions between graphene layers inside an electrode. The intercalation process is alternated with de-intercalation, in which the Lithium ions move out again, which gives Li-ion batteries their nickname 'rocking-chair batteries'.*

$$C_6Li_x \underset{\text{charge}}{\overset{\text{disch.}}{\rightleftharpoons}} xLi^+ + C_6 + xe^-, \qquad \text{(anode)} \qquad (4.1)$$

$$Li_{1-x}CoO_2 + xLi^+ + xe^- \underset{\text{charge}}{\overset{\text{disch.}}{\rightleftharpoons}} LiCoO_2. \qquad \text{(cathode)} \qquad (4.2)$$

The fractional reaction stoichiometry x indicates the number of Lithium ions per carbon atom that is integrated into the layered graphite structure through a process called *intercalation* or *insertion*, see Fig. 4.2.

In an alkaline battery, the following redox reaction takes place

$$Zn + 2OH^- \underset{\text{charge}}{\overset{\text{disch.}}{\rightleftharpoons}} ZnO + H_2O + 2e^- \qquad \text{(anode)} \qquad (4.3)$$

$$2MnO_2 + 2H_2O(l) + 2e^- \underset{\text{charge}}{\overset{\text{disch.}}{\rightleftharpoons}} 2MnO(OH) + 2OH^-. \qquad \text{(cathode)} \qquad (4.4)$$

4.1.2 Battery terminology

Battery researchers have their own terminology and conventions, sometimes somewhat different from other parts of electrochemistry and electrochemical engineering fields. Here, we list some of the definitions and terms we will use later on.

1. **Cut-off voltage** (V_d): the voltage below which the battery is considered empty or discharged; hence the subscript d. Below this voltage, the battery can no longer be used satisfactorily for the intended application; further discharging may even damage the battery.

2. **Theoretical capacity** ($Q_{\max}$): The maximum "charge" the battery can hold. The battery is electrically neutral, but this indicates the amount of charge that can be maximally converted through redox reactions. Often units of Ampere-hours are used (1 Ah = 3600 A s = 3600 C) instead of C, the Coulomb.

3. **Volumetric theoretical capacity** ($q_{\max}$): Maximum charge per unit volume. Considering only a single porous electrode volume, we can write $q_{\max} = \frac{Q_{\max}}{AL}$, with A the separator area and L the electrode thickness.

4. **Discharge time** (t_{d}): The time required for a full discharge, until the cut-off voltage is reached.

5. **Discharge rate (C/#)**: A measure of how long it takes to discharge a battery from its maximum theoretical capacity. This is often expressed as a C rate. For example, a rate of C/3 means the battery is discharged in 3 hours and 3C means a full discharge in 20 minutes. Using a similar notation, the charging rate is sometimes expressed as an E rate.

6. **Current density** (j): Rarely used when describing batteries; its average value can be related to the 'actual' battery capacity $Q \leq Q_{\max}$ and the discharge time through

$$j = \frac{Q}{At_{\mathrm{d}}} = \frac{qL}{t_{\mathrm{d}}} = \frac{q_{\max}L}{3600N}. \tag{4.5}$$

7. **State of charge** (SOC): Represents the amount of charge stored, as a fraction of the theoretical capacity $Q_{\max}$. We will use the symbol $\mathrm{S_{oC}}$, where,

$$\mathrm{S_{oC}}(t) = 1 - A\frac{\int_0^t j\,dt}{Q_{\max}} = 1 - \frac{1}{L}\frac{\int_0^t j\,dt}{q_{\max}}. \tag{4.6}$$

8. **Terminal voltage** (V_{cell}): This is the voltage between the positive and negative terminals of a battery. For a single electrochemical cell or cells in parallel, this is equal to the cell voltage, so we will use the same notation as before. It is a multiple of the cell voltage for batteries consisting of several cells in series. The terminal voltage is not to be confused with the cut-off voltage.

9. **Energy density**: The maximum available energy per unit volume or unit mass of the battery. Often units of Wh = 1 W·3600s = 3600 J are used instead of Joules. Hence, common units for energy density are Wh/l or Wh/kg, for *volumetric* and *gravimetric* energy density (*specific energy*), respectively.

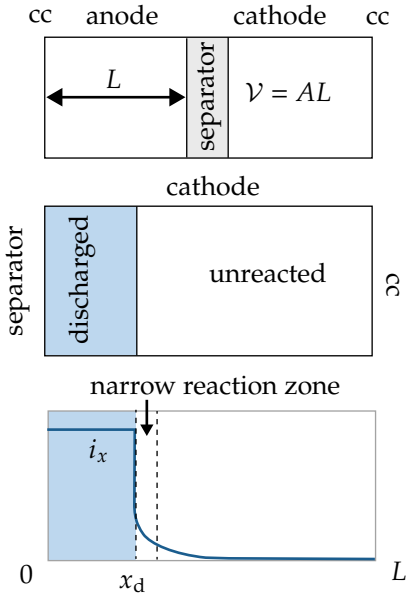

Figure 4.3: *The typical battery layout considered (top), an electrode separated in distinct discharged and unreacted parts in the reaction zone model (middle), and the distribution of ionic current i_x in an example cathode assuming $j \gg J_\kappa$. The fraction of reacted material is equal to the dimensionless position of the reaction zone x_d/L.*

4.2 Moving reaction zone model

4.2.1 Assumptions

We consider a porous battery electrode with negligible electrode resistivity but significant ohmic limitations in the electrolyte. We assume a constant electrolyte conductivity κ.[2] In the terminology of Chapter 3, we consider the case $j \gg J_\kappa = b\kappa/L$ so, by Eq. (3.66), the effectiveness factor $\mathcal{E} \ll 1$. This implies that the reaction takes place primarily over a reaction zone with a thickness equal to the penetration depth $\mathcal{E}L \ll L$. This allows us to split the discharging battery electrode into three zones, with the thin reaction zone demarcating discharged and not yet discharged zones as shown in Figure 4.3.[3] A *moving reaction zone model* based on this idealisation was developed in Ref. [27].

[2]Commonly in batteries, the metal electrodes allow a high conductivity for electrons. At the same time, there are large research efforts to develop electrolytes with sufficiently high ionic conductivity. *Solid-state batteries* use solid electrolytes, which may approximately satisfy Ohm's law, as considered here.

[3]We will in this chapter generally talk about discharging, while the descriptions equally apply to charging. We will also only consider a single electrode at a time to keep the notation minimal. It will usually be straightforward to add the second electrode in the same manner.

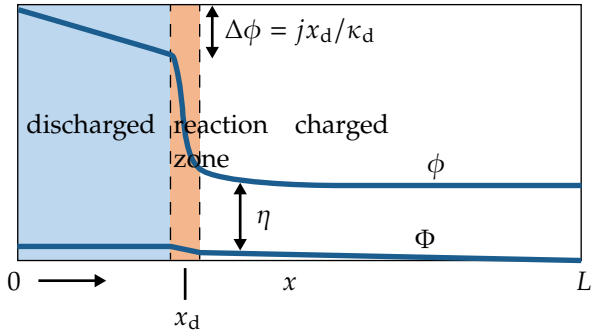

Figure 4.4: *Distribution of ionic and electronic potential ϕ and Φ respectively, with the voltage drop $\Delta\phi$ due to ohmic resistance over the discharged region and the strong drop in activation overpotential in the reaction zone.*

4.2.2 The terminal voltage

We will write the cell voltage using Eqs. (3.39) and (1.35) as

$$V_{\text{cell}} = V_{\text{eq}} - \Delta V - \Delta\phi, \tag{4.7}$$

where[4]

$$\Delta V = \eta_{\text{a0}} - \eta_{\text{a0}} + ARj. \tag{4.8}$$

Figure 4.4 shows the distributions of potentials inside a porous battery electrode with a sharp, moving reaction zone front. There is no reaction over the discharged region so, by Ohm's law in the form of Eq. (1.8), the ionic potential drop up to the reaction zone reads:

$$\Delta\phi = \frac{jx_d}{\kappa_d}, \tag{4.9}$$

where x_d is the thickness of the discharged layer and κ_d is the effective ionic conductivity of the discharged material.[5]

Figure 4.5 shows the cell voltage as a function of the discharged layer thickness x_d. When x_d approaches the electrode thickness L and little reactive material is left, the activation losses will increase, causing the strong decrease in terminal voltage depicted in Fig. 4.5. At a cut-off voltage V_d, the battery is considered discharged for practical purposes. The final state of charge will typically be non-zero because some capacity remains left, which can be used at a lower current.

[4]In Eq. (1.35), we reserved ΔV for just electronic losses in the electrodes, cables, etcetera. Here, in ΔV, we also include the activation losses and ionic ohmic losses in the membrane. Since we assume $j \gg J_\kappa$, Eq. (3.65) can be used to give the overpotential at the beginning of the reaction zone. Strictly speaking, this will cease to hold when the reaction zone comes very close to the right boundary, requiring $S_{oC} \geq 2J_\kappa/j$.

[5]Note that since the reaction in a battery involves the solid electrode material, the porosity may change due to the reaction, changing the ionic conductivity compared to that in the unreacted electrode material.

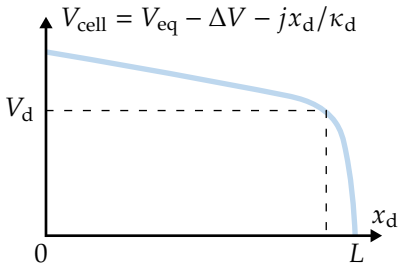

Figure 4.5: *The terminal voltage V_{cell} as a function of the position x_{d} of the reaction zone. Ideally, the cut-off voltage (V_{d}) is reached when x_{d} approaches L at the end of the porous electrode. In reality, the activation losses start to increase when x_{d} approaches L resulting in the terminal voltage dropping below the cut-off voltage.*

4.2.3 Optimal battery electrode thickness

Combining Eqs. (4.7) and (4.9) gives the position of the reaction front at the end of the discharge when the terminal voltage V_{cell} equals the cut-off voltage V_{d}

$$x_{\text{r}} = \kappa_{\text{d}} \frac{V_{\text{eq}} - V_{\text{d}} - \Delta V}{j} = L_{\text{opt}}. \tag{4.10}$$

Here $V_{\text{eq}} - V_{\text{d}}$ is the maximum allowable voltage drop of the battery over its discharge. Subtracting other losses ΔV, the numerator $V_{\text{eq}} - V_{\text{d}} - \Delta V$ gives the voltage that 'remains' for ohmic losses in the electrolyte of the porous electrode.

Ideally, the final state of charge is small, and the reaction zone has approximately reached the end of the battery electrode, so little unreacted electrode material remains. Therefore, Eq. (4.10) directly gives the optimal porous electrode thickness L_{opt} for this current density j. Similar to what we found in Eq. (3.68), higher current densities and lower conductivities dictate the use of thinner electrodes.

Often, we want to discharge a battery in a certain given time t_{d} rather than at a given current density. In this case using Eq. (4.5), $j = \frac{qL}{t_{\text{d}}}$, in Eq. (4.10) and neglecting the current density dependence of ΔV, gives a quadratic equation for L that is solved

by[6]

$$\boxed{L_{\text{opt}} = \sqrt{\kappa_{\text{d}} \frac{V_{\text{eq}} - V_{\text{d}} - \Delta V}{q} t_{\text{d}}}.} \tag{4.12}$$

For example, with $t_{\text{d}} = 10$ h, $\kappa_{\text{d}} = 1$ S/m, $V_{\text{eq}} - V_{\text{d}} = 0.1$ V, and $q_{\max} \approx 1$ kAh/l, we obtain $L \approx 1$ mm. The effective conductivity in batteries is usually relatively low compared to that in fuel cells, electrolysers, and flow batteries. Unlike in these other applications, the electrodes themselves are the reactants. Therefore, battery electrodes are relatively thick, which is necessary to achieve a high capacity. Through Eqs. (4.10) and (4.12), this implies that batteries have relatively low current densities or long discharge times.

4.3 Single particle models

4.3.1 Solid diffusion

The moving reaction zone model we just considered is expected to be a good approximation for high discharge rates when ohmic limitations in the electrolyte are limiting. However, the slow penetration of reactants and products inside solids is often the limiting process. The model we follow here is inspired by a common approach to battery modelling discussed in more detail in section 4.3.6. We assume that redox reactions take place at the battery particle surface after which the products diffuse towards the bulk of the particle. [7] The diffusion coefficient in gases and liquids are typically of the order of 10^{-5} and 10^{-9} m^2/s, respectively, whereas in solids it can be still many orders of magnitude lower than in liquids. See Tbl. 4.1 for typical diffusion coefficients in various Lithium compounds.

We will denote the radius of a spherical particle with R, trusting that it will not lead to confusion with the resistance for which we used the same symbol before. The

[6] Neglecting the current-density dependence of $\eta_{\text{a}0} - \eta_{\text{a}0}$ but including the final term ARj in Eq. (4.8) gives a quadratic equation for L that can be solved by

$$L = \frac{AR\kappa_{\text{d}}}{2}\left(\sqrt{1 + \frac{4}{AR\kappa_{\text{d}}}\frac{t_{\text{d}}}{q}\frac{V_{\text{eq}} - \eta - V_{\text{d}}}{AR}} - 1\right) \approx \begin{cases} \sqrt{\kappa_{\text{d}}\frac{V_{\text{eq}} - V_{\text{d}} - \Delta V}{q} t_{\text{d}}} & \text{if } AR \ll \frac{L}{\kappa_{\text{d}}} \\ \frac{t_{\text{d}}}{q}\frac{V_{\text{eq}} - \eta - V_{\text{d}}}{AR} & \text{if } AR \gg \frac{L}{\kappa_{\text{d}}}. \end{cases} \tag{4.11}$$

The bottom expression uses the expansion $\sqrt{1+x} \approx 1 + \frac{x}{2}$ for $x \ll 1$. Typically, the separator will be much thinner and less resistive than the electrode so that $L/\kappa_{\text{d}} \gg AR$ and the top expression, or Eq. (4.12), will be more relevant.

[7] It may be argued [6] that the intercalation of e.g. Lithium in the *intercalation host* graphene show in Fig. 4.2 is not a purely faradaic process. This is a process in which electrons are transferred, and redox reactions occur. When the charged lithium cations move between the carbon sheets, they attract electrons in the carbon phase, creating a capacitance. Even in the absence of reactions, such a process could store electrical energy. Both processes may also occur simultaneously.

Material	D [m^2/s]
$LiCoO_2$	$10^{-14} - 10^{-12}$
$LiMn_2O_4$	$10^{-15} - 10^{-13}$
$LiFePO_4$	$10^{-19} - 10^{-18}$

Table 4.1: *Diffusivities of lithium ions in different electrode materials used in Li-ion batteries.*

characteristic time-scale for diffusion over a distance R is[8]

$$t_D \equiv \frac{R^2}{D}. \tag{4.13}$$

Discharging a porous battery electrode consisting of particles with radius R over a discharge time t_d thus requires $R \lesssim \sqrt{Dt_\mathrm{d}}$. For a discharge time of $t_\mathrm{d} \sim 1$ hour, Table 4.1 gives a radius of a few micrometres for $LiCoO_2$ and only a few tens of nanometres for $LiFePO_2$. Therefore, solid diffusion requires battery electrodes to consist of very small particles or highly porous materials in which the electrolyte is never far away from the electrode-electrolyte interface.

4.3.2 The single particle model

Reactants and products of the redox reactions in the electrolyte are transported by diffusion and, in the case of ions, migration. At low to moderate discharge rates, gradients in the concentration and overpotential can usually be neglected. In Chapter 3, this was quantified using $j \ll J_D, J_\kappa$. Under these conditions, the concentrations and overpotential in the electrolyte can be taken to be approximately constant, as schematically illustrated in the below Figure 4.6. We will allow a significant drop in concentration and potential over the separator but do consider homogeneous conditions throughout the electrodes. This means that all active particles that comprise the porous electrode experience the same conditions, so we can describe their charging and discharge by considering a single representative particle.

The reactant or product ion flux $N_\perp$ at the surface of each particle will be the same throughout the porous electrode. The constant associated local surface current density $j_\perp$ adds up for all particles, using Eqs. (3.18) and (3.21), to give a total current density magnitude

$$j = aL|j_\perp|, = aLnF|N_\perp|. \tag{4.14}$$

Here, Eq. (3.4) gives the total volumetric surface area $a = (1-\epsilon)\, a_\mathrm{s}$ [m$_\mathrm{s}^2$/m^3] in terms of the volumetric surface area a_s of a single battery particle and the porosity ϵ. As

[8] Eq. (2.57), for example, gave for the one-dimensional diffusion boundary layer thickness in case of a constant flux $\delta \sim \sqrt{Dt}$.

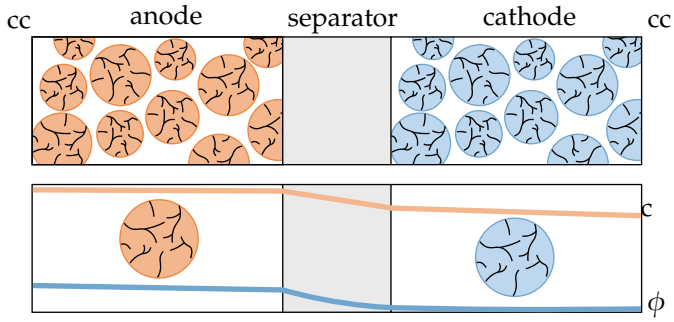

Figure 4.6: *A battery electrode consisting of many small particles in a 'single particle model' is represented by a single characteristic particle, assuming all particles in an electrode experience the same electrolyte potential ϕ and concentration.*

discussed in section 3.3.1, the multiplication factor aL is the conversion factor between the total internal and external electrode area.

4.3.3 Diffusion in a spherical particle

We will denote the concentration of solid reactant material, per total unit volume, with a capital C [mol/m^3], and reserve the lower case c for the concentration of a reactant in a fluid or the electrolyte concentration. As discussed above, we assume the redox reactions occur at the particle surface and assume that the transport of reactants from the interior of the battery material can be described by diffusion. We can thus describe the solid reactant concentration C by the general conservation equation, Eqs. (2.1) and (2.2) without flow and sources,

$$\frac{\partial C}{\partial t} = -\nabla \cdot \boldsymbol{N}, \text{where} \quad \boldsymbol{N} = -D\nabla C. \tag{4.15}$$

Consider the spherical particle shown in Figure 4.7. Its solid material with an initial concentration $C_{\max}$ reacts at the surface at a radial coordinate $r = R$, equal to the sphere radius R. The surface flux

$$N_\perp(t) = -D\frac{\partial C}{\partial r}\bigg|_R, \tag{4.16}$$

is positive for flux from the solid in the direction of the electrolyte, which is the case in Figure 4.7. The effective medium diffusivity D used here may differ from the material diffusivity in case the particle is porous. At the centre of the particle, by symmetry, there is zero flux, so $D\frac{\partial C}{\partial r}\big|_{r=0} = 0$. Using these boundary conditions while integrating Eq. (4.15) over the particle volume and dividing by the volume V_s gives, using the divergence theorem

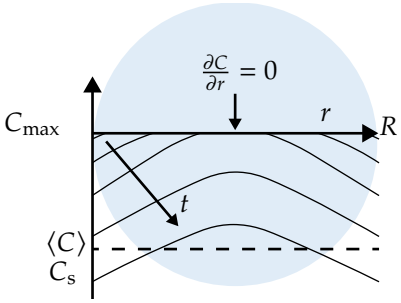

Figure 4.7: *The concentration profiles in a spherical particle at various times for a constant charge or discharge rate. Initially, the concentration profile forms a transient boundary layer near the surface, while all of the sphere's volume is affected for longer times.*

$$\frac{d\langle C \rangle}{dt} = -a_s N_\perp, \tag{4.17}$$

where $\langle C \rangle \equiv \frac{1}{\mathcal{V}_s} \int C d\mathcal{V}$ is the average concentration, and $a_s \equiv A_s/\mathcal{V}_s$ the particle volumetric surface area. Equation (4.17) holds for any particle shape, but for a sphere we have $a_s = \frac{4\pi R^2}{\frac{4}{3}\pi R^3} = \frac{3}{R}$.[9]

Equation (4.16) can be solved analytically, resulting in a somewhat complicated series solution for $C(r,t)$. Alternatively, in two limiting cases, we can solve Eq. (4.17) for the average concentration $\langle C \rangle$. We define the mass transfer coefficient by the ratio of the flux and the difference between the average and surface concentration:

$$k_m \equiv \frac{N_\perp}{\langle C \rangle - C_s}, \tag{4.18}$$

where $C_s \equiv C(r = R)$ is the surface concentration. Simple expressions for this mass transfer coefficient exist in two distinct regimes, shown in Figure 4.7:

1. *Developing* ($t \ll t_D$): the concentration boundary layer is much thinner than the particle radius.
2. *Developed* ($t \gg t_D$): the concentration profile changes throughout the entire particle.

For short times $t \ll t_D$, the concentration varies only in a thin layer near the particle surface, so the exact particle shape does not matter, and we can use the solution of the one-dimensional diffusion equation. With $N_\perp = D\frac{\langle C \rangle - C_s}{\delta}$ we see from Eq. (4.18) that

[9] In case of spherical symmetry, $\nabla^2 C = \frac{1}{r^2}\frac{\partial}{\partial r}\left(r^2 \frac{\partial C}{\partial r}\right)$. Multiplying Eq. (4.15) by $4\pi r^2$ and integrating from $r = 0$ to $r = R$ and dividing by the particle volume $V_s = 4\pi R^3/3$ gives with $\langle C \rangle = \frac{1}{V_s}\int_0^R C(r)\, 4\pi r^2 dr$, again, Eq. (4.17). However, using the divergence theorem is arguably easier and more general.

$k_m = D/\delta$. For a constant flux $N_\perp$, Sand's analysis gives a boundary layer thickness described by Eq. (2.57) so the mass transfer coefficient k_{m0} at time $t = 0$ is given by

$$k_{m0} = \sqrt{\frac{\pi D}{4t}}. \tag{4.19}$$

While initially it is very high, the mass transfer coefficient decreases as time progresses and the boundary layer thickness increases. As the boundary layer approaches the order of the particle size, Eq. (4.19) becomes invalid. In Appendix 4.A, we show for a spherical particle that δ can be approximately replaced by $R/5$ in this case, so the mass transfer coefficient for times $t \gg t_D$ reads

$$k_{m\infty} \approx \frac{5D}{R}. \tag{4.20}$$

The smaller the particle, the larger the mass transfer coefficient. This is expected because of the larger concentration gradients that are associated with smaller length scales.

4.3.4 State of charge

Assuming a first-order reaction takes place at the particle surface, we can write

$$N_\perp = kC_s, \tag{4.21}$$

where k is the reaction rate coefficient. In general, this will depend on the overpotential and the electrolyte concentration. In a single particle battery model, these are assumed constant throughout the electrode, so we can treat k as a constant here.

Combining Eqs. (4.21) and (4.18), we can solve for $C_s = \frac{k_m}{k+k_m}\langle C\rangle$ to give

$$N_\perp = k_{tot}\langle C\rangle, \text{where} \frac{1}{k_{tot}} = \frac{1}{k} + \frac{1}{k_m}. \tag{4.22}$$

The total transfer resistance $1/k_{tot}$ is obtained as a reaction resistance $1/k$ and a mass transfer resistance $1/k_m$, acting in series. With this, Eq. (4.17) can be written as

$$\boxed{\frac{d\langle C\rangle}{dt} = -a_s k_{tot}\langle C\rangle.} \tag{4.23}$$

The state of charge is given by the average reactant concentration divided by the maximum. Integrating Eq. (4.23), with the initial condition $\langle C\rangle(t=0) = C_{max}$, gives

$$S_{oC} = \frac{\langle C\rangle}{C_{max}} = e^{-\int \frac{dt}{\tau}}, \text{with } \tau = \frac{1}{a_s k_{tot}}. \tag{4.24}$$

For $t \ll t_D$, the boundary layer will be very thin, and the mass transfer resistance $1/k_m$ can be neglected. In case $k_{tot} \approx k$ is constant, the state of charge $S_{oC} = \frac{\langle C\rangle}{C_{max}} = e^{-ka_s t}$ decays exponentially with time.

For $t \gg t_D$, assuming $1/k_\mathrm{m} \gg 1/k$, for a spherical particle Eq. (4.20) can be used to give for the characteristic time-scale of Eq. (4.24)

$$\tau_\infty \equiv \frac{1}{k_{\mathrm{m}\infty} a_\mathrm{s}} = \frac{R^2}{15D}. \tag{4.25}$$

In this regime of mass transfer-limited discharging, Eq. (4.25) shows that smaller particles can be discharged faster. However, for very small particles, the reaction may become limiting. As an example, for a solid diffusivity $D = 10^{-13}$ m^2/s, to have $\tau_\infty \lesssim 1$ h requires a particle radius $R \lesssim 75$ μm.

In both of the above examples, the discharge rate decreases with time. However, often, batteries will be used with a more or less constant discharge rate. In this case, the state of charge will go down linearly as $\mathrm{S_{oC}} = 1 - \frac{t}{\tau_0}$. Inserting this into Eq. (4.24) gives

$$\frac{1}{\tau} = a_\mathrm{s} k_\mathrm{tot} = \frac{1}{\tau_0 - t}. \tag{4.26}$$

So, as time increases, the total transfer coefficient has to decrease to compensate for the reduced reactant concentration. For redox reactions, this can be realised by increasing the overpotential. As t approaches $\tau_0 = \frac{1}{a_\mathrm{s} k(t=0)}$, Eq. (4.26) shows that ever-larger overpotentials will be needed. This additional concentration overpotential will be quantified further in the next section.

4.3.5 Polarisation relation

Assuming first-order Tafel kinetics $j_\perp = j_* \frac{C_\mathrm{s}}{C_\mathrm{max}} \mathrm{e}^{\eta/b}$ so, using Eq. (4.14), the overpotential is given by

$$\boxed{\eta = b \ln\left(\frac{j C_\mathrm{max}/J_*}{\langle C \rangle \left(1 - \frac{j}{j_\mathrm{lim}}\right)} \right),} \tag{4.27}$$

where the numerator represents the surface concentration C_s, Eq. (3.43) gives $J_* \equiv aLj_*$, and we introduced

$$j_\mathrm{lim} = aLnFk_\mathrm{m}\langle C \rangle. \tag{4.28}$$

Using Eq. (4.24), Eq. (4.27) can be written as

$$\frac{\eta}{b} = \ln\left(\frac{j}{J_*}\right) + \int \frac{dt}{\tau} + \ln\left(\frac{1}{1 - \frac{j}{j_\mathrm{lim}}}\right). \tag{4.29}$$

where $j_\mathrm{lim} = aLnFk_\mathrm{m} C_\mathrm{max} \mathrm{e}^{-\int \frac{dt}{\tau}}$. Here, the first term represents the activation overpotential. The second term represents the concentration overpotential due to the decrease in the average concentration. The final term is the additional concentration

overpotential that arises because, as a result of internal mass transport limitations, the surface concentration C_s will always be below the average particle concentration. This term can diverge even for non-zero average concentration because the internal mass transfer coefficient is finite.

Unlike the other terms, the second term in Eq. (4.29) is not a logarithm. This is because the average concentration decreases exponentially, cancelling the logarithm. Because the solid concentration decreases exponentially, the overpotential increases linearly with time. It implies that for each decrease of the state of charge $S_{oC} = \langle C \rangle / C_{max}$ by a factor e, the overpotential η increases with a Tafel slope b. Or, every halving in the state of charge adds $b \ln 2 \approx 0.7b$ to η. As j approaches j_{lim}, the increase will increase dramatically. While the physics is quite different, we thus find a similar behaviour as with the moving reaction zone model, as shown in Fig. 4.5. Initially, cell potential decreases linearly, followed by a large drop due to activation overpotential associated with reactant depletion until the cut-off voltage is reached.

4.3.6 *Pseudo-2D Model **

Most battery models use some form of the *pseudo-two-dimensional* (or P2D) model developed by Doyle, Fuller, and Newman [10]. It effectively applies a single particle model to each point along a one-dimensional coordinate x through the battery electrode. Therefore, it allows for the inclusion of both the behaviour inside the battery particles and in the electrolyte. For the electrolyte, we may use the porous electrode binary electrolyte equations consisting of Eq. (3.15) and (3.18) combined with Eq. (2.41) without flow

$$\frac{\partial \epsilon c}{\partial t} - \nabla \cdot (D_a \nabla c) = a j_\perp, \tag{4.30}$$

where for the local current density the Butler-Volmer equation is used,

$$j_\perp = j_{*s} \left(e^{\alpha \frac{F\eta}{RT}} - e^{-(1-\alpha)\frac{F\eta}{RT}} \right). \tag{4.31}$$

Here j_{*s} may depend on the surface concentration of electrolyte c_s and solid reactant C_s, see Eq. (1.B.42). For a binary electrolyte with an anion with zero flux,[10] Eqs. (2.49) and (2.51) give for the flux

$$N(x = 0) = -\frac{D_a}{1 - t_+} \frac{dc}{dx}, \tag{4.32}$$

which forms the boundary condition to Eq. (4.30). This approach allows each particle to experience a different electrolyte concentration and overpotential and have a different time evolution. At each electrode position, we have a second coordinate r inside the particle. The solid concentration is obtained by solving Eq. (4.15) or, in radial coordinates,

[10] For example, in a Lithium-ion battery where lithium cations carry the charge. For a zero-flux cation, t_+ is replaced by t_- in Eq. (4.32).

$$\frac{\partial C}{\partial t} = \frac{D}{r^2}\frac{\partial}{\partial r}\left(r^2\frac{\partial C}{\partial r}\right). \tag{4.33}$$

Solving for the entire concentration profile as a function of r is not necessary since only its surface value $C_s = C(r = R)$ is needed. For example, solving Eqs. (4.23) and Eq. (4.20) can lead to a much faster one-dimensional model.

A concentrated-solution theory equation like $\boldsymbol{i} = -\kappa\nabla\phi - \kappa_d\nabla\ln c$ is typically used since the electrolyte concentration can be high. This closely resembles our dilute solution theory expression Eq. (2.46), with the difference that the conductivity κ and *diffusive conductivity* $\kappa_d = \chi\kappa$ will strongly depend on the local electrolyte concentration.

4.4 Binary electrolyte

In the moving reaction zone model of section 4.2 we assumed Ohm's law with a constant conductivity, which may be fine for e.g. solid-state batteries. However, battery electrolytes are often binary electrolytes, whose concentration can vary throughout the electrode. As in section 2.4, we consider the equations for a monovalent binary electrolyte with a reacting anion and a zero-flux cation.[11] Equation (2.49) gives the conductivity $\kappa = -i/\phi'$ as

$$\kappa = \kappa_0\bar{c}, \text{where } \kappa_0 = \frac{2D_-F^2c_0}{\mathcal{R}T}. \tag{4.34}$$

Here, the dimensionless concentration $\bar{c} = c/c_0$ is obtained by dividing by the electrolyte concentration $c_0 = c(x = 0)$ at the entrance of the porous electrode. As derived in section 2.4.3, the factor two originates from diffusion, which contributes to the current in equal proportion to migration. Since the conductivity now depends on concentration, we have to modify the porous electrode equations (3.44)-(3.46) slightly, to

$$\bar{c}' = i/2FD_-c_0, \tag{4.35}$$

$$\eta' = i/\kappa_0\bar{c}, \tag{4.36}$$

$$i' = aj_*\bar{c}^{\,r}e^{\eta/b}, \tag{4.37}$$

where we used Eq. (2.49) to modify Eq. (3.44). For generality, we consider a general reaction order r.

Dividing Eq. (4.35) by (4.36), we get

[11] This is relevant, for example, for an alkaline battery with a K^+OH^- electrolyte. Equations (4.3)-(4.4) show that OH^- is a reactant at the anode during discharging and at the cathode during charging. Non-monovalent electrolytes like $H_2{}^+SO_4{}^{2-}$ can be described using small modifications considered in Appendix 2.G. The case of a reacting cation, to describe a Li-ion battery electrolyte, for example, is obtained by changing all pluses into minuses and minuses into pluses below.

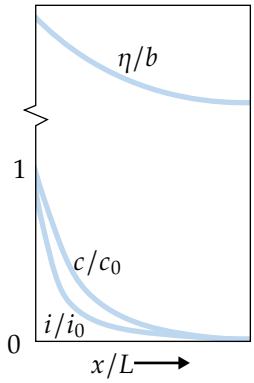

Figure 4.8: *A schematic illustration of the transport of ions of a binary electrolyte in a porous electrode where $x = 0$ represents the reaction front or the 'entrance' of the porous electrode at the start of a charge or discharge.*

$$\frac{d\bar{c}}{d\eta} = \frac{\bar{c}}{\mathcal{R}T/F} \rightarrow \bar{c} = \mathrm{e}^{F\frac{\eta-\eta_0}{\mathcal{R}T}}. \tag{4.38}$$

As expected for a (cat)ion in thermal equilibrium, the electrolyte concentration is described by a Boltzmann distribution. As the current penetrates into the porous electrode, the overpotential and the reactant concentration decrease due to resistance and diffusion, respectively. Figure 4.8 shows the expected solution schematically. Here, $x = 0$ represents the 'entrance' of the porous electrode when the battery is fully charged or discharged. Alternatively, it represents the location of a moving reaction zone front. In this case, all battery material has reacted for $x < 0$ while for $x > 0$ the battery electrode has not yet reacted, and L becomes the length of this unreacted area.

Differentiating Eq. (4.35) with respect to x, inserting Eqs. (4.37) and (4.38) and using $b = \mathcal{R}T/\alpha F$ gives

$$\bar{c}'' = \frac{2\mathrm{M}^2/L^2}{1+\gamma+\alpha}\bar{c}^{\gamma+\alpha}, \text{where } \mathrm{M}^2 \equiv L^2\frac{1+\gamma+\alpha}{2}\frac{aj_*\mathrm{e}^{\eta_0/b}}{2FD_-c_0}. \tag{4.39}$$

This is equal to a reaction-diffusion equation with a reaction order not equal to γ but $\gamma + \alpha$. This is because the reaction coefficient, through its proportionality to $\mathrm{e}^{\eta/b} = \mathrm{e}^{\eta_0/b}\bar{c}^{\alpha}$, depends itself on concentration.

Eq. (4.39) can be solved analytically only for particular values of $\gamma + \alpha$. However, for $\mathrm{M} \gg 1$ we can deploy a similar approach as that followed in section 3.4.3. Similar to Eq. (3.63), we can write $\bar{c}'' = \frac{1}{2}\frac{d\bar{c}'^2}{d\bar{c}}$. Integrating Eq. (4.39) from $x = 0$ to the electrode end at $x = L$ gives

$$\frac{\bar{c}_L'^2 - \bar{c}_0'^2}{2} = \frac{2\mathrm{M}^2/L^2}{(1+r+\alpha)^2}\left(\bar{c}_L^{1+r+\alpha} - \bar{c}_0^{1+r+\alpha}\right) \xrightarrow{\bar{c}_L' \ll 1} |\bar{c}_0'| = \frac{2\mathrm{M}/L}{1+r+\alpha}. \tag{4.40}$$

The final expression holds in case of sufficiently large current densities, giving strong diffusion limitations. As illustrated in Fig. 4.8, the reactant concentration will then approximately vanish at the end of the electrode. Comparing this expression with Eq. (4.35), evaluated at $x = 0$, gives

$$\mathrm{M} = \frac{1+r+\alpha}{2}\frac{jL}{2FD_- c_0}. \tag{4.41}$$

Comparing this expression with that of Eq. (4.39) gives, after some algebra

$$\boxed{\eta_0 \approx 2b\ln\left(\frac{j}{\sqrt{\frac{4FD_- c_0}{1+r+\alpha}aj_*}}\right),} \tag{4.42}$$

where we again find a doubled Tafel slope $2b$. Equation 4.42 may equally be written in the general form $\eta_0 = b\ln\left(\frac{j}{j_*\mathcal{E}}\right)$ of Eq. (3.42) with $J_* = aLj_*$ and an effectiveness factor $\mathcal{E} = 1/\mathrm{M}$.[12] This explicit polarisation relationship is equal to Eq. (3.60), obtained in the case of only diffusion limitations, upon replacing $D \to \frac{2D_-}{(1+r+\alpha)/2}$. The only differences are the doubled diffusivity $D = 2D_-$ and the division by $(1+r+\alpha)/2$. For a reaction order $r = 1$ and $\alpha = 1/2$ this becomes $1.6D_-$. This result is also equal to Eq. (3.65), obtained for a constant conductivity, upon replacing $b \to \frac{\mathcal{R}T/F}{1+r+\alpha}$.

4.5 Summary

- When $j \gg J_\kappa$, the moving reaction zone model gives voltage losses in a battery electrode as $\eta + jx_\mathrm{d}/\kappa_\mathrm{d}$ where $x_\mathrm{d} = \mathrm{S_{oC}}L$ is the position of the reaction zone.
- When $j \ll J_\kappa$, the single-particle model describes the state of charge $\mathrm{S_{oC}} = \frac{\langle C\rangle}{C_\mathrm{max}} = \mathrm{e}^{-\int \frac{a_\mathrm{s}}{1/k+1/k_\mathrm{m}}dt}$ (4.24) using a series resistance of the inverse of a reaction-rate coefficient $k = \frac{j_*}{nFC_\mathrm{max}}\mathrm{e}^{\eta/b}$ and the inverse of a mass-transfer coefficient k_m, the latter tending to $5D/R$ for long times.
- For a binary electrolyte, the diffusion and migration flux are equal, and we obtain for an r-th order reaction in case of strong transport limitations an effectiveness factor $\mathcal{E} \approx 1/\mathrm{M} \ll$ with $\mathrm{M} \approx \frac{1+r+\alpha}{2}\frac{j}{2FD_- c_0} \gg 1$.

[12] Therefore, we anticipate that, as discussed in section 3.4.4, using $\mathcal{E} \approx \frac{1}{1+\mathrm{M}}$ will give a reasonable approximation for all current densities.

4.6 Exercises

Exercise 4.1

A present disadvantage of electric vehicles would disappear if their charging time could be reduced to a time not much longer than is required for refuelling a petrol car.

a. If we want to charge an electric vehicle in 5 minutes, for what E-rate should its battery be designed?
b. For a 50 kWh battery, to what power does this rate correspond?

Exercise 4.2

Consider a battery electrode operated at high current density ($j \gg J_\kappa$), so the moving reaction zone model can be used. The battery has a separator of thickness L_s and conductivity κ_s. You may neglect the activation overpotential.

a. Write an expression for the potential difference $\Delta\phi_s$ across the separator at a current density j.
b. Now, consider a single porous electrode with a volumetric capacity q. We switch on the current when the electrode is fully charged. Write an expression for the position x_d of the reaction zone at a certain time, t.
c. Assuming that the conductivity of the reacted electrode is κ_d, write an expression for the potential drop over the distance x_d of reacted electrode.
d. Assuming no appreciable voltage losses arise at the other electrode of the battery, and with an equilibrium voltage V_{eq}, write an expression for the voltage V_{cell} that can be drawn from the battery at time t.
e. The amount of useful energy or work $\mathcal{U}$ that can be obtained from the battery is given by the integral of terminal voltage over the charge transferred. Using the above formulation for the battery terminal voltage, write an expression for this total energy, per unit membrane area, obtained over a discharge time t.
f. Using the above formulation, write an expression for the optimal thickness L_{opt} of the electrode for maximal capacity. (Hint: this implies the whole electrode is utilised when the maximal capacity is used)

Exercise 4.3

Consider a laptop Li-ion battery consisting of many cells in parallel. Each cell has a cross-sectional area of $A = 5$ cm^2, and consists of an anode and a cathode of $L = 0.1$ mm thick and a volumetric capacity of $q = 10^6$ Ah/m^3 each.

a. When discharging at C/5, what current is drawn per cell?

b. Consider a discharge of this battery using a moving reaction zone model, assuming equal ohmic losses in the anode and cathode. The ohmic drop over one fully discharged electrode is ten times that over the separator, which is 0.1 V at the considered current density. If the equilibrium voltage is $V_{eq} = 3.6$ V, at what state of charge is the cut-off voltage $V_d = 3$ V reached?

Exercises 4.4-4.21

Fill in the missing steps in the main text, indicated by the symbol .

*Appendices **

4.A *Parabolic polynomial approximation*

We postulate that the concentration profile can be written as

$$C(r,t) = \langle C \rangle(t) + \frac{N_\perp(t)R}{D} f(r). \tag{4.A.43}$$

To satisfy Eq. (4.16), we require $f(R) = -1/R$ and $\langle f \rangle = 0$ to ensure that $\langle C \rangle$ represents the average of C. In case of spherical symmetry $\nabla^2 C = \frac{1}{r^2}\frac{\mathrm{d}}{\mathrm{d}r}\left(r^2 \frac{\mathrm{d}C}{\mathrm{d}r}\right)$ and Eq. (4.15) becomes

$$\frac{\partial C}{\partial t} = \frac{D}{r^2}\frac{\mathrm{d}}{\mathrm{d}r}\left(r^2 \frac{\mathrm{d}C}{\mathrm{d}r}\right). \tag{4.A.44}$$

Inserting Eq. (4.A.43) gives $\frac{-3}{R^2} = \frac{1}{r^2}\frac{\mathrm{d}}{\mathrm{d}r}\left(r^2 \frac{\mathrm{d}f}{\mathrm{d}r}\right)$. This is solved by $f(r) = \frac{3}{10} - \frac{r^2}{2R^2}$, which satisfies $\frac{\mathrm{d}f}{\mathrm{d}r}(r=R) = -1/R$ and $\langle f \rangle = \frac{1}{4\pi R^2}\int_0^R 4\pi r^2 f(r)\mathrm{d}r = 0$. This parabolic solution gives the name to this approximation method, which is popular in battery modelling. Inserting Eq. (4.A.43) in Eq. (4.18) gives

$$k_{\mathrm{m}\infty} = -\frac{D}{Rf(R)} = \frac{5D}{R}. \tag{4.A.45}$$

4.B *Dimensionless binary electrolyte porous electrode model*

For a binary electrolyte with varying conductivity, given by Eq. (4.34), the porous electrode equations (4.35)-(4.37) become in the dimensionless notation of section 3.B (and for a general reaction order r):

$$\bar{c}' = -\bar{j}_D \bar{\imath}, \quad \bar{\eta}' = -\bar{j}_\kappa / \bar{c}\bar{\imath}, \quad \bar{j}_* \bar{\imath}' = -\bar{c}^r \mathrm{e}^{\bar{\eta}}. \tag{4.B.46}$$

Here $\bar{j}_\kappa = j/J_\kappa$ and $\bar{j}_D = j/j_D$, with J_κ and J_D given by

$$J_\kappa = \frac{\kappa_0 b}{L}, \quad J_D = \frac{2FD_- c_0}{L}. \tag{4.B.47}$$

A factor two multiplies the anion diffusivity in J_D in accordance with Eq. (2.49). With these definitions and $b = \mathcal{R}T/\alpha F$ we have

$$\frac{J_D}{J_\kappa} = \alpha. \tag{4.B.48}$$

Therefore, for a binary electrolyte, there is no need for a separate J_κ and J_D since migration and diffusion are coupled.

By differentiating the first of Eqs. (4.B.46) and inserting the last we obtain, with $\bar{c} = \mathrm{e}^{\frac{\bar{\eta}-\bar{\eta}_0}{\alpha}}$ from Eq. (4.38),

$$\bar{c}'' = \frac{\bar{j}_D \bar{c}^r}{\bar{j}_*} \mathrm{e}^{\bar{\eta}} = \frac{2\mathrm{M}^2}{1+r+\alpha} \bar{c}^{r+\alpha}, \tag{4.B.49}$$

where

$$\mathrm{M}^2 \equiv \frac{1+r+\alpha}{2} \frac{\bar{j}_D \mathrm{e}^{\bar{\eta}_0}}{\bar{j}_*} = \frac{1+r+\alpha}{2} \bar{j}_D. \tag{4.B.50}$$

The final expression in Eq. (4.B.50) is the dimensionless form of Eq. (4.41). The dimensionless overpotential $\bar{\eta}_0 = \ln\left(\frac{\bar{j}_*}{\bar{\varepsilon}}\right)$ with $\mathcal{E} \approx 1/\mathrm{M} \ll 1$ becomes $\bar{\eta}_0 = \ln\left(\frac{1+r+\alpha}{2} \bar{j}_D \bar{j}_*\right)$.

Chapter 5

Fuel cells

This chapter concerns the modelling of fuel cells, with a particular focus on the effects of produced water in hydrogen fuel cells. First, the transport of water in the membrane and flow channels is briefly described, primarily empirically. A multiphase Darcy flow model is derived for water transport in the diffusion layer. Finally, a flooded agglomerate model *of the catalyst layer is presented that takes into account diffusion inside the water-filled catalyst particles.*

Fuel cells are galvanic cells that generate electricity, as illustrated in Figure 5.1. Where batteries have solid reactants, fuel cells have gaseous or sometimes liquid reactants. Similar to rechargeable batteries, the reaction in fuel cells can sometimes be reversed, allowing the gases or liquids to store energy. If these galvanic and electrolytic reactions occur within the same cell, the resulting system is called a flow battery. Therefore, many aspects of fuel cell modelling also apply to flow batteries. Conversely, most aspects treated in chapter 7 on redox flow batteries will also be relevant for fuel cells. While chapter 7 will focus on two-dimensional single-phase transport, we will consider aspects related to multiphase flow. In particular, we will focus on the case in which gaseous reactants produce liquid products. This occurs, for example, in a PEM[1] fuel cell. Hydrogen and oxygen are converted to water according to the following redox reactions

$$2H_2 \rightarrow 4H^+ + 4e^- \qquad \text{(anode)}, \tag{5.1}$$

$$O_2 + 4H^+ + 4e^- \rightarrow 2H_2O. \qquad \text{(cathode)} \tag{5.2}$$

5.1 *Types of fuel cells* *

A concise overview of the most important types of fuel cells is given in Table 5.1. The redox reactions given by Eqs. (5.1) and (5.2) assume acidic conditions, as occur in

[1]PEM can stand for either Polymer Electrolyte Membrane or Proton Exchange Membrane.

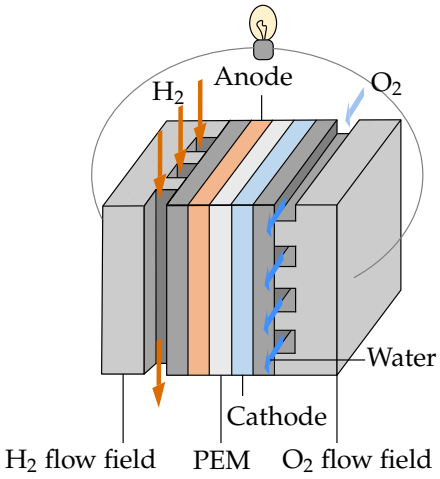

Figure 5.1: *The different types of fuel cells are usually named after their electrolyte and typically operate on hydrogen, oxygen, or air.*

e.g. polymer electrolyte fuel cells (PEMFCs) and phosphoric acid fuel cells (PAFCs).[2] An exception is the direct-methanol fuel cell (DMFC), which, as its name suggests, converts methanol instead of hydrogen. Unlike the other fuel cells, it is named after its reactant and not after its electrolyte or membrane.

Solid oxide fuel cells (SOFC) and molten carbonate fuel cells (MCFC) offer greater fuel versatility than traditional fuel cells, which are limited to only hydrogen. These types of fuel cells also allow various other input gasses, such as methane. Due to their high operating temperature, they can internally catalytically reform these gases into hydrogen. Their high temperature allows for cheaper catalysts but leads to a more complex design and higher material requirements.

Alkaline fuel cells were the first fuel cells commercially available, following their introduction during the 1960 Apollo space missions. However, catalyst poisoning due to CO and CO_2 from the atmosphere somewhat limited their success on Earth. Phosphoric acid fuel cells (PAFC) do not operate at the same high temperatures as SOFCs and MCFCs but still benefit from higher temperatures, which allow them to increase their electrolyte conductivity. However, these fuel cells are currently losing ground to polymer electrolyte fuel cells (PEMFC), which will be the primary focus of this chapter.

[2] In alkaline fuel cells, hydroxide ions (OH^-) are the charge carrier and $4OH^-$ should be added on both sides of both reactions. Subsequently $4OH^- + 4H^+$ may be replaced by $4H_2O$. In SOFCs, the oxygen ion (O^{2-}) is the charge carrier and $2O^{2-}$ should be added on both sides of both reactions. Subsequently $2O^{2-} + 4H^+$ may be replaced by $2H_2O$. Finally, MCFCs have CO_3^{2-} as the charge carrier and $2CO_3^{2-}$ should be added along with using $2CO_3^{2-} + 4H^+ \rightarrow 2H_2O + 2CO_2$.

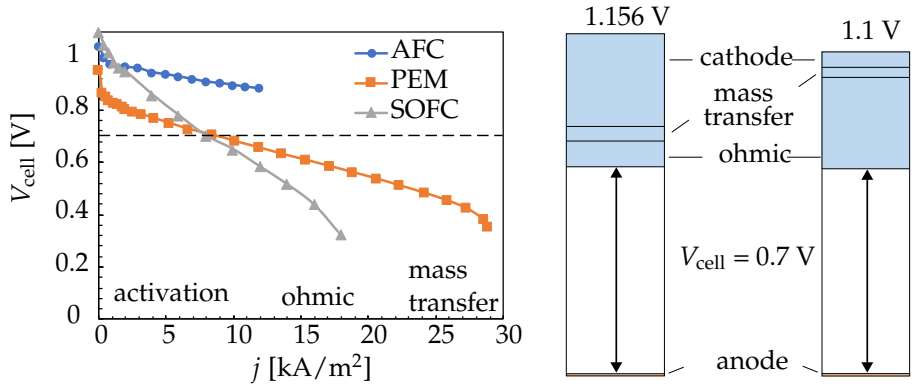

Figure 5.2: *A graph showing typical polarisation curves of an Alkaline Fuel Cell (AFC), Polymer Electrolyte Membrane (PEM), and Solid Oxide Fuel Cell (SOFC). The bar charts on the right show the approximate contributions of activation, mass transfer and ohmic losses to the overall cell voltage of the PEMFC and SOFC, operating at 0.7 V. It is evident, from the strong linear decrease, that the SOFC in this figure experiences substantial ohmic losses. However, the activation losses are considerably smaller, allowing it to outperform the PEMFC at low current densities. With kind permission from Thomas F. Fuller and John Harb for allowing re-use of their data [12]..*

	PEMFC	**AFC**	**PAFC**	**MCFC**	**SOFC**	**DMFC**
Electrolyte	Polymer	KOH	H_3PO_4	K_2CO_3	Ceramics	Polymer
Catalyst (a/c)	Pt/Ni	Fe,Ni/Ag	Pt	Ni	Cermet	Pt,Ru
Temp. (°C)	40-80	65-220	205	650	600-1000	25-90
Charge carrier	H^+	OH^-	H^+	CO_3^{--}	O^{--}	H^+

Table 5.1: *A short overview of the most important fuel cells: the polymer electrolyte/proton exchange membrane (PEMFC), alkaline (AFC), phosphoric acid (PAFC), solid oxide (SOFC), and direct methanol (DMFC) fuel cell. Only the most commonly used materials and operating temperatures are indicated. A cermet is a ceramics-metal mixture, typically Nickel with Yttria-Stabilised Zirconium (YSZ).*

Figure 5.2 shows typical polarisation curves of three different types of fuel cells, the AFC, PEM, and SOFC.

The splitting of hydrogen at the anode (Eq. (5.1)) is a simple reaction. In an acidic medium, platinum is an almost ideal catalyst, so the activation losses involved are often negligible. This is clear from the bottom part of Fig. 5.2, where the losses of a PEMFC and SOFC are split into their different components at a current density for which their voltage is similar. The anode polarisation, shown at the bottom, is very small. Clearly, the ohmic resistance of the reported SOFC is much higher than that of the shown PEMFC. This means that the latter clearly outperforms the former at high

current densities. However, at low current densities, the cell voltage of the SOFC is substantially higher than that of the PEMFC because of the higher equilibrium voltage associated with its higher temperature.

5.2 Water management

5.2.1 Catalyst layer

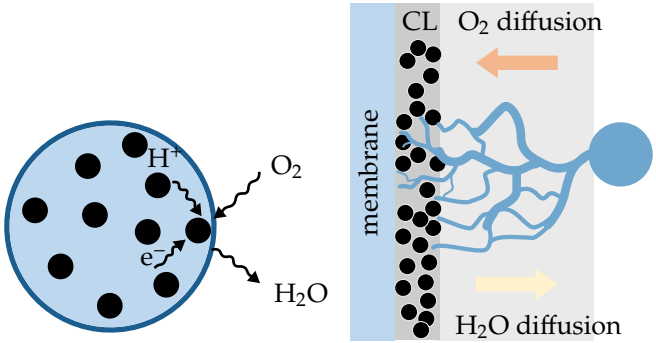

Figure 5.3: *Left: a schematic illustration of PEM fuel cell carbon-supported catalyst particle showing the black catalyst particles surrounded by a carbon/ionomer/binder mixture. Right: water that is produced at the cathode catalyst layer (CL) of a PEM fuel cell permeates as a liquid by capillary action or diffuses out as water vapour. The gas flow of oxygen or air can transport away droplets that form in the flow channel. [10]*

At the cathode of a PEMFC, oxygen reacts with electrons, and the protons are transported from the membrane to form water according to Eq. (5.2). The cathode catalyst layer, therefore, plays an important and intricate role, as it needs to facilitate the conduction of protons and electrons while also allowing gases to enter and liquid water to exit. These different demands are achieved by porous particles whose pores are wetted by the generated water. Oxygen can dissolve in this water and reach the active catalytic sites dispersed throughout the particles. These catalyst nanoparticles should be in good contact with the electrolyte, which is a solid polymer in a PEM fuel cell, and the electrode material, typically carbon. These two phases are mixed and held together by a binder material. See, for example, Figure 5.13. Additionally, the right-hand side of Fig. 5.3 provides a schematic representation of the path followed by liquid water and water vapour.

A gas diffusion layer (GDL) exists between the gas channel, which provides the reactant gases, and the thin catalyst layer, where the reactions take place. Because the catalyst layer is integrated into this layer, the combination is also sometimes called a gas-diffusion electrode (GDE). Section 5.3 will be fully dedicated to the mathematical description of this layer.

5.2.2 Flow channel

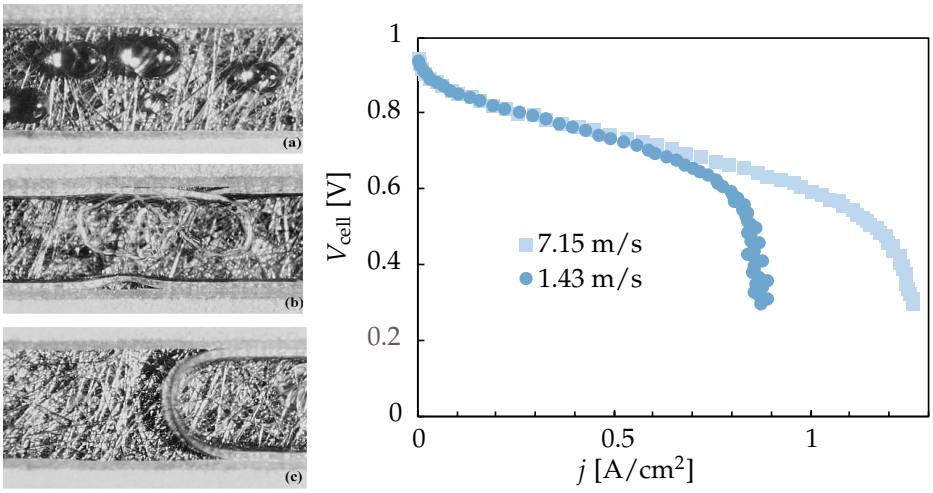

Figure 5.4: *Left: different flow regimes in a PEM fuel cell flow channel bordering a carbon paper GDL [31] with (a) droplets, (b) annular film (c) slug flow. Right: Cell voltage measurements at 80 °C show a strong dependence on average airflow velocity. [31] The transition from the droplet flow regime to the occurrence of films and slugs below roughly 4 m/s was assumed to be at least partly responsible. [31]*

Water making its way through the diffusion layer at the cathode side has to be transported out of the cell through the flow channel. The left-hand side of Fig. 5.4 shows different possible flow regimes. The droplet or spray regime may be the most favourable, as gas is in the continuous phase. In the film and slug flow regimes, the continuous liquid phase impedes the efficient transport of oxygen.
Through the resulting concentration overpotential, the flow channel can affect the cell performance. The right-hand side picture in Figure 5.4 shows the influence of the gas flow velocity on the cell voltage. The occurrence of liquid films and slugs in the flow channel was assumed to be at least partially responsible for the decrease in cell voltage at relatively low velocities and high current densities. [31]

5.2.3 Membrane

The presence of water is necessary for the polymer membrane to function well. The most commonly used polymer electrolyte membrane is Nafion.[3] The conductivity of this polymeric membrane material is crucially dependent on the water content, typically expressed in terms of a parameter λ_{H_2O} indicating the number of water

[3]This is a sulfonated tetrafluoroethylene. Ethylene (C_2H_4) in which the hydrogen atoms are replaced by fluorine and which is polymerised into chains that are terminated by a sulfonic acid (SO_3H) group.

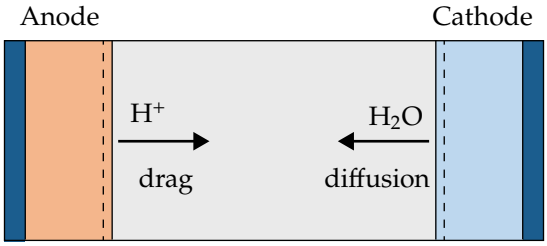

Figure 5.5: *A schematic of a PEM fuel cell, focused on the membrane in grey. Protons moving from anode to cathode bring along the water with them through electro-osmotic drag. On the other hand, water will also want to diffuse in the opposite direction, from cathode to anode.*

molecules per sulfonic acid group. The PEM membrane conductivity $\kappa \approx \kappa_0 + \lambda_{H_2O}\kappa'$ roughly increases linearly with the water content.

Protons can hop along the polymeric structures, but while doing so, they typically drag along several water molecules. This phenomenon is referred to as electro-osmotic drag. The electro-osmotic drag coefficient, ξ, denotes the average number of water molecules carried per proton. Consequently, an electro-osmotic molar flux $\xi \boldsymbol{j}/F$ of water will follow the proton current from the anode to the cathode.

Because water is generated at the cathode, see Eq. (5.2), it tends to diffuse through the membrane to the anode. An accurate quantitative picture requires concentrated solution theory. However, as a rough approximation, we may write

$$\boldsymbol{N}_{H_2O} \approx \frac{\xi \boldsymbol{j}}{F} - D\nabla c_{H_2O}. \tag{5.3}$$

Note that in a membrane, water can be a minority species and can build up gradients. Fick's law of diffusion has been found to hold reasonably well for many polymer membranes. The balance between these opposing fluxes determines how well the membrane is hydrated and, therefore, its conductivity. In this way, water transport significantly impacts the overall cell resistance. Adding to this possible flooding of the catalyst layer, discussed in the next section, water management emerges as a complex but important aspect of obtaining good fuel cell performance.

5.3 Multiphase gas diffusion layer model

The gas diffusion layer typically consists of carbon microfibres made into felts, cloths, or papers. Coatings of PTFE (Teflon) or similar materials are used to make the fibres hydrophobic. This porous layer is placed in between the catalyst layer and the flow channel. It serves several purposes:

1. Providing mechanical strength and shielding the precious and fragile catalyst layer from the channel flow, reducing erosion and degradation.

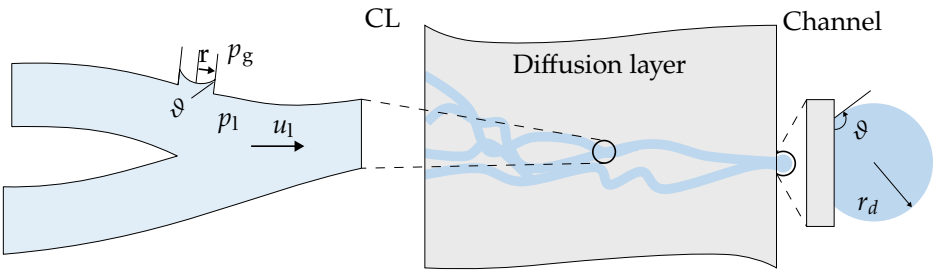

Figure 5.6: *This idealised schematic of a hydrophobic (contact angle $\vartheta > 90°$) cathode diffusion layer illustrates how liquid water, produced at the catalyst layer (CL) on the left, is transported towards the flow channel on the right, through 'channels' formed by the largest pores.*

2. Providing an electronic connection between the catalyst particles and the bipolar plate.

3. Removing water due to its hydrophobic nature, while allowing oxygen to enter.

This section will primarily focus on this last functionality. The gas phase will contain significant amounts of water vapour at temperatures approaching the boiling point. We will consider relatively low temperatures, so we may neglect water vapour transport. We will also neglect the frictional pressure drop due to gas flow, which will be a reasonable approximation at liquid fractions that are not too high. Therefore, the following model is not a substitute for more rigorous models but serves primarily to illustrate the important mechanism of capillary transport.

Figure 5.6 shows the cathode diffusion layer, where liquid water is generated at the catalyst layer (CL) on the left and transported by capillary action out to the right. The capillary force, or surface tension force, keeps the liquid together. It allows the formation of droplets on the surface of the diffusion layer, as shown on the left Fig. 5.4. Next, the gas flow shears and takes away these droplets.

The cathodic gas diffusion layer is porous and resembles paper or a sponge. But because it is made hydrophobic, it will soak up gas instead of water. A water droplet on the surface of a hydrophobic material will approximately have the shape of a capped sphere. As illustrated in Fig. 5.6, the contact angle ϑ is defined as the angle between the surface of the material and the surface of the droplet, *through the liquid phase*.[4] This angle will be larger than ninety degrees for a hydrophobic surface, creating droplets larger than hemispheres.

The approximately spherical shape of droplets arises because the attractive forces between water molecules are much larger than between gas molecules. This results in a minimisation of the droplet surface area. Although attractive forces exist between

[4]On a surface that is not flat but rough or irregular over the scale of the wetted area, like the porous materials we consider here, droplets will show an *apparent contact angle* that may differ from the contact angle on a flat surface of the same material, which can be described by the Cassie-Baxter equation.

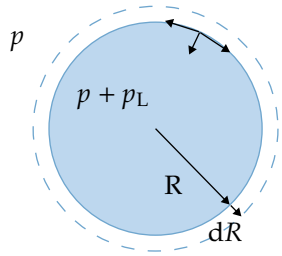

Figure 5.7: *The pressure inside a droplet or bubble is elevated compared to its surroundings by the Laplace pressure p_L. It is caused by the attractive forces in the liquid. Their tangentially oriented force at the gas-liquid surface results in a net inwards surface tension force, somewhat similar to the force exerted by the rubber surface of a balloon. Therefore, increasing the radius by an infinitesimal amount from R to $R+\mathrm{d}R$ results in work $\mathrm{d}W$ done by the Laplace pressure.*

the water and the solid surface, for a hydrophobic surface, these are weaker than those between water molecules, resulting in a limited *wetted area*.

The liquid is pushed away from where it is produced near the catalyst layer by pressure forces. The left part of Fig. 5.6 shows a magnification of a pore splitting into three smaller pores. Due to the hydrophobic nature of the pores, the liquid chooses to flow through the largest pores. Despite a positive pressure difference $p_l > p_g$ between the liquid and the gas, the liquid does not enter the small capillary. The liquid follows irregular paths through preferentially larger pores. The reason can be understood using the concept of capillary pressure.

5.3.1 Capillary pressure

Surface tension results from the attractive forces between molecules making up a liquid. In the bulk, these forces are in all directions, resulting in a net zero force. However, they do not exactly cancel each other out on a curved gas-liquid interface. As illustrated in Fig. 5.7, the direction of their net pulling force is tangential to the surface. Due to the curvature, this results in a net inward force. This restoring force is trying to make the surface as flat as possible. This can be described by the minimisation of a *surface energy* $\mathcal{U} = \gamma A$ proportional to the surface area A times the surface tension γ [J/m^2]. Surface tension hardly depends on the type of gas and is a property primarily of liquids.[5]

For the spherical gas-liquid surface of Fig. 5.7, this additional inwards force results in a higher pressure inside the closed surface compared to its outside. This additional pressure is called the *Laplace pressure* and exists for both droplets and bubbles. We can derive its magnitude from an energy balance using the following reasoning.

[5]The more general term *interfacial tension* describes the energy of interfaces that can also be between two liquids, a liquid and a solid, or between a gas and a solid.

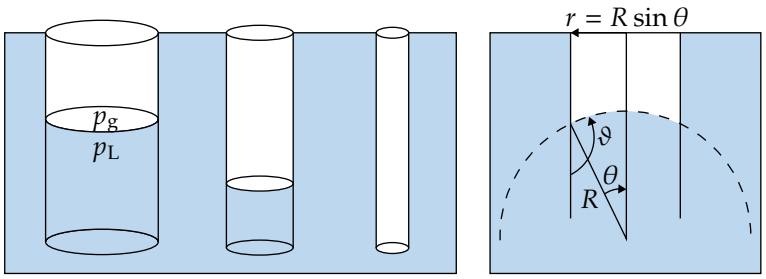

Figure 5.8: *Three hydrophobic capillaries or 'straws' with different radii are immersed in water, illustrating how the height of the water column pushed down will be larger for thinner capillaries (left). The liquid surface will be approximately spherical with radius* $R = r/\sin\theta = -r/\cos\vartheta$.

Because the pressure inside is higher than outside, the Laplace pressure p_L can be used to do work. An increase of the sphere radius R by an infinitesimal amount dR to $R + dR$ increases its volume $\mathcal{V} = \frac{4}{3}\pi R^3$ by $d\mathcal{V} = 4\pi R^2 dR$ and its surface area $A = 4\pi R^2$ by $dA = 8\pi R$. This exerts a work $dW = p_L d\mathcal{V}$ on the sphere's surroundings while changing its surface energy by $d\mathcal{U} = -\gamma dA$. Conservation of energy $pV + \mathcal{U}$ gives $dW = -\mathcal{U}$, so we find

$$p_L = \frac{2\gamma}{R}. \tag{5.4}$$

Because the Laplace pressure can become very high for small radii R, creating very small droplets or bubbles is exceedingly difficult.

Now consider Fig. 5.8, showing three hydrophobic straws or *capillaries* immersed in water. The straw area does not like to be wet, and the larger capillaries have a larger surface area, so why will the liquid level be lower in the thinner tubes? This is because of the smaller 'radius of curvature' that the liquid surface will have inside the capillaries.[6] The right-hand side of Fig. 5.8 shows a zoom of the convex surface associated with a hydrophobic contact angle $\vartheta \geq \pi/2$. The *radius of curvature* R is the radius of the approximately spherical surface. Using geometry and Eq. (5.4), the Laplace pressure is equal to[7]

$$\boxed{p_{cap} \equiv p_l - p_g = \frac{2\gamma|\cos\vartheta|}{r}.} \tag{5.5}$$

This pressure is usually referred to as the *capillary pressure* and Eq. (5.5) as the Young-Laplace equation. It shows that the smaller the radius r of the capillary, the higher

[6]The opposite happens in hydrophilic materials, where the water level creeps up more in smaller capillaries.

[7]An absolute value is taken as we defined the contact angle ϑ through the liquid phase so that hydrophobic materials have $\theta > \pi/2$ and $\cos\vartheta < 0$. However, the capillary pressure is defined by Eq. (5.5) as the pressure difference between the non-wetting phase and the wetting phase and is positive.

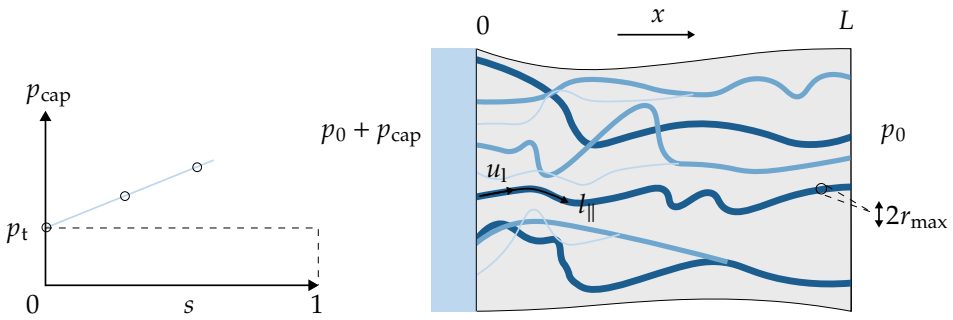

Figure 5.9: *By increasing the differential pressure p_{cap} between a water reservoir on the left of a gas-filled diffusion layer and recording the water saturation s, a capillary pressure-saturation curve can be generated. The largest pore (dark blue) with radius r_{max} forms a water channel first at the threshold p_t. At higher pressures p_{cap} the lighter-coloured pores follow, increasing s.*

the pressure difference between the liquid and the gas that can be sustained. In Fig. 5.8 this is hydrostatic pressure, while in Fig. 5.6 it is the frictional pressure drop required to push the water out. The capillary pressure thus explains why the fluid preferentially takes the path traced by the largest pores and does not enter the smaller pores. In the next section, we will consider how to quantify this behaviour.

5.3.2 Capillary pressure-saturation curve

Instead of the well-defined cylindrical capillaries used in the experiment of Fig. 5.8, diffusion layers typically do not consist of regular-sized capillaries, although making such structured diffusion media is an active research area. The carbon paper that is typically used consists of a random arrangement of approximately cylindrical fibres, with the space in between forming a wide pore-size distribution. This distribution can quantified using the procedure[8] illustrated in Fig. 5.9.

A gas-filled diffusion layer is bordered on one side by water, which is gradually increased in pressure. At the *threshold pressure*, or *breakthrough pressure*, p_t, the first liquid permeates through.[9] By Eq. (5.5) this pressure can be related to the *maximum pore radius* r_{max} as

$$p_t = \frac{2\gamma|\cos\vartheta|}{r_{max}}. \tag{5.6}$$

The *water saturation* s is defined as the volume fraction of the local pore volume that is occupied by water. Before the breakthrough pressure is reached, the saturation $s = 0$. With increasing liquid pressure, first, the largest pores and, eventually, the

[8]This is called the *porous diaphragm method*, or *restored capillary pressure method*. It is not often used because of its rather slow nature.

[9]For a hydrophilic material, the pressure at which gas first penetrates a water-filled porous medium is observable by the first bubble appearing on the liquid side and is therefore referred to as the bubble point.

smaller capillaries fill with liquid. With increasing liquid pressure, the liquid flow rate increases, and the saturation increases. The resulting curve that can be obtained between applied capillary pressure p_{cap} and water saturation s is shown on the left-hand side of Fig. 5.9. The slope $\partial p_{\text{cap}}/\partial s = p_{\text{t}}/\lambda$ can be characterised in terms of the *pore-size distribution index* λ, so[10]

$$p_{\text{cap}}(s) = p_{\text{t}}\left(1 + \frac{s}{\lambda}\right) \quad \text{for } s \approx 0. \tag{5.7}$$

Comparing with Eq. (5.5) we see that $\frac{r(s)}{r_{\text{max}}} = \frac{p_{\text{t}}}{p_{\text{cap}}} = \frac{1}{1+\frac{s}{\lambda}}$. This gives the smallest pore size r filled with liquid at a liquid saturation s. The average squared pore radius filled with water is given by

$$\left\langle \frac{r^2(s)}{r_{\text{max}}^2} \right\rangle = \frac{1}{s}\int_0^s \frac{p_{\text{t}}^2}{p_{\text{cap}}^2} ds = \int_0^s \frac{\mathrm{d}s}{\left(1+\frac{s}{\lambda}\right)^2} = \frac{\lambda}{s+\lambda}. \tag{5.8}$$

A high λ gives a relatively flat $p_{\text{cap}} - s$ curve that indicates a relatively homogeneous pore size distribution with fairly equal pore sizes. A small λ gives a relatively steep $p_{\text{cap}} - s$ curve, indicating a wide pore size distribution with many widely differing pore radii.

5.3.3 Darcy's law

A fluid flowing through a porous medium will incur a frictional pressure gradient similar to flow through a tube. For steady laminar flow through a cylindrical pore, the *Hagen-Poiseuille equation* gives:[11]

$$-\frac{\mathrm{d}p}{\mathrm{d}x_{\parallel}} = \frac{8\mu u_{\text{pore}}}{r^2}. \tag{5.9}$$

Here, $x_{\parallel}$ is a coordinate parallel to the flow. The pressure gradient is linear in the average velocity u_{pore} and scales inversely proportional to the square of the channel radius r.

As we have done in section 3.1, we may approximate a porous medium by a bundle of capillaries. Equation (3.7) gives the superficial velocity through a porous medium of porosity ϵ as $U = \epsilon\frac{u_{\text{pore}}}{\tau}$. Here, the tortuosity defined in Eq. (3.2) $\tau = \partial x_{\parallel}/\partial x$ gives the length of the pores compared to the shortest length.

[10] One of the simplest $p_{\text{cap}} - s$ models that approximately works well for many materials is the Brooks-Corey relation $p_{\text{cap}} = p_{\text{t}}(1-s)^{-1/\lambda}$. For $s \approx 0$ this can be linearised to give Eq. (5.7). Another popular relation, the Udell Leverett-J function $J(s) = p_{\text{cap}}/p_{\text{t}} = 1.417s - 2.21s^2 + 1.263s^3$, describes certain rock types. Linearising near $s = 0$ shows this corresponds to $\lambda = 1/1.417 = 0.706$.

[11] The steady incompressible Navier-Stokes equation $0 = \nu\nabla^2\boldsymbol{u} - \nabla p$ for a uni-axial flow velocity $u(r)$ in the x-direction as a function of the radial coordinate r becomes $0 = \frac{\mu}{r}\frac{\mathrm{d}}{\mathrm{d}r}\left(r\frac{\mathrm{d}u}{\mathrm{d}r}\right) - \frac{\mathrm{d}p}{\mathrm{d}x}$. With boundary condition $u(r) = 0$ this is solved by the parabolic profile $u(r) = 2\langle u\rangle\left(1-(r/r)^2\right)$ with the average velocity $u_{\text{pore}} \equiv \frac{1}{\pi r^2}\int u(r)2\pi r dr$ given by Eq. (5.9).

Therefore, *absolute permeability* or *single-phase permeability* of the porous medium reads

$$K \equiv \frac{\mu U}{\mathrm{d}p/\mathrm{d}x} = \frac{\lambda}{1+\lambda}\frac{\epsilon}{8\tau^2} r_{\max}^2 \tag{5.10}$$

where we used Eq. (5.8) (with $s = 1$, for all pores filed with liquid) to replace r^2 with an average value. This will only give a rough numerical approximation,[12] but it does show the expected dependencies with pore size, porosity, and tortuosity.

The linear dependence of superficial velocity and pressure gradient, with a proportionality constant K/μ, is called *Darcy's law*.

5.3.4 Relative permeability

For a porous medium consisting of cylindrical channels, Eq. (3.13) gave $\tau^2 \approx \epsilon^{-1}$ so the permeability becomes proportional to ϵ^2. If a static gas phase is also present besides the flowing liquid phase, the available pore fraction for the liquid becomes ϵs. Furthermore, for $\lambda \gg 1$, another factor s is added to give

$$\boxed{-\frac{\mathrm{d}p_\mathrm{l}}{\mathrm{d}x} = \frac{\mu U_\mathrm{l}}{Kk},} \tag{5.11}$$

where *the relative permeability*

$$k = s^3. \tag{5.12}$$

The *total permeability* Kk is defined by Eq. (5.11).[13]

5.3.5 An equation for s

The water saturation s will be highest at the catalyst layer at $x = 0$, where water is produced, and lowest at the gas channel at $x = L$, where water is removed. Therefore, following Eq. (5.7), the capillary pressure will be highest near the catalyst layer. This pushes water towards the flow channel, in what is called *capillary action*. To reduce the exposure of the hydrophobic material to water, a flow is established to move the water out.

Taking the spatial derivative of Eq. (5.5), assuming $\mathrm{d}p_\mathrm{g}/\mathrm{d}x \ll \mathrm{d}p_\mathrm{l}/\mathrm{d}x$, and inserting Eqs. (5.7) and (5.11) gives the following differential equation for the water saturation

$$\boxed{\frac{\mathrm{d}s}{\mathrm{d}x} = -\frac{\lambda\mu}{p_\mathrm{t}K}\frac{U_\mathrm{l}}{s^3}.} \tag{5.13}$$

[12] For a porous medium consisting of spheres of diameter d_p, the often-used Cozeny-Karman relation $K = \frac{\mathrm{d}_\mathrm{p}^2\epsilon^3}{180(1-\epsilon)^3}$ is obtained by inserting into Eq. (5.9) the hydraulic pore radius $r = \frac{\epsilon d_\mathrm{p}/2}{1-\epsilon}$ and $\tau = 180/32 \approx 5.6$.

[13] Several admittedly heuristic arguments have led to Eq. (5.12). Therefore, unsurprisingly, various other results can be found in the literature; for example, Eq. (5.12) but with the power 3 replaced with anywhere between 2 and 8 [17].

This shows how the liquid saturation s will decrease in the liquid flow direction. The decrease will be more rapid for larger flow velocities and higher liquid viscosity, particularly at low liquid saturations near $s = 0$. A larger permeability and threshold pressure decrease the variation in the saturation. As expected, the liquid saturation decreases in the x-direction, away from the catalyst layer.

Assuming that all the produced water leaves in liquid form through the diffusion layer, so neglecting water vapour and transport through the membrane, Faraday's law gives

$$U_\mathrm{l} = \frac{j\mathcal{V}_m}{2F}, \tag{5.14}$$

where, at ambient conditions, $\mathcal{V}_m \approx 1.8 \cdot 10^{-5}$ m^3/mol is the molar volume of liquid water and $n = 2$ electrons are consumed per water molecule produced, according to Eq. (5.2). Inserting into Eq. (5.13) gives

$$\frac{\mathrm{d}s}{\mathrm{d}\,(x/L)} = -\frac{j/J_\mathrm{c}}{s^3}. \tag{5.15}$$

Here the characteristic capillary current density

$$J_\mathrm{c} = \frac{p_\mathrm{t} K}{\lambda\mu L}\frac{2F}{\mathcal{V}_m} \approx \frac{\gamma|\cos\vartheta|}{2\mu(1+\lambda)}\frac{\epsilon}{\tau^2}\frac{F}{\mathcal{V}_m}\frac{r_\mathrm{max}}{L} \approx 3\cdot 10^{10}\frac{r_\mathrm{max}}{L}\ \mathrm{A/m^2}, \tag{5.16}$$

where in the second expression, we used Eqs. (5.6) and (5.10). In the final expression we used $\mathcal{V}_\mathrm{m} = 1.8 \cdot 10^{-5}$ m^3/mol and $\mu = 4.7 \cdot 10^{-3}$ Pas for water at 60 °C and 1.2 bar, $\gamma|\cos\vartheta| = 0.05$ Pas, and $\frac{\epsilon}{(1+\lambda)\tau^2} \approx 0.1$. A typical diffusion layer pore size $r_\mathrm{max} \approx 10$ µm and thickness $L \approx 300$ µm gives $L/r_\mathrm{max} \approx 30$, so that along its width only a few dozen of the largest pore size fit into the diffusion layer. This makes $J_\mathrm{c} \approx 10^9$ A/m^2 and at typical fuel cell current densities $j = (1-3)\cdot 10^4$ A/m^2 we see that $j \ll J_\mathrm{c}$.

To determine a boundary condition for Eq. (5.15), we consider the water droplets illustrated in Fig. (5.8) on the surface of the diffusion layer. If these are sufficiently larger, their capillary pressure is small so that Eq. (5.7) gives at the channel-diffusion layer interface[14]

$$s(x = L) = 0. \tag{5.17}$$

5.3.6 A solution for s

Solving Eq (5.13) with boundary condition (5.17) gives

$$\boxed{s(x) = \left(\frac{4j}{J_\mathrm{c}}\left(1 - \frac{x}{L}\right)\right)^{1/4}, \quad \text{for } j \ll J_\mathrm{c}.} \tag{5.18}$$

[14] We assume the droplet radius $r_d \gg r_\mathrm{max}$ so their Laplace pressure $p_\mathrm{cap} = 2\gamma/r_d \ll p_\mathrm{t}$ will be negligible. Neglecting any frictional or kinetic pressure drops between inside and outside, we can assume the same holds just inside the porous medium.

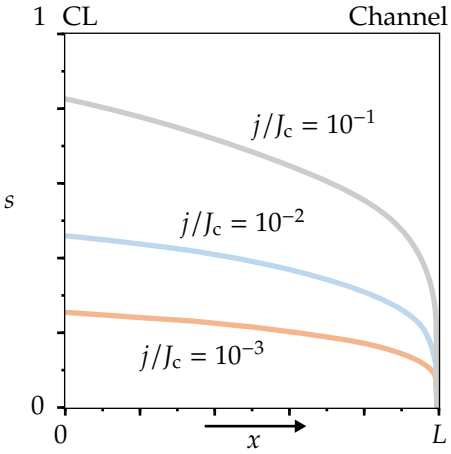

Figure 5.10: *The water saturation* $s(x) = \left(\frac{4j}{J_c}\left(1 - \frac{x}{L}\right)\right)^{1/4}$ *of Eq.* (5.18) *for various* j/J_c. *The boundary condition* $s(x = L) = 0$ *near the gas channel is associated with a large pressure drop due to the low permeability* $k = s^3$. *To maintain a low liquid saturation* $s < 0.25$ *everywhere requires* $j/J_c \lesssim 0.75$.

This solution is shown in Fig. 5.10 for various values of j/J_c. A large decrease in the water saturation can be seen close to the gas channel at $x = L$. The low water saturation leads to a lower permeability that induces a large frictional pressure drop. Therefore, the saturation strongly decreases towards the gas channel.

The main disadvantage of a high saturation is that oxygen transport will be hindered. Since the oxygen solubility and diffusivity are low in water, the sustainable diffusion flux of oxygen through water is orders of magnitude lower. In the next section, we will consider the effect of water on the diffusion of oxygen in the diffusion layer.

5.3.7 Effective oxygen diffusivity

Without water present, an oxygen diffusion flux $N = D(c_L - c_0)/L$ can be sustained for an oxygen concentration difference $c_L - c_0$ over the diffusion layer of thickness L. Here $D \approx \epsilon^{1+\mathcal{B}} D_m$, as given by Eq. (3.14), is lower than the molecular diffusion coefficient D_m due to porosity ϵ and tortuosity τ. When the oxygen concentration vanishes in the catalyst layer, a limiting current density arises. Without any water present, it reads

$$j_{lim0} = \frac{4FDc_L}{L}, \tag{5.19}$$

where Eq. (5.2) gives that $n = 4$ electrons are converted per oxygen molecule. With a typical oxygen concentration $c_L \approx 10$ mol/m^3 in air at typical elevated temperature and pressure, $D \approx 10^{-5}$ m^2/s, and $L = 300$ µm, this gives about 13 A/m^2, several

times higher than typical fuel cell current densities.

The increase in water saturation s further decreases the volume fraction $1 - s$ of the pores available for gas diffusion, and increases the tortuosity. We will model this with a modified diffusivity $D\,(1-s)^m$, similar to the Bruggeman correction of Eq. (3.14), with a power m depending on the geometry of the medium. This gives for the molar oxygen flux $N = D\,(1-s)^m \frac{\mathrm{d}c}{\mathrm{d}x}$. Integrating over the entire diffusion layer gives $j = 4FD_{\text{eff}}\frac{c_L - c_0}{L}$, where

$$\frac{D_{\text{eff}}}{D} = \frac{1}{L}\int_0^L (1-s)^{-m}\,dx. \tag{5.20}$$

Inserting Eq. (5.18) does not give simple expressions for D_{eff}. Instead, we provide the following approximation[15]

$$\frac{D_{\text{eff}}}{D} \approx \left(1 - (1.6j/J_{\text{c}})^{1/4}\right)^{-m}. \tag{5.21}$$

We have $j_{\text{lim}} = \frac{D_{\text{eff}}}{D} j_{\text{lim0}}$ where D_{eff} by Eq. (5.21) depends on $j_{\text{lim}}/J_{\text{c}}$. Experiments show that m varies over a wide range between different materials. Taking $m = 4$ we can solve this to give

$$\boxed{j_{\text{lim}} = \frac{j_{\text{lim0}}}{\left(1 + \left(\frac{1.6 j_{\text{lim0}}}{J_{\text{c}}}\right)^{1/4}\right)^4}.} \tag{5.22}$$

This solution is plotted in Fig. 5.11.

As estimated at the beginning of this section, typical 'dry' limiting current densities j_{lim0} are only several times higher the current densities normally used in fuel cells. Therefore, to avoid significant concentration overpotentials, the presence of water cannot lower the limiting current density by much.

To avoid the limiting current density dropping below, say, 50 % of its 'dry' value $j_{\text{lim0}} \sim 10^5$ A/m^2, according to Eq. (5.22) $J_{\text{c}} \gtrsim 10^3 j_{\text{lim0}} \sim 10^8$ A/m^2 is required. Equation (5.16) then gives $L/r_{\text{max}} \lesssim 300$. Therefore, avoiding a too-low limiting current density requires a diffusion layer that is less than a few hundred times its maximum pore radius. With typical values $r_{\text{max}} \sim 10$ µm and $L = 300$ µm, this is taken into consideration in the design of modern diffusion layers.

5.4 Flooded agglomerate model

5.4.1 Ohmic and diffusion limitations

Figure 5.13 shows an image of a catalyst particle in a PEM fuel cell cathode. It contains fine carbon particles to conduct electrons, ionomer to conduct ions, and plat-

[15] This is obtained by expanding Eq. (5.18) to first order in $(4j\,(1-x/L)/J_{\text{c}})^{1/4}$ to write $(1-s)^{-m} \approx 1 + m\,(4j\,(1-x/L)/J_{\text{c}})^{1/4}$ and integrating to give $\frac{D_{\text{eff}}}{D} \approx 1 + \frac{4m}{5}(4j/J_{\text{c}})^{1/4}$. With $\frac{4}{5}4^{1/4} \approx 1.6^{1/4}$ this is the first-order approximation of Eq. (5.21).

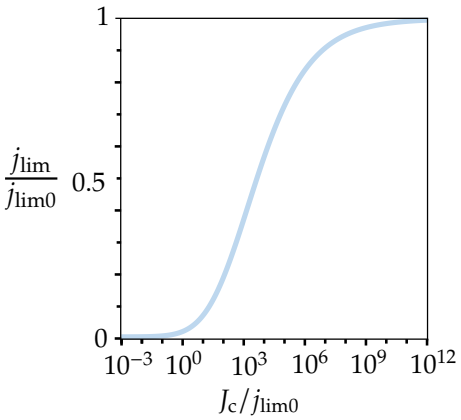

Figure 5.11: *The solution* $j_{lim} = \frac{j_{lim0}}{\left(1+\left(\frac{1.6 j_{lim0}}{J_c}\right)^4\right)^4}$ *of Eq.* (5.22) *plotted as a function of* j_{lim0}/J_c.

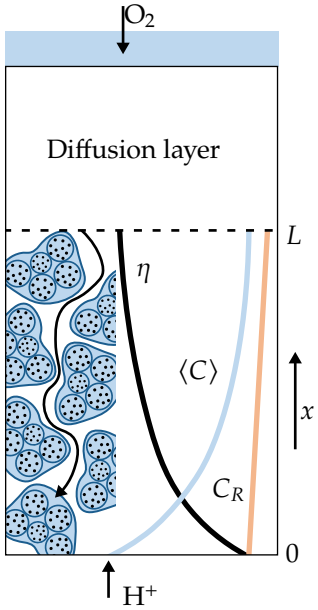

Figure 5.12: *A schematic of the cathode catalyst layer structure and profiles of the overpotential* η *and oxygen concentration* C. *Note: this is not to scale; the catalyst layer is typically much thinner than the diffusion layer. The flooded agglomerate model consists of agglomerates of several carbon-supported catalyst particles flooded by water from the reaction. The dissolved oxygen concentration at the agglomerate surface* C_R, *see Fig. 5.13, is in equilibrium with the approximately constant gas phase concentration. Near* $x = 0$, *the reaction is fastest because the overpotential* η *is highest.*

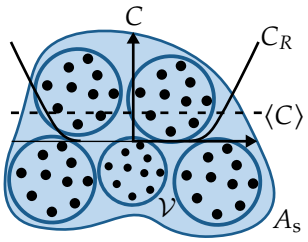

Figure 5.13: *A schematic illustration of an agglomerate of PEM fuel cell carbon-supported catalyst particles with volume $\mathcal{V}$ and surface area A_s. The black catalyst particles are surrounded by a carbon/ionomer/binder mixture. The dissolved oxygen concentration decreases from its value C_R at the particle surface towards the interior of the particle, due to the oxygen reduction reaction.*

inum nanometre-sized particles to increase the reactivity. These carbon-supported particles are typically a few to tens of nanometres in size, but they can agglomerate to agglomerates of a few or many particles in size extending to tens to hundreds of nanometres. The water produced in the reaction of Eq. (5.2) floods the pores of these carbon particles and often the inter-particle space within an agglomerate. The carbon particles will be flooded with the water produced in the reaction, hence the term *flooded agglomerate model*. As a consequence, for oxygen to reach the catalyst particles inside these agglomerates, it first has to dissolve and then diffuse inwards while reacting.

Both the concentration and the diffusivity of oxygen drop dramatically when dissolved in water. Therefore, the intra-agglomerate pores ideally remain dry to allow oxygen to diffuse towards the agglomerates in the gas phase. *Flooding* of the catalyst layer, when the inter-agglomerate space also fills with water, makes it impossible for the oxygen to reach much of the catalyst layer. On the other hand, flooding of the agglomerates themselves is hard to avoid and less of an issue because of their much smaller size. Due to the good hydration of the ionomer and their small size, ohmic limitations inside the agglomerates can be neglected. However, limitations of oxygen mass transfer may have to be considered inside the water-filled agglomerate.

On the other hand, ohmic limitations may arise over the catalyst layer's thickness. This leads to the profiles shown in Fig. 5.12 where we consider variation in the overpotential η and the average oxygen concentration $\langle C \rangle$ inside the agglomerates, but the concentration C_R at the surface is assumed to be constant throughout. The reason is that this surface is in equilibrium with the oxygen concentration in the gas phase, which will be constant throughout the catalyst layer.[16]

[16]By Henry's law, the oxygen concentration in the liquid phase at the interface with the gas is given by $C_R = Hp_{O_2}$ with p_{O_2} the partial pressure of oxygen in the gas. Here H is Henry's constant.

5.4.2 Model equations

To describe the activation overpotential, we consider Tafel kinetics, first-order in the oxygen concentration. We start from the porous electrode equation Eq. (3.62), which we modify to:

$$\mathrm{e}^{\eta/b} = \mathcal{E}_\mathrm{a}\frac{\kappa}{a j_*}\eta''. \tag{5.23}$$

Here, $\mathcal{E}_\mathrm{a} = \langle C\rangle/C_R$ is the agglomerate effectiveness factor. Similar to the approximation $\mathcal{E} = \frac{1}{1+\mathrm{M}}$ introduced in section 3.4.4, in Appendix 5.A we show

$$\mathcal{E}_\mathrm{a} \approx \frac{1}{\sqrt{1+\mathrm{M}_\mathrm{a}^2}}, \tag{5.24}$$

in terms of the agglomerate Thiele modulus M_a. In Eq. (3.56) we obtained the porous-electrode expression $\mathrm{M}^2 = \frac{J_*}{J_D}\mathrm{e}^{\eta_0/b}$, where $J_D \equiv nFDc_0/L$. Analogously, we will use here

$$\mathrm{M}_\mathrm{a}^2 = \mathcal{M}^2\mathrm{e}^{\eta/b}, \text{where } \mathcal{M}^2 = \frac{j_*}{J_D}, \text{and } J_D \equiv nFDa_\mathrm{s}C_0 \tag{5.25}$$

where the effective medium diffusivity D now refers to that inside the agglomerate particle instead of the porous electrode as a whole. Other differences with the porous electrode expressions that we obtained before are:

1. Instead of the overpotential η_0 at the 'entrance' of the electrode, at $x = 0$ near the membrane, we use the overpotential η at the 'entrance' of the agglomerate. Due to ohmic limitations, this overpotential can vary throughout the catalyst layer.

2. Instead of the total exchange current density $J_* = aLj_*$ of the entire electrode, the exchange current density j_* of a single agglomerate particle is used.[17]

3. Instead of the effective-medium electrode thickness L, we use as a length-scale $1/a_\mathrm{s}$, where a_s is the volumetric surface area of a single agglomerate. This is shown to be a sensible replacement in Appendix 5.A.1. For a sphere of radius R this would replace L with $1/a_\mathrm{s} = \frac{4}{3}\pi R^3/4\pi R^2 = R/3$.

Inserting Eqs. (5.24) and (5.25) into Eq. (5.23) gives

$$\eta'' \approx \frac{a j_*}{\kappa}\frac{\mathrm{e}^{\eta/b}}{\sqrt{1+\mathcal{M}^2\mathrm{e}^{\eta/b}}}. \tag{5.26}$$

[17] Here a is now the external area of the agglomerates per total unit volume of the catalyst layer. Considering an agglomerate to be porous, we may further write j_* in terms of the intrinsic exchange current density of a platinum particle times the ratio between the combined platinum surface area, divided by the agglomerate area.

5.4.3 Overpotential

Equation (5.26) can be solved approximately under the assumption $\mathcal{M}^2 e^{\eta_1/b} \ll 1$, so the agglomerate effectiveness factor $\mathcal{E}_a(x = L) \approx 1$. This will be the case at sufficiently strong ohmic limitations, such that the reaction rate at $x = L$ is negligible. We can use a similar solution method as in sections 3.4.3 and 4.4 to give:[18]

$$\boxed{\eta_0 = b\ln\left(\frac{j^2}{2b\kappa a j_*}\left(1+\frac{j^2}{8b\kappa a J_D}\right)\right) \approx \begin{cases} 2b\ln\left(\frac{j}{\sqrt{2b\kappa a j_*}}\right) & \left(\frac{j^2}{8b\kappa a J_D} \ll 1\right) \\ 4b\,\ln\left(\frac{j}{\sqrt{4b\kappa a\sqrt{j_* J_D}}}\right) & \left(\frac{j^2}{8b\kappa a J_D} \gg 1\right) \end{cases}} \tag{5.27}$$

The agglomerate effectiveness factor at $x = 0$ reads

$$\mathcal{E}_{a0} = \frac{1}{\sqrt{1+\mathcal{M}^2 e^{\eta_0/b}}} = \frac{1}{\sqrt{1+\frac{j^2}{2b\kappa a J_D}\left(1+\frac{j^2}{8b\kappa a J_D}\right)}}, \tag{5.28}$$

so that the top and bottom case correspond to $\mathcal{E}_{a0} \approx 1$ and $\mathcal{E}_{a0} \ll 1$, respectively.

In the top case, the agglomerates are used effectively ($\mathcal{E}_{a0} \approx 1$), and we obtain the same result as in section 3.4.3. In this case, ohmic limitations over the catalyst layer thickness lead to a doubling in the Tafel slope to $2b$ and an apparent exchange current density $\sqrt{2b\kappa a j_*}$.

In the bottom case, besides these ohmic limitations, additional internal diffusion limitations lead to a further doubling or quadrupling in the Tafel slope to $4b$. [21] The apparent exchange current density is replaced by a geometric average of a resistive current density $4b\kappa a$ and a geometrical average of a diffusive current density $J_D = \frac{a_s^2}{a} nFDC_R$ and j_*. Because of the very weak dependence on j_* catalyst improvements, they only very weakly improve performance in this undesirable regime. The predicted doubling and quadrupling of the Tafel slope is compared to experimental data in Figure 5.14.

The quadrupled Tafel slope regime is obviously not a desirable operational regime for a fuel cell. To avoid this, under all operating conditions, the Thiele moduli must remain small.

5.4.4 Example calculation

Using the following typical values for a PEM fuel cell [14]: a diffusivity $D = 5 \cdot 10^{-9}$ m^2/s and solubility $C_R = 7.6\,mol/m^3$ of oxygen in water at elevated pressure, $b = 0.05$

[18] The chain rule gives $\frac{d}{dx} = \frac{d\eta}{dx}\frac{d}{d\eta}$ so that $\eta'' = \eta'\frac{d\eta'}{d\eta} = \frac{1}{2}\frac{d\eta'^2}{d\eta}$. The integral $\int \frac{e^{\eta/b}d\eta}{\sqrt{1+\mathcal{M}^2 e^{\eta/b}}} = \frac{2b\sqrt{1+\mathcal{M}^2 e^{\eta/b}}}{\mathcal{M}^2}$ so integrating from η_0 to η_1, assuming $\mathcal{M}^2 e^{\eta_1/b} \ll 1$, gives $\eta_0'^2 \approx \frac{4aj_*b}{\kappa}\frac{\sqrt{1+\mathcal{M}^2 e^{\eta_0/b}}-1}{\mathcal{M}^2}$. The boundary condition (3.B.101) gives $|\eta_0'| = jL/\kappa$, resulting in Eq. (5.27).

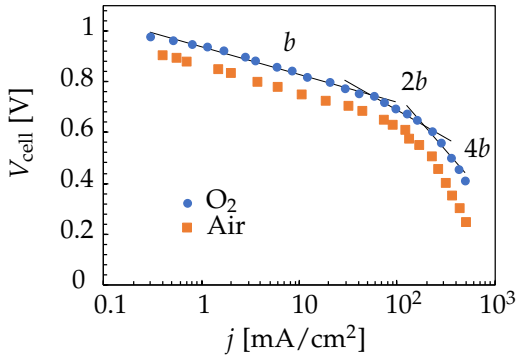

Figure 5.14: *Experimental data for a phosphoric acid fuel cell [18] with a catalyst loading of 0.63 mg Pt cm^{-2} and catalyst layer thickness of 200 µm on Vulcan XC-72R containing 50 wt% PTFE and in 105 wt% H_3PO_4. The potential as a function of current density seems to show a doubling and then a quadrupling in Tafel slope per decade, from 110 mV, to 220 mV, to 440 mV [21].*

V, $n = 4$, and $aj_* = 4 \cdot 10^4$ A/m^3, we find for an agglomerate radius of R= 10^{-7} m that $\mathcal{M}^2 = \frac{aj_* R^2}{9nFDC_R} \sim 3 \cdot 10^{-10}$. To reach a Thiele modulus squared $\mathrm{M}_\mathrm{a}^2 = \mathcal{M}^2 \mathrm{e}^{\eta/b}$ of the order unity requires in this case $\eta \approx 22b \approx 1$ V. Such high overpotentials will never be used, since there will be no useful potential left in this case. Therefore, modern catalyst layers in which agglomerates are of the order of 100 nm in radius or smaller should be free of diffusion limitations and should not show the Tafel slope quadrupling of Figure 5.14.

5.5 Summary

- The capillary pressure inside a porous medium is given by the Young-Laplace equation as $p_{\mathrm{cap}} = p_\mathrm{l} - p_\mathrm{g} = \frac{2\gamma|\cos\vartheta|}{r} = \frac{2\gamma|\cos\vartheta|}{r_{\max}}\left(1 + \frac{1-s}{\lambda}\right)$ (5.5). The second equation linearises its dependence on saturation $s \approx 1$. Combined with Darcy's equation $-\frac{\mathrm{d}p_\mathrm{l}}{\mathrm{d}x} = \frac{\mu U_\mathrm{l}}{Kk}$ (5.11) and a relative permeability $k = s^3$ this gives $\frac{\mathrm{d}s}{\mathrm{d}x} = -\frac{\lambda\mu}{p_\mathrm{t} K}\frac{U_\mathrm{l}}{s^3} = -\frac{j/j_\mathrm{c}}{Ls^3}$ (5.13), which describes how s decreases away from the catalyst layer.
- If the increase in s decreases the local effective gas diffusivity from D to $D\,(1-s)^4$, the limiting current density is decreased from $j_{\mathrm{lim}0}$ to $\frac{j_{\mathrm{lim}0}}{\left(1+\left(\frac{1.6 j_{\mathrm{lim}0}}{j_\mathrm{c}}\right)^{1/4}\right)^4}$ (5.22).
- Assuming ohmic limitations over the thickness of the catalyst layer, where the gas phase ensures high reactant diffusivity, and potential diffusion lim-

itations inside the flooded agglomerates, which are small enough to avoid ohmic limitations, we obtained an analytical expression for the overpotential $\eta_0 = b\ln\left(\frac{j^2}{2b\kappa a j_*}\left(1+\frac{j^2}{8b\kappa a J_D}\right)\right)$ (5.27). The Tafel slope doubled by the ohmic limitations gets doubled again in case of diffusion limitations inside the agglomerates.

Exercise 5.1

A limiting current arises in the cathode of a PEM fuel cell when the oxygen concentration reaches zero at the catalyst layer. Assume that the only significant transport resistance is in the diffusion layer of thickness L, where oxygen has to diffuse through air and water vapour with an effective diffusivity, D.

a. Give an expression for the limiting current associated with this diffusion layer in terms of the oxygen concentration c_L at the gas channel.

b. Give a numerical value for this current density when $D = 10^{-5}\,\mathrm{m^2/s}$, $L = 0.3\,\mathrm{mm}$, and the oxygen concentration is that in air at ambient pressure, or $c_L = 10\,\mathrm{mM}$. (N.B. Regularly much lower limiting currents of the order of $1\,\mathrm{A/cm^2}$ are found. This may be due to an unaccounted-for transfer resistance, like that associated with the dissolution of oxygen.)

c. In case of two resistances in series, with mass transfer coefficients k_1 and k_2 give an expression for the overall mass transfer coefficient (remember that the mass transfer coefficient is the flux divided by the driving concentration difference).

d. Assume that these mass transfer resistances combine to a single transfer coefficient given by $k=\frac{N}{c_L-c_0}$ with c_L the local concentration of oxygen at the catalyst layer-diffusion layer interface and c_0 the concentration at the catalyst surface where the reaction takes place. Give an expression for the limiting current, including this resistance and that of the diffusion layer.

Exercise 5.2

Equation (5.13) was derived neglecting the friction of the gas phase.

a. Modify Eq. (5.13) to include the effect of the gas pressure gradient.

b. The liquid pressure gradient will dominate for a very low liquid saturation $s \approx 0$, while the gas fraction will be largest for very low values of s. For what saturation s_* will the gas and liquid pressure gradients be equal? Give a formula and fill in the properties of water and air at 60 °C and 1.2 bar to give a numerical value.

Exercise 5.3

Consider a PEM fuel cell cathode catalyst layer with spherical platinum particles with a radius R at a volume fraction φ.

a. Give a formula the volumetric surface area of the catalyst.
b. If the intrinsic exchange current density of a platinum surface for the oxygen reduction reaction is known to be $j_* = 10^{-1}$ A/m^2, the nanoparticles have a radius of $R = 2.5$ nm and are used at a volume fraction of φ=10^{-3} give the effective exchange current density $a j_*$ per unit of total catalyst layer volume.
c. If the catalyst layer has a thickness $L = 5$ µm and is used effectively, given a Tafel slope $b = 50$ mV, what are the expected cathodic activation losses at 1 A/cm^2?
d. What overpotential can be saved when the catalyst layer thickness is increased tenfold and remains fully effective? Give your answer in the form of a formula.
e. If the effective ionic conductivity is 1 S/m, what will be the approximate effectiveness factor when increasing the electrode thickness by a factor of 10?

Exercises 5.4-5.12

Fill in the missing steps in the main text, indicated by the symbol .

*Appendices **

5.A *Generalised Thiele modulus*

5.A.1 *General particle shape*

The Thiele modulus squared $\mathrm{M}^2 = \frac{L^2 k}{D}$ is expressed as the ratio of the *volumetric* reaction rate kC and a characteristic diffusion rate DC/L^2. And we found the effectiveness factor $\mathcal{E} = \frac{\tanh \mathrm{M}}{\mathrm{M}}$ for a planar configuration. In this section, we will generalise this result to apply approximately to any shape. Consider a general volume, V, as shown in Figure 5.13, which has a concentration C_R at the boundary of the volume.
The diffusion-reaction conservation equation inside the particle reads

$$0 = D\nabla^2 C - k C. \tag{5.A.29}$$

The effectiveness factor is defined as the ratio of the average and maximum reaction rates:

$$\mathcal{E} \equiv \frac{\frac{1}{\mathcal{V}} \int k C \, \mathrm{d}\mathcal{V}}{k C_0} = \frac{D \int \nabla^2 C \, \mathrm{d}\mathcal{V}}{k C_0 \, \mathcal{V}} = \frac{D \int \nabla C \cdot d\boldsymbol{A}}{k C_0 \mathcal{V}} \approx \frac{D a_\mathrm{s}}{k} \left. \frac{|\nabla C|}{C} \right|_{\text{surface}}. \tag{5.A.30}$$

In the second equation, we inserted Eq. (5.A.29); in the third, we applied the divergence theorem, and in the final approximation, we assumed that ∇c is constant over the surface of the particle and aligned with the outwards directed $\mathrm{d}\boldsymbol{A}$. This allowed us to replace and introduce the volumetric surface area $a_\mathrm{s} = A/\mathcal{V}$.
Comparing Eq. (5.A.30) with the expression $\mathcal{E} = -\frac{L\, c'/c|_0}{\mathrm{M}^2}$ for the 1D pore case, we see that we can maintain the definition $\mathrm{M}^2 = \frac{L^2 k}{D}$ if we replace L by $1/a_\mathrm{s}$. For a pore of radius R and length L of which only the sides react, we have $a_\mathrm{s} = \frac{\pi R^2}{\pi R^2 L} = 1/L$ as before.
With this replacement, we obtain the generalised Thiele modulus

$$\mathrm{M}^2 = \frac{k}{a_\mathrm{s} D}, \tag{5.A.31}$$

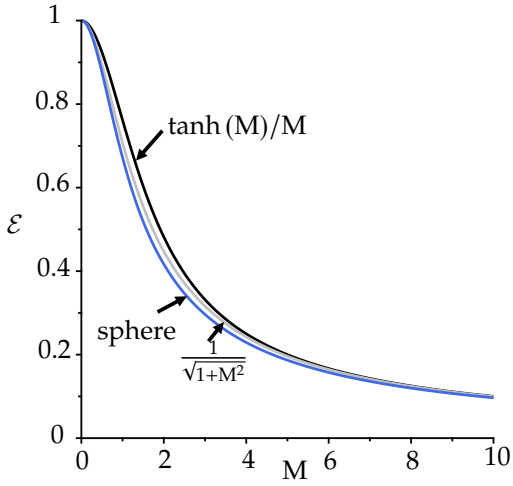

Figure 5.15: *The effectiveness factor* $\mathcal{E} = \frac{\tanh(M)}{M}$ *for a planar configuration (dark blue),* $\frac{1}{M}\left(\frac{1}{\tanh(3M)} - \frac{1}{3M}\right)$ *for a sphere and an approximation* $\frac{1}{\sqrt{1+M^2}}$ *showing only very small differences using the generalised Thiele modulus of Eq.* (5.A.31).

where we also inserted the reaction coefficient $k = \hbar/a_s$ per unit external surface area.
For a spherical particle with radius R we have $a_s = \frac{4\pi R^2}{\frac{4}{3}\pi R^3} = \frac{3}{R}$ so that with $L = R/3$ we have $M^2 = \frac{R^2\hbar}{9D} = \frac{Rk}{3D}$.

5.A.2 *Effectiveness factor approximation*

Besides the planar case we considered previously, the reaction-diffusion equation can also be solved exactly in, for example, a sphere. The result is for this is shown in Figure 5.15. It can be seen that the curves are very similar. This allows us to use the planar result $\mathcal{E} = \frac{\tanh(M)}{M}$ with a reasonable degree of accuracy, also for the case of a sphere using the generalised Thiele modulus of Eq. (5.A.31).
Figure 5.15 also shows the approximation

$$\mathcal{E} \approx \frac{1}{\sqrt{1+M^2}}. \tag{5.A.32}$$

This result also tends to the correct limits $\mathcal{E} \approx 1$ when $M \ll 1$ and $1/M$ when $M \gg 1$. It can be seen that this approximation is also quite close to both the spherical and planar results. Usually, this approximation is sufficiently accurate, especially since the exact particle shape is often not well known.

5.A.3 *Dimensionless flooded agglomerate model*

Eq. (5.23) in the dimensionless notation of Appendix 3.B reads

$$\mathrm{e}^{\bar{\eta}} = \mathcal{E}_\mathrm{a} \frac{\bar{j}_*}{\bar{j}_\kappa} \bar{\eta}'', \tag{5.A.33}$$

and Eq. (5.26) becomes

$$\bar{\eta}'' \approx \frac{\bar{j}_\kappa}{\bar{j}_*} \frac{\mathrm{e}^{\bar{\eta}}}{\sqrt{1+\mathcal{M}^2 \mathrm{e}^{\bar{\eta}}}}. \tag{5.A.34}$$

The chain rule gives $\frac{\mathrm{d}}{\mathrm{d}\bar{x}} = \frac{\mathrm{d}\bar{\eta}}{\mathrm{d}\bar{x}} \frac{\mathrm{d}}{\mathrm{d}\bar{\eta}}$ so that $\bar{\eta}'' = \bar{\eta}' \frac{\mathrm{d}\bar{\eta}'}{\mathrm{d}\bar{\eta}} = \frac{1}{2} \frac{\mathrm{d}\bar{\eta}'^2}{\mathrm{d}\bar{\eta}}$. The integral $\int \frac{\mathrm{e}^{\bar{\eta}} d\bar{\eta}}{\sqrt{1+\mathcal{M}^2 e^{\bar{\eta}}}} = \frac{2\sqrt{1+\mathcal{M}^2 \mathrm{e}^{\bar{\eta}}}}{\mathcal{M}^2}$ so that integrating from $\bar{\eta}_0$ to $\bar{\eta}_1$ assuming $\mathcal{M}^2 \mathrm{e}^{\bar{\eta}_1} \ll 1$ gives

$$\bar{\eta}_0'^2 \approx \frac{4\bar{j}_\kappa}{\bar{j}_*} \frac{\sqrt{1+\mathcal{M}^2 \mathrm{e}^{\bar{\eta}_0}} - 1}{\mathcal{M}^2}. \tag{5.A.35}$$

The boundary condition (3.B.101) gives $\bar{\eta}_0'^2 = \bar{j}_\kappa^2$ resulting in

$$\bar{\eta}_0 = \ln\left(\frac{\bar{j}_\kappa \bar{j}_*}{2}\left(1 + \frac{\bar{j}_\kappa \bar{j}_* \mathcal{M}^2}{8}\right)\right) \approx \begin{cases} \ln\left(\frac{\bar{j}_\kappa \bar{j}_*}{2}\right) & \left(\frac{\bar{j}_\kappa \bar{j}_* \mathcal{M}^2}{8} \ll 1\right), \\ 2\ln\left(\frac{\bar{j}_\kappa \bar{j}_* \mathcal{M}}{4}\right) & \left(\frac{\bar{j}_\kappa \bar{j}_* \mathcal{M}^2}{8} \gg 1\right). \end{cases} \tag{5.A.36}$$

Inserting dimensional quantities again gives Eq. (5.27).

Chapter 6

Electrolysers

In this chapter, we consider the modelling of electrolysers and, in particular, the effect that gas evolution has on the vertical current distribution and the electrolyte flow. We start with the rise of a single bubble, its relation to the gas fraction, and the impact of the gas fraction on conductivity. Next, we develop a model for the vertical gas distribution and its impact on the current density. Finally, we consider how gas bubbles can be used to drive a circulating electrolyte flow, which is useful for transporting heat and bubbles out of the cell.

6.1 Introduction

Throughout the twentieth century various alkaline water electrolysers have been used to generate hydrogen, in particular near hydropower plants. While steam methane reforming has taken over most hydrogen production, a clear comeback of water electrolysis seems imminent.[1]

The term electrolyser generally refers to an electrolytic cell in which current is used to drive a reaction. In this chapter, we will primarily focus on electrolysers that produce, or *evolve*, gases.[2] We will focus here on alkaline water electrolysers, for the production of hydrogen. However, the phenomena we will model also apply to various other types of gas-evolving electrochemical cells and devices. Figure 6.1 shows two types of electrolyser designs: the traditional one on the right is more and more replaced by a *zero-gap* configuration in which there is no space between

[1]Other processes are most cost-effective, or even only possible, using electrolysis. An example is the *chlor-alkali process*. Here, NaCl is converted in an electrochemical cell into chlorine gas, hydrogen, and NaOH. Sodium chlorate, potassium chlorate, and several other organic compounds are also produced through electrolysis. The electrolytic production of metals, or *electrometallurgy*, is perhaps most well-known for making aluminium from alumina Al_2O_3 in the *Hall-Héroult process*.

[2]In many industrially relevant electrolysers, gases are evolved, which can have deleterious effects on the process. In the production of aluminium, for example, in the *anode effect*, a bubble cloud covers the anode. This increases the ohmic losses due to their insulating nature and increases the activation losses by partially covering the electrode area.

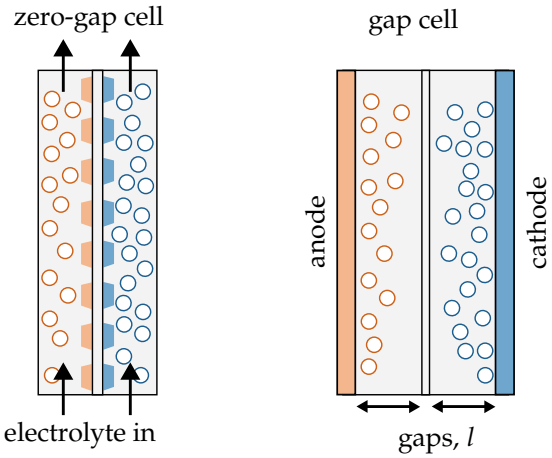

Figure 6.1: *The left-hand figure shows an electrolyser in a zero-gap configuration where perforated electrodes are positioned directly adjacent to the diaphragm to reduce ohmic losses. The right-hand figure shows the traditional configuration with gaps between planar electrodes and the diaphragm.*

the electrodes and the diaphragm to reduce ohmic overpotentials, as shown on the left-hand side of Fig. 6.1.

Often, a pump is used to drive a liquid flow through the cell. This is beneficial, first and foremost, in transporting away the heat generated in the reaction. Sometimes, the natural lift induced by the bubbles generates this liquid flow.[3] In section 6.5, we will consider how to model this. However, first, we will consider how to predict the average gas fraction in electrolysers, not through the use of computational fluid dynamics as in Figure 6.2, but through simplified one-dimensional analytical modelling.

6.2 A current distribution model

So far, we have only considered one-dimensional models with a spatial coordinate in the direction of the current. Here, we will consider variation in the direction normal to the current, to model the gas fraction as a function of height. In the next chapter on flow batteries, we will develop a quasi-two-dimensional model that allows for the description of variations in the direction parallel to the current *and* the flow.

[3]This is, for example, typically the case in chlor-alkali electrolysers where liquid flow is essential to improve mass transport. Also, a few alkaline water electrolysers that operate at near-atmospheric pressure make use of this principle.

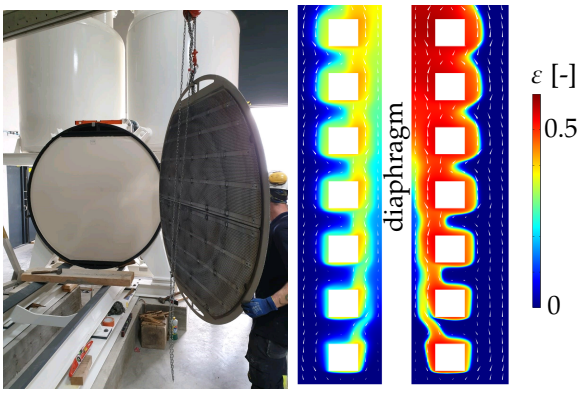

Figure 6.2: *A Nickel-plated perforated plate electrode of roughly 2 m^2 being lifted into a NEL alkaline water electrolyser stack (left, used with permission from Lhyfe). A 2-3 mm gap separates the diaphragm from the electrodes. There is a larger space behind the electrodes. About 230 cells are stacked in series to make up a roughly 10-metre-long electrolyser. A pump is used to flow liquid through the cell with a small velocity of $W_l \approx 0.3$ mm/s. This design is made for a relatively low current density of 750-2000 A/m^2. On the right is a 2D mixture-model simulation of the gas fraction at $j = 10^4$ A/cm^2 in the first few millimetres. The electrode, diaphragm, and gap thickness are all 0.5 mm. We used the COMSOL Multiphysics® software to perform the modelling [8]. Simulations by W.L. v.d. Does.*

6.2.1 Cell model

We write the cell model of Eq. (1.36), similar to Eq. (4.7) as

$$V_{\text{cell}} \approx V_{\text{eq}} - \left(\eta + \frac{jl}{\kappa} + \frac{jl_{\text{eff}}}{\kappa_{\text{m}}}\right), \tag{6.1}$$

where η is the sum of the combined anode and cathode activation overpotentials.[4] Here, l and κ are the thickness and effective conductivity of the bubble-filled gap under consideration. The final term in Eq. (6.1) gives additional ohmic losses, for example in the diaphragm or a gas-free electrolyte layer, in terms of an equivalent thickness l_{eff} of a layer with conductivity κ_{m}.[5]

We recall that electrolytic cells have $V_{\text{cell}} < 0$, so the various voltage losses increase the cell potential magnitude. This is different from the galvanic batteries and fuel cells considered in the previous sections.

We will use term jl/κ in Eq. (1.35) to describe the electrolyte ohmic drop over the 'gaps' between the electrode and diaphragm, or the space behind the electrodes in

[4]For planar electrodes $\eta = \eta_{\text{a}} - \eta_{\text{c}}$, where $\eta_{\text{a}} > 0$ and $\eta_{\text{c}} < 0$. Ohmic losses in cables or connections that only depend on the total current may also be added here.

[5]For example, using Eq. (3.12), a diaphragm with thickness l_{d}, porosity ϵ, and tortuosity τ gives an ohmic drop $jl_{\text{eff}}/\kappa_{\text{m}} = jl_{\text{d}}\tau^2/\epsilon\kappa_{\text{m}}$ so $l_{\text{eff}} = l_{\text{d}}\tau^2/\epsilon$.

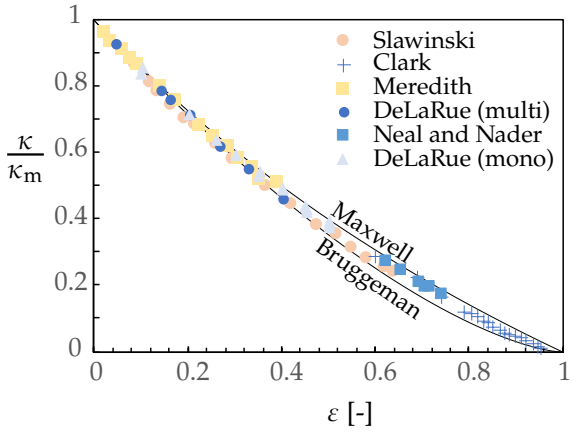

Figure 6.3: *Experimental data from various sources on the relative effective conductivity κ/κ_m of spherical packings of insulating spheres, emulsions (Meredith), and foams (Clark) [24]. A comparison is shown with the relations, Eq.* (6.2)*, of Maxwell $\left(\frac{1-\varepsilon}{1+\varepsilon/2}\right)$ and Bruggeman $\left((1-\varepsilon)^{1+\mathcal{B}}\right)$ for $\mathcal{B} = 1/2$.*

a zero-gap configuration. See Fig. 6.2. The rest of the ohmic drop, including that in the diaphragm, is included in the final term jl_{eff}/κ_m.

The space we consider will horizontally be filled homogeneously with bubbles at a volumetric gas fraction ε. Similar to the solid material in a porous electrode, the presence of gas will reduce the effective conductivity from its molecular value κ_m. Analogous to Eq. (3.25), we write[6]

$$\frac{\kappa}{\kappa_m} = \begin{cases} (1-\varepsilon)^{1+\mathcal{B}} & \text{Bruggeman,} \\ \frac{1-\varepsilon}{1+\varepsilon/2}. & \text{Maxwell} \end{cases} \tag{6.2}$$

We have previously considered Bruggeman's relation to describe polydisperse spherical particles using $\mathcal{B} = 1/2$. The second expression[7] is often used to model the thermal conductivity of porous media. As shown in Fig. 6.3, both expressions give similar results[8] and compare reasonably well with experiments.

[6]Mind you that in a porous electrode, the porosity ϵ denotes the volume fraction available for the electrolyte, while in the presence of a gas fraction ε this is $1-\varepsilon$.

[7]It is named after James Clerk Maxwell and derived for a dilute random distribution of spherical particles. It has analogues for the refractive index: the Lorentz-Lorenz equation named after Hendrik Antoon Lorentz and Ludvig Lorenz; and permittivity: the Clausius-Mossotti relation and the mixing formula derived by Maxwell Garnett, whose father named him after his friend J.C. Maxwell.

[8]At low gas fractions, their predictions overlap for $\mathcal{B} = 1/2$, as they have the same first-order Taylor expansion $1 - 3\varepsilon/2$. At high gas fractions nearing 1, both results tend to 0.

6.2.2 The bubble rise velocity

Bubbles coming from electrodes tend to be small, typically of the order of 0.1 mm.[9] Due to surface tension, such small bubbles are approximately spherical. Buoyancy will cause an upwards *slip* velocity w_s, defined as the difference between the gas bubble velocity w_g and the liquid velocity

$$w_s \equiv w_g - w_l. \tag{6.3}$$

We will use a w to denote velocity components in the vertical z-direction, in keeping with the fluid dynamics notation to write the velocity vector $\boldsymbol{u} = u\hat{\boldsymbol{x}} + v\hat{\boldsymbol{y}} + w\hat{\boldsymbol{z}}$. Superficial velocities will be denoted by capitals as before, so the vertical superficial gas velocity $W_g = w_g\varepsilon$ and the liquid superficial velocity $W_l = (1-\varepsilon)w_l$.

For small enough bubbles, the Reynolds number $\mathrm{Re} \equiv \frac{\rho w_s(2R)}{\mu} \lesssim 1$, and we can use the Stokes drag force expression of Eq. (2.C.71):[10]

$$F_D = 6\pi\mu R w_s, \tag{6.4}$$

for the drag force magnitude, with μ the dynamic viscosity of the liquid. The buoyancy force $\frac{4\pi R^3}{3}\rho g$ is proportional to the liquid density ρ. Neglecting the gravitational force on the bubbles, equating these forces, we find for the *Stokes rise velocity*

$$w_S = \frac{2gR^2}{9\nu}, \tag{6.5}$$

where $\nu = \mu/\rho$ is the liquid kinematic viscosity.

Inserting, for example, $2R = 0.1$ mm,[11] $\nu = 10^{-6}$ m^2/s, and $g = 9.8$ m/s^2 gives a slip velocity of $w_S \approx 5$ mm/s. This corresponds to a Reynolds number of 0.5, for which the Stokes drag force expression of Eq. (6.4) can still be used to a reasonable approximation.

6.3 One-dimensional model

The general conservation equation (2.1) for the volume of gas becomes in steady-state $\nabla \cdot \boldsymbol{U}_g$ or in two dimensions

$$\frac{\partial U_g}{\partial x} + \frac{\partial W_g}{\partial z} = 0, \tag{6.6}$$

[9] This depends on the type of electrolyte, electrode, potential, etc. and is, of course, a distribution rather than a single size.

[10] This approximates bubbles as rigid particles, neglecting potential internal fluid circulation. In the presence of surfactants, this is usually a good approximation.

[11] A very rough idea of the bubble release diameter on a horizontal electrode can be obtained from a force balance between the attractive surface tension force and the buoyancy force away from the electrode, see Eq. (6.A.29). However, because this is usually a too strong oversimplification, we only include this analysis for the interested reader in appendix 6.A.

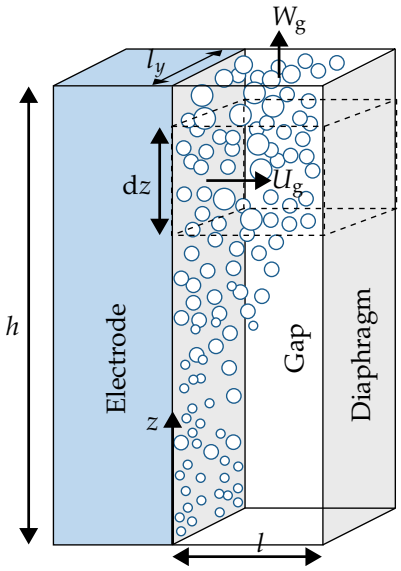

Figure 6.4: *The configuration, dimensions, and velocities used in the analysis of the present section. The gas fraction is averaged over the horizontal direction. The dashed box gives the control volume used in Eq.* (6.8).

where the volumetric gas flux, or superficial gas velocity components in the horizontal x and vertical z-directions, read $U_g = \varepsilon u_g$ and $W_g = \varepsilon w_g$.

As illustrated in Fig. 6.4, for a small enough distance between the electrode and the diaphragm and above a certain height, the gas fraction variation in the horizontal direction may become negligible compared to that in the vertical direction. Here, we will develop a one-dimensional model that can describe the gas fraction as a function of height.

We integrate Eq. (6.6) over the dashed box in Fig. 6.4 from $x = 0$ at the electrode to $x = l$ at the diaphragm and divide by l to give the x-averaged equation[12]

$$\frac{\mathrm{d}W_g}{\mathrm{d}z} = \frac{j\mathcal{V}_m}{nFl}. \tag{6.7}$$

Here, we re-use the symbol $W_g(z) = \frac{1}{l}\int_0^{-l} W_g(x,z)\mathrm{d}x$ for the x-averaged superficial vertical gas velocity, which hopefully does not lead to confusion. The right-hand side gives the volumetric gas flow rate, U_g, at which the gas enters the domain, divided by l. Here $\mathcal{V}_m$ is the molar volume of the gas. For an ideal gas $\mathcal{V}_m = \mathcal{R}T/p$ is equal to 30 l/mol at 85 °C and 1 bar.

[12]In case an additional space of thickness l_b exists behind the electrode, for example in case of a zero-gap or almost zero-gap configuration, we may replace here l with $l + l_b$. In case the bubbles distribute homogeneously horizontally, the analysis will remain the same otherwise.

Assuming $w_s \equiv w_g - w_l = \frac{w_S}{1-\varepsilon}$,[13] we have

$$W_g = \left(W_g + W_l + w_S\right)\varepsilon, \tag{6.8}$$

where $W_l = w_l(1-\varepsilon)$ is the volumetric liquid flux or superficial liquid velocity, so

$$\boxed{\varepsilon = \frac{W_g}{w_S + W_l + W_g/\varepsilon_{max}}.} \tag{6.9}$$

Here $\varepsilon_{max} = 1$, but we will allow different values to be able to describe a maximum gas fraction as $W_g \to \infty$.[14]

Equation (6.9) can be solved for W_g to give

$$W_g = \frac{\varepsilon}{1 - \varepsilon/\varepsilon_{max}}\left(W_l + w_S\right) \tag{6.10}$$

Taking the derivative with respect to z, neglecting the dependence[15] of w_S on z gives, with Eq. (6.7):

$$\frac{\mathrm{d}}{\mathrm{d}z}\left(\frac{\varepsilon}{1-\varepsilon/\varepsilon_{max}}\right) = \frac{\mathrm{d}W_g/\mathrm{d}z}{W_l + w_S}. \tag{6.11}$$

If we know the current distribution j as a function of height or gas fraction, we can solve this equation for the gas fraction. This will be the goal of the next section.

6.4 Vertical gas fraction and current distributions

6.4.1 Constant current density

we take $z = 0$ to be at the bottom of the electrode, and we assume that no gas exists below the electrode. If the current density is constant and we use $W_g(z=0) = 0$, Eq. (6.7) gives $W_g = \frac{\mathrm{d}W_g}{\mathrm{d}z} z$ with $\frac{\mathrm{d}W_g}{\mathrm{d}z}$ given by Eq. (6.7). Inserting this into Eq. (6.9) gives

$$\frac{\varepsilon}{\varepsilon_{max}} = \frac{z}{z_c + z}, \tag{6.12}$$

where, with $j_0 \equiv j(z=0)$:

$$z_c = \varepsilon_{max}\frac{w_S + W_l}{dW_g/\mathrm{d}z\big|_{z=0}} = \varepsilon_{max} l \frac{w_S + W_l}{j_0 \mathcal{V}_m/nF}. \tag{6.13}$$

[13] The lower effective mixture density and 'hindrance' between bubbles reduce the single-bubble rise velocity at higher gas fractions. However, measurements with rising bubbles show that with increasing gas fraction, they mostly speed up due to clustering effects. We model this very crudely by dividing the Stokes rise velocity by $1-\varepsilon$.

[14] The experiments reported in Ref. [7] are described well with $w_S = 0$ and $\varepsilon_{max} = 0.7$, close to the maximum packing fraction of spheres.

[15] By conservation of liquid volume, the superficial liquid velocity W_l does not depend on z.

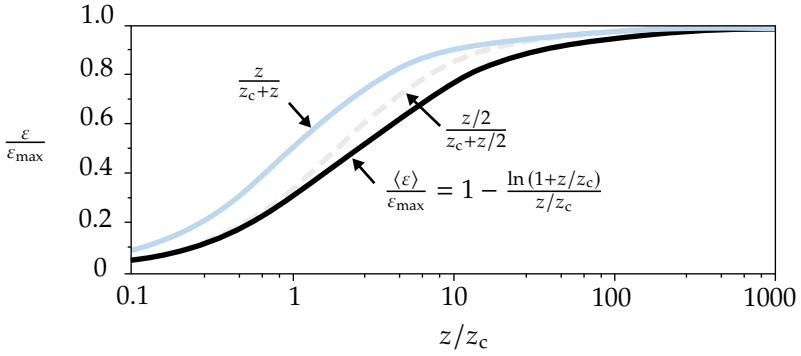

Figure 6.5: *The gas fraction* $\frac{\varepsilon}{\varepsilon_{max}} = \frac{z}{z_c+z}$ *as a function of the dimensionless height* z/z_c *as given by Eq.* (6.12) *(solid blue line) and its running average* $\langle\varepsilon\rangle = \frac{1}{z}\int \varepsilon dz$ *(solid black line) and its approximation as given by Eq.* (6.14).

To derive Eq. (6.12) we considered a constant current density. However, anticipating a variable current density in the next section, we defined z_c in this more general way.

For $z \ll z_c$, Eq. (6.12) gives $\frac{\varepsilon}{\varepsilon_{max}} \approx \frac{z}{z_c}$, from which we see that z_c is a characteristic length-scale associated with the initial increase of the gas fraction with height. In the case of a constant current density, Eq. (6.12) shows that z_c gives the height at which the gas fraction has increased to half its maximum value. A higher current density or lower gap width l increases the volumetric gas flux and thus decreases z_c. The higher the superficial liquid velocity W_l or the bubble slip velocity w_s, the more gas can be transported away, the lower the gas fraction, and the larger z_c will be. When z/z_c is no longer small, the gas fraction will increase sub-linearly and will asymptotically approach its maximum value, see Fig. 6.5.

We are also interested in the average gas fraction $\langle\varepsilon\rangle = \frac{1}{h}\int_0^h \varepsilon dz$, which gives

$$\frac{\langle\varepsilon\rangle}{\varepsilon_{max}} = 1 - \frac{\ln(1+h/z_c)}{h/z_c} \approx \frac{h/2z_c}{1+h/2z_c}. \tag{6.14}$$

In Fig. 6.5, the approximation on the right-hand side is compared with the exact result, showing that this is a reasonably good approximation.[16]

6.4.2 Variable current density

In the traditional cell configuration, on the right of Figure 6.1, and to a much lesser extent also in the zero-gap configuration on the left, bubbles increase the ohmic drop

[16]For $h/z_c \ll 1$, Eq. (6.12) gives $\frac{\varepsilon}{\varepsilon_{max}} = \frac{z}{z_c}$. Taking the first order approximation gives $\langle\varepsilon\rangle = \frac{1}{h}\int_0^h \frac{z}{z_c} dz = h/2z_c$, which is equal to the first order approximation of Eq. (6.14). At higher gas fractions, diving by a higher value than 2, e.g. $\frac{h/3z_c}{1+h/3z_c}$ would give a lower error, but the error would be unacceptably large at lower gas fractions. The relative error compared to the approximation in Eq. (6.14) with the exact result over the entire range of gas fractions is acceptable at less than 12%.

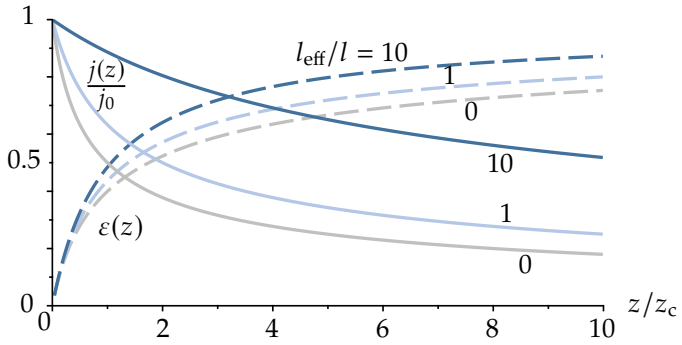

Figure 6.6: *Profiles of the normalized current density j/j_0 (solid) and the gas fraction (dashed) as a function of height z. Various ratios l_{eff}/l, between the non-gap-related cell areal resistance l_{eff}/κ_m, and the bubble-free areal resistance l/κ_m of the gap, are plotted. The higher this ratio, the larger the height over which the current distribution decreases.*

in the electrolyte potential. As bubbles accumulate with height, the impact on the current density will become larger. Here we will try to quantify this effect.

In the original analysis of Charles W. Tobias [29], the gas velocity w_g was taken to be constant, no maximum gas fraction was considered, and no other voltage losses than the ohmic losses in the gap were considered. Here, we make this analysis more realistic by including these additional effects.

From Eq. (6.1) we find the current density to be given by

$$j(z) = \frac{V_{eq} - V_{cell} - \eta}{l/\kappa(z) + l_{eff}/\kappa_m}. \tag{6.15}$$

The presence of bubbles decreases the gap conductivity κ, which decreases the current density. Inserting Eq. (6.15) into Eq. (6.11), using Eq. (6.7), gives

$$\frac{\mathrm{d}}{\mathrm{d}\,(z/z_c)}\left(\frac{\varepsilon/\varepsilon_{max}}{1-\varepsilon/\varepsilon_{max}}\right) = \frac{j(z)}{j_0}. \tag{6.16}$$

We expect this dimensionless current distribution to decrease with height z as the bubble resistance decreases the current. Equation (6.15) gives $\frac{j}{j_0} = \frac{1+l/l_{eff}}{1+l\kappa_m/l_{eff}\kappa}$. Inserting the Maxwell relation Eq. (6.2) we can solve this for ε to give

$$\frac{\varepsilon}{1-\varepsilon} = \frac{2}{3}\frac{j_0 - j}{j}\left(1 + \frac{l_{eff}}{l}\right) \tag{6.17}$$

For $\varepsilon_{max} = 1$ we can insert this into Eq. (6.16) to obtain a separate first-order ordinary differential equation for $j(z)$. Solving it, with as a boundary condition a fixed j_0,

gives

$$\boxed{\frac{j}{j_0} = \frac{1}{\sqrt{1 + \frac{3z/z_c}{1+l_{eff}/l}}}.} \tag{6.18}$$

This relationship gives that the current $j(z) = j_0/2$, so it is halved compared to the current at $z = 0$, for a height given by $z_c\left(1 + \frac{l_{eff}}{l}\right)$, which reduces to z_c in the case of negligible resistance $l_{eff} \ll l$. For a constant current density, this is also the height at which the gas fraction reaches half its maximum. Any additional resistance in the diaphragm will cause the current density to halve at a larger height. This is also clearly visible from the graphical depiction in Fig. 6.6.

Inserting Eq. (6.18) into Eq. (6.17) gives the gas fraction profile as a function of height.[17] This exact solution is shown as the dashed lines in Fig. 6.6 and gives a result very similar to $\frac{z}{z+z_c}$ of Eq. (6.12), with a maximum relative error below 22 %. Therefore, at least for ε_{max}, this simpler relation can be used to obtain a rough indication of the gas fraction profile.[18]

6.5 Natural liquid circulation

High gas fractions can lead to dry zones, called *hot-spots*, that can become dangerously hot. To avoid this, Eq. (6.12) shows that z_c should be sufficiently high compared to the electrolyser height. According to Eq. (6.13) this characteristic height increases with increasing l. Therefore, scaling up the electrolyser height also requires more horizontal space for the gas. Alternatively, Eq. (6.13) shows that z_c also increases with increasing superficial liquid velocity W_l. Using electrolyte convection can, therefore, help to remove the gas more effectively and allow for more compact electrolysers. Additionally, liquid flow also helps transport heat out of the cells.

The use of a pump adds additional costs for power use and maintenance. Therefore, some atmospheric pressure electrolysers use the buoyancy of the rising bubbles to set the electrolyte into motion. Fig. 6.7 illustrates the operational principle behind a natural recirculation electrolyser. The rising bubbles drag liquid flow upwards in what we will call the '*riser*'. This is the bubble-filled space between the diaphragm and the electrode or behind the electrode in case of a zero-gap electrolyser. After the bubbles are removed in a *gas-liquid separator*, the bubble-free electrolyte flows downwards through a '*downcomer*' and re-enters the bottom of the electrolyser.

Due to the presence of the bubbles, the liquid column near the electrode will be lighter than that of the bubble-free downcomer. The hydrostatic pressure in the

[17] Alternatively, in Appendix 6.B we solve Eqs. (6.16) and (6.15) directly for the gas fraction. The result is the same and provided in Eq. (6.B.33).

[18] We note from Eq. (6.18) that the highest height-average current density is obtained when $l = 0$. Therefore, to maximise the total current, the gap l should be made as small as practically possible. This is indeed what most of the data of Ref. [19] shows. However, for some of the higher current densities, an optimum gap l is observed that is not predicted by our model. This may indicate, for example, the transition to a slug flow regime or some other effect not incorporated here.

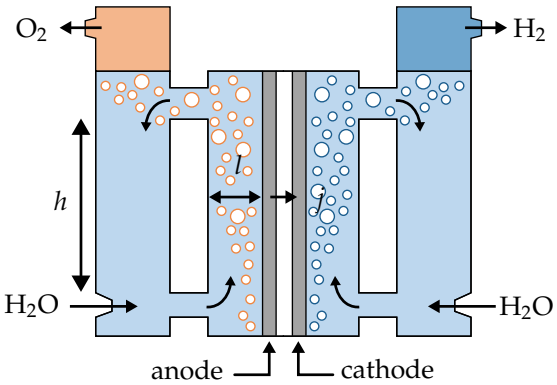

Figure 6.7: *An illustration of the natural liquid recirculation that will arise due to the buoyancy of the gas evolving from the electrodes. When there is a closed loop where liquid can recirculate in a* downcomer*, the difference in weight of the liquid with and without bubbles will drive a natural circulation pattern.*

downcomer is $\rho_l g h$, while that in the riser is $\rho_l (1 - \langle \varepsilon \rangle) g h$, where $\rho_l (1 - \langle \varepsilon \rangle)$ is the average mixture density in the riser. The pressure difference $\rho_l g h \langle \varepsilon \rangle$ between the riser and downcomer will create an upward flow in the riser, which will induce a frictional pressure drop Δp_f. In a steady-state, the resulting pressure balance reads

$$\rho_l g h \langle \varepsilon \rangle = \Delta p_f. \tag{6.19}$$

We will write this frictional pressure drop as

$$\Delta p_f \approx \frac{1}{2} \rho W_l^2 K, \tag{6.20}$$

where we can add $K = \sum_i K_i$ the contributions of various *irreversible loss coefficients* due to bends ($K \approx 1$) and contractions ($K \approx 1.5$) to the frictional contribution of the riser[19]

$$K_{\text{riser}} = f \frac{h}{l}. \tag{6.21}$$

For turbulent single-phase flow the coefficients K and the *friction factor*[20] f depend only weakly on the liquid velocity W_l. Using these same values for multi-phase flow will only be a crude approximation. In general, they will also depend on the gas fraction and/or the gas velocity W_g.

[19] In case the flow area A_i of segment i differs from the flow area $A_\perp$ of the riser, we may write $K = \sum_i \left(\frac{A_\perp}{A_i}\right)^2 \left(K_i + f_i \frac{h_i}{d_i}\right)$. The hydraulic diameter $d_i = 4A_i/P_i$ with P_i the perimeter and area of segment i. For a circular cross-section, this is the diameter, while for two parallel plates, it is the distance l_i between them. The prefactor $\left(\frac{A_i}{A_\perp}\right)^2$ corrects the local velocity to $W_i = \left(\frac{A_\perp}{A_i}\right)^2 W_l$.

[20] This is the Darcy friction factor, which is four times the Fanning fraction factor. Inserting Eq. (6.21) into Eq. (6.20) gives the Darcy-Weisbach equation.

The maximum liquid velocity $W_{l,max}$ arises when the average gas fraction in the riser is equal to the maximum $\langle\varepsilon\rangle = \varepsilon_{max}$. In this case, Eqs. (6.19) and (6.21) combine to give

$$W_{l,max} = \sqrt{\frac{2gh\varepsilon_{max}}{K}}. \tag{6.22}$$

Note that $\sqrt{2gh}$ is the maximum velocity that a free-falling object[21] attains when dropped from a height h.

To make further analytical progress, assume a constant current density and use the approximation in Eq. (6.14). Together with Eq. (6.13), this reads

$$\frac{\langle\varepsilon\rangle}{\varepsilon_{max}} \approx \frac{W_g/2\varepsilon_{max}}{w_S + W_l + W_g/2\varepsilon_{max}} \tag{6.23}$$

where

$$W_g = \frac{h}{l}\frac{j\mathcal{V}_m}{nF}, \tag{6.24}$$

is the superficial gas flux at the top of the electrolyser at $z = h$.[22]

From Eqs. (6.19) and (6.20) the superficial liquid velocity squared, W_l^2, is proportional to the average gas fraction $\langle\varepsilon\rangle$. Therefore, Eq. (6.23) gives

$$W_l^2 \approx \frac{2gh\varepsilon_{max}/K}{1 + 2\varepsilon_{max}\frac{w_S+W_l}{W_g}}. \tag{6.25}$$

Here the numerator is the squared maximum superficial liquid velocity of Eq. (6.22), which is obtained in case the superficial gas velocity W_g far exceeds $w_S + W_l$. The denominator brings down this maximum velocity when the average fraction in the riser is not equal to the maximum. This depends on the ratio between the sum of the upwards velocities $w_S + W_l$ and the superficial gas velocity W_g.

For K independent of W_l, Eq. (6.25) is a cubic equation for W_l that can be solved analytically. However, this gives a somewhat lengthy expression and a good approximation is provided in Eq. (6.C.37). Here, we consider only its limits. Neglecting the Stokes slip velocity[23], the limits of relatively high and low superficial gas velocity

[21] This is called Toricelli's law. Equation (6.22) reminds us of the terminal velocity of an object in the presence of a drag force, with K appearing instead of a drag coefficient. The ratio $\mathrm{Fr} \equiv W_l/\sqrt{2gh}$ is referred to as the Froude number, which according to Eq. (6.22) will satisfy $\mathrm{Fr} \leq \sqrt{\varepsilon_{max}/K}$.

[22] Obtained by integrating Eq. (6.7) from $z = 0$ to $z = h$.

[23] The cases of dominant superficial gas velocity and liquid velocity are shown in Eq. (6.26). Assuming the opposite limit of dominant slip velocity $w_S \gg \left(W_{l,max}^2 \frac{W_g}{2\varepsilon_{max}}\right)^{1/3}$, $\frac{W_g}{2\varepsilon_{max}}$ gives $W_l \approx \sqrt{\frac{W_{l,max}^2}{w_S}\frac{W_g}{2\varepsilon_{max}}} = \sqrt{\frac{W_g}{w_S}\frac{gh}{K}}$. Depending on the relative magnitude of W_g, $W_{l,max}$ and w_S, the liquid velocity can scale with the square root of the current density, the cubic root, or not at all.

read, respectively

$$W_\mathrm{l} \approx \begin{cases} W_\mathrm{l,max} & \text{for } W_\mathrm{l,max} \ll \frac{W_\mathrm{g}}{2\varepsilon_\mathrm{max}}, \\ \left(W_\mathrm{g}\frac{gh}{K}\right)^{1/3} & \text{for } W_\mathrm{l,max} \gg \frac{W_\mathrm{g}}{2\varepsilon_\mathrm{max}}. \end{cases} \tag{6.26}$$

The top limit in Eq. (6.26) is obtained for relatively high superficial gas fluxes W_g, so the maximum gas fraction is obtained. The lower limit in Eq. (6.26) is obtained for relatively low superficial gas fluxes W_g,[24] requiring, according to Eq. (6.24), relatively low current densities j, heights h, and/or relatively large gaps l. In this regime, the superficial liquid velocity increases proportional to $\left(jh^2/Kl\right)^{1/3}$.

For a typical atmospheric pressure electrolyser we take $\mathcal{V}_\mathrm{m} = 0.06\ \mathrm{m^3/mol}$,[25], a height $h = 1$ m, a gap of $l = 1$ cm, and $j = 1\ \mathrm{A/cm^2}$. Inserting into Eq. (6.24) gives $W_\mathrm{g} \approx 0.3$ m/s for the hydrogen side ($n = 2$). Usually, the inlets and outlets of cells have areas that are much smaller than the riser flow area,[26] which can lead to very large values of K, see footnote 19. For example, a reduction in flow area by a factor 10^2 gives $K \approx 10^4$, for which the top limit of Eq. (6.26) gives $W_\mathrm{l} \approx 4$ cm/s. This is more than sufficient to remove the heat and gas from the cell. However, in larger stacks or at higher pressure, the limited recirculation velocity may require the use of a pump.

6.6 Summary

- For a maximum gas fraction $\varepsilon_\mathrm{max} = 1$, the gas fraction inside the electrolyser $\varepsilon = \frac{W_\mathrm{g}}{w_\mathrm{S}+W_\mathrm{l}+W_\mathrm{g}} = \frac{z}{z_\mathrm{c}+z}$ (6.9), (6.12) increases to 1/2 at a height $z_\mathrm{c} = l\frac{w_\mathrm{S}+W_\mathrm{l}}{j_0\mathcal{V}_\mathrm{m}/nF}$ (6.13). A relatively high superficial liquid velocity W_l or Stokes rise velocity w_S can increase this height, while a higher current density and a smaller gap thickness l decrease it.

- In a traditional electrolyser design where the bubbles rise in the inter-electrode spacing, the current will decrease with height according to $\frac{j}{j_0} = \frac{1}{\sqrt{1+\frac{3z/z_\mathrm{c}}{1+l_\mathrm{eff}/l}}}$. For higher areal resistance $l_\mathrm{eff}/\kappa_\mathrm{m}$ relative to that of the gap l/κ_m, the height at which the current density halves, increases.

- In a natural recirculation electrolyser the pressure difference between riser and downcomer is compensated by friction: $\langle\varepsilon\rangle\rho_\mathrm{l}gh = \Delta p_\mathrm{f}$. Considering only turbulent friction $\Delta p_\mathrm{f} \approx \frac{1}{2}\rho W_\mathrm{l}^2 K$ (6.20) gives $W_\mathrm{l,max} = \sqrt{\frac{2gh\varepsilon_\mathrm{max}}{K}}$ (6.22) in case the maximum gas fraction is reached in the riser.

[24] The friction in the downcomer circuit, as quantified by K, should also be small enough to allow the slip velocity to be neglected with respect to the superficial liquid velocity.

[25] With $T = 80°$ C and $p = 10^5$ Pa, the ideal gas law gives $\mathcal{V}_\mathrm{m} \approx 0.03\ \mathrm{m^3/mol}$, but at such temperatures the gas bubbles will also contain significant amounts of water vapour, easily doubling the gas volume.

[26] In a bipolar stack this is required to avoid 'shunt currents' that arise when ions skip a number of cells by travelling out of their cell.

Exercise 6.1

a. High gas fractions can give rise to hot spots. When problems arise near the cathode of a water electrolyser when $\varepsilon = \varepsilon_c < \varepsilon_{max}$, give an expression for the maximum electrolyser height to stay below this gas fraction You may assume a constant current density and a half-cell width l.

b. With $j = 1$ A/cm^2, $\varepsilon_{max} = 0.9$, $\varepsilon_{max} = 1$, $l = 1$ cm, and $w_S + W_l = 1$ cm/s, give a numerical value for this maximum electrolyser height at ambient conditions.

Exercise 6.2

Consider a half-cell of a traditional electrolyser configuration with a gap of thickness l, an electrolyte conductivity κ_m and an approximately constant current density j.

a. Assuming the tortuosity squared (τ^2) of the ion path around the bubbles with a gas fraction ε is given by $\frac{1}{1-\varepsilon}$, give an expression for the local ohmic voltage drop over the gap.

b. When $\varepsilon \approx z/z_c \ll 1$, give an expression for the height-averaged ohmic drop at a height h to first order in $h/z_c \ll 1$.

c. Give an expression for only the *additional* dissipated ohmic power [J/s] as a consequence of the presence of bubbles for an electrode of area A.

d. Assuming $\varepsilon_{max} = 1$ and neglecting w_S, Eq. (6.13) gives $z_c = \frac{lW_l}{j\mathcal{V}_m/nF}$. Increasing the liquid velocity W_l thus increases z_c and decreases the bubble-associated ohmic dissipation. However, this goes at the expense of additional pumping power $Q\Delta p$, with $Q = W_l Al/h$ the volumetric flow rate. Assume that the Hagen-Poiseuille equation $\Delta p = 12\mu W_l/l^2$ holds and that Stokes slip is negligible. Give an expression for the optimal superficial liquid velocity W_l that minimises the total dissipation.

e. With $j = 0.3$ A/cm^2, $h = 1$ m, $l = 1$ cm, $\kappa_m = 100$ S/m, and $\mu = 1$ mPas, give this optimal velocity for the hydrogen side at ambient conditions.

Exercise 6.3

In the main text, we assumed that the gas fraction depends only on height z, while it may also depend on a horizontal coordinate x across the cell. Here we consider the simplest way to model this for a zero-gap electrolyser.

a. If the (constant) current is j, the number of electrons per gas molecule n, the gas molar volume $\mathcal{V}_m$, and Faraday's constant F, what is the superficial gas velocity emanating from the electrode in the x-direction?

We assume that :

- at $z = 0$ there is no gas,
- the average interstitial gas velocity is a constant w_g,
- the gas fraction is a constant ε between the electrode at $x = 0$ and $x = \delta$,
- the gas fraction is zero between $x = \delta$ and the back wall at $x = l$.

b. Using conservation of gas volume, give an expression for the bubble plume thickness δ.

c. Assuming $w_g = 0.3$ m/s, $\varepsilon = 0.2$, $j = 0.2$ A/cm^2, $\mathcal{V}_m = 25$ l/mol, and $n = 2$, what will be the plume thickness at a height of $z = 1$ m?

Exercise 6.4

A perforated plate electrode used in gas-evolving electrolysers may be treated as a porous medium with a tortuosity equal to 1. Its front and back areas do not participate in the reaction; only the electrode area inside the perforations does.

a. If the holes make up a fraction ϵ of the electrode area, and these holes contain a gas fraction ε, what is the ohmic drop if a current density j, as always per total unit area, traverses the full thickness L of the electrodes when the electrolyte conductivity is κ?

b. With b the Tafel slope of the electrode, what is the Thiele modulus M associated with this ohmic limitation?

c. If M $\gg$ 1, by what number is the effectiveness factor multiplied when the gas fraction increases from 0.3 to 0.6?

d. Give a formula for the overpotential that can be attributed to the presence of bubbles.

Exercises 6.5-6.17

Fill in the missing steps in the main text, indicated by the symbol  .

*Appendices **

6.A *Bubble release diameter*

As we saw in section 6.3, the gas fraction ε is determined by how much gas is produced and how fast it can be removed. This can occur through the flow of electrolytes but also due to the velocity of the bubbles relative to the liquid. To determine this buoyant rise velocity, as discussed in section 6.2.2, we have to know their size. The size distribution of bubbles is very hard to model due to the complex interactions between bubbles, the bubbles and the electrode, and the electrolyte flow. In the context of describing boiling, some limited success has been obtained by considering the force balance. Such types of analysis are complicated because the exact shape of the bubble at the point of its release must be known to evaluate all the forces accurately. This can be solved exactly in the special case of single bubbles in a quiescent liquid on a horizontal surface. Since this can give us an idea of typical bubble sizes, we will consider this force balance here.

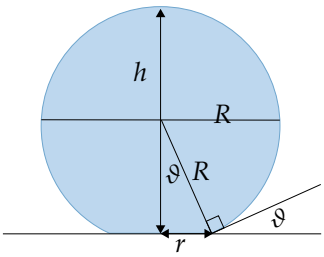

Figure 6.8: *A* spherical cap *bubble on a horizontal surface, showing the contact angle* ϑ.

Consider the approximately *spherical cap* bubble of Fig. 6.8. The surface tension force keeping the bubble attached to the surface despite its buoyancy is given by γ times $\sin\vartheta$, times the perimeter of the contact line.[27] By solving for the exact shape of the bubble, it can be shown that at the point of release 3/4 of this force will

[27]The surface tension potential energy reads $\mathcal{U} = \gamma\pi r^2$ so that the principle of virtual work gives the force associated with a change in the bubble radius as $\partial\mathcal{U}/\partial R = \sin\vartheta\partial\mathcal{U}/\partial r = 2\pi r\sin\vartheta\gamma$.

be cancelled by the additional Laplace pressure inside the bubble[28] so that the net attractive force reads

$$F_{\downarrow} = \frac{\pi R}{2}\gamma \sin^2 \vartheta. \tag{6.A.27}$$

The main force away from the surface, $F_{\uparrow}$, is that due to buoyancy. We will consider the contact angle to be small, $\vartheta \ll \pi/2$, and approximate the volume of the bubble by that of a sphere so that, neglecting the gas density,

$$F_{\uparrow} = \frac{4\rho g}{3}\pi R^3. \tag{6.A.28}$$

Equating these forces gives for the bubble release radius R

$$R = \vartheta\sqrt{\frac{3\gamma}{8\rho g}}. \tag{6.A.29}$$

This is called the Fritz equation, where we note that ϑ is in radians and is assumed to be small compared to $\pi/2$.[29] Using $\gamma = 73$ mN/m and $\rho = 10^3$, typical for aqueous electrolytes, and $\vartheta = 20° \frac{\pi}{180}$, typical for smooth pure metal surfaces, this gives a release diameter $2R = 120$ µm. Interactions with other bubbles and flow will usually tend to decrease this release radius further. Especially hydrogen bubbles in alkaline electrolytes can be much smaller still.

6.B *Dimensionless current distribution*

We introduce the dimensionless current density profile $\bar{j} = j/j_0$, where $j_0 = \frac{V_{\mathrm{eq}} - V_{\mathrm{cell}} - \eta}{l/\kappa + l_{\mathrm{eff}}/\kappa_{\mathrm{m}}}$. In dimensionless notation, Eq. (6.15) can be written as

$$\bar{j} = \frac{1 + \bar{R}}{1/\bar{\kappa} + \bar{R}}, \tag{6.B.30}$$

where $\bar{R} = l_{\mathrm{eff}}/l$ is the diaphragm resistance relative to the bubble-free gap resistance. Inserting Eq. (6.B.30) in Eq. (6.11) gives, assuming $\varepsilon_{\max} = 1$,

$$\frac{\mathrm{d}}{\mathrm{d}\bar{z}}\left(\frac{\varepsilon}{1-\varepsilon}\right) = \frac{1 + \bar{R}}{1/\bar{\kappa}(\varepsilon) + \bar{R}}. \tag{6.B.31}$$

[28] The Laplace pressure is given by Eq. (5.4) as $p_{\mathrm{l}} = 2\gamma/R$ so that multiplying with the contact area $\pi r^2 = \pi R^2 \sin^2\vartheta$ gives a repulsive force $2\pi\gamma R \sin^2\vartheta$, equal and opposite to the surface tension force. However, buoyancy will slightly lift the bubble, changing its shape, so one can show that the cancellation is incomplete.

[29] For small contact angles we have $\sin\vartheta \approx \vartheta$. Using degrees instead of radians sometimes $2R = 0.021\vartheta\sqrt{\frac{\gamma}{g\rho}}$ can also be found in the literature [25].

where $\bar{z} \equiv z/z_c$. We can solve Eq. (6.B.31) using the Maxwell relation (6.2),[30] to give

$$\varepsilon\left(\bar{z}\right) = \frac{1}{1 + \frac{3}{2\left(1+\bar{R}\right)\left(\sqrt{1+\frac{3\bar{z}}{1+\bar{R}}}-1\right)}} \approx \begin{cases} \frac{\sqrt{1+3\bar{z}}-1}{\sqrt{1+3\bar{z}}+\frac{1}{2}} & \bar{R} = 0, \\ \frac{\bar{z}}{1+\bar{z}} & \bar{R} \to \infty. \end{cases} \tag{6.B.32}$$

For $\bar{z} \ll 1$ the solution approximates to $\varepsilon \approx \bar{z} \ll 1$, independent of $\bar{R}$. This is equal to the previous result of Eq. (6.12) for constant current density. In dimensional notation, Eq. (6.B.32) reads

$$\varepsilon\left(z/z_c\right) = \frac{1}{1 + \frac{3}{2(1+l_{\text{eff}}/l)\left(\sqrt{1+\frac{3z/z_c}{1+l_{\text{eff}}/l}}-1\right)}} \approx \begin{cases} \frac{\sqrt{1+3z/z_c}-1}{\sqrt{1+3z/z_c}+\frac{1}{2}} & l_{\text{eff}} = 0, \\ \frac{z}{z_c+z} & l_{\text{eff}} \to \infty. \end{cases} \tag{6.B.33}$$

In the limit $l_{\text{eff}} \to \infty$, the resistance of the gap can be neglected so the current density will be independent of the gas fraction in the gap, and we retain the previous result of Eq. (6.12) for constant current density.

Inserting the solution of Eq. (6.B.33) into Eq. (6.B.30) gives Eq. (6.18), or in dimensionless form

$$\bar{j} = \frac{1}{\sqrt{1 + \frac{3\bar{z}}{1+\bar{R}}}}. \tag{6.B.34}$$

In the limit $\bar{z} \gg 1 + \bar{R}$, this tends to zero.

6.C *An expression for the liquid recirculation velocity*

In terms of $W_{l,\max}$ defined in Eq. (6.22) we can approximate the solution to Eq. (6.25) by

$$W_l \approx \frac{\left(W_g W_{l,\max}^2/2\varepsilon_{\max}\right)^{1/3}}{\left(1 + \left(\frac{w_S + W_g/2\varepsilon_{\max}}{\left(W_g W_{l,\max}^2/2\varepsilon_{\max}\right)^{1/3}}\right)^{p/2}\right)^{1/p}} \approx \begin{cases} \frac{W_{l,\max}}{\sqrt{1+2\varepsilon_{\max} w_S/W_g}} & \ll w_S \text{ or } \frac{W_g}{2\varepsilon_{\max}}, \\ \left(\frac{W_g W_{l,\max}^2}{2\varepsilon_{\max}}\right)^{1/3} & \gg w_S \text{ and } \frac{W_g}{2\varepsilon_{\max}}. \end{cases} \tag{6.C.35}$$

This is nearly identical to the exact result using $p \approx 2.6$. For $p = 3$ and inserting Eqs. (6.24) and (6.22):

[30] The resulting differential equation $\frac{1}{1+\bar{R}}\left(\frac{1+\varepsilon/2}{1-\varepsilon} + \bar{R}\right)\frac{\mathrm{d}}{\mathrm{d}\bar{z}}\left(\frac{\varepsilon}{1-\varepsilon}\right) = 1$, with the substitutions $\tilde{\varepsilon} = \frac{\varepsilon}{1-\varepsilon}$ and $\frac{1}{\kappa} = \frac{1+\varepsilon/2}{1-\varepsilon} = 1 + \frac{3}{2}\tilde{\varepsilon}$, reads $\frac{1+3\tilde{\varepsilon}/2+\bar{R}}{1+\bar{R}}\frac{\mathrm{d}\tilde{\varepsilon}}{\mathrm{d}\bar{z}} = 1$, so that, with the boundary condition $\varepsilon(0) = 0$, we find $\int_0^{\tilde{\varepsilon}}\left[1 + \frac{3\tilde{\varepsilon}}{2(1+\bar{R})}\right]d\tilde{\varepsilon} = \tilde{\varepsilon} + \frac{3\tilde{\varepsilon}^2}{4(1+\bar{R})} = \bar{z}$. This quadratic equation is solved by $\tilde{\varepsilon} = \frac{2(1+\bar{R})}{3}\left(\sqrt{1+\frac{3\bar{z}}{1+\bar{R}}} - 1\right)$ or $\varepsilon = \frac{\tilde{\varepsilon}}{1+\tilde{\varepsilon}}$ given by Eq. (6.B.32).

$$W_\mathrm{l} \approx \frac{(gh/K)^{\frac{1}{3}}}{\left(\frac{1}{W_\mathrm{g}} + \left(\frac{w_\mathrm{S}/W_\mathrm{g}+1/2\varepsilon_\mathrm{max}}{(gh/K)^{\frac{1}{3}}}\right)^{\frac{3}{2}}\right)^{\frac{1}{3}}} \approx \begin{cases} \sqrt{\frac{2gh\varepsilon_\mathrm{max}/K}{1+\frac{2\varepsilon_\mathrm{max}w_\mathrm{S}l}{h}\frac{nF}{j\mathcal{V}_\mathrm{m}}}} & \ll w_\mathrm{S} \text{ or } \frac{W_\mathrm{g}}{2\varepsilon_\mathrm{max}}, \\ \left(\frac{j\mathcal{V}_\mathrm{m}}{nF}\frac{gh^2}{Kl}\right)^{1/3} & \gg w_\mathrm{S} \text{ and } \frac{W_\mathrm{g}}{2\varepsilon_\mathrm{max}}. \end{cases} \tag{6.C.36}$$

The limits of high gas velocity, high slip velocity, and high liquid velocity can be written, respectively as:

$$W_\mathrm{l} \approx \begin{cases} W_\mathrm{l,max} & W_\mathrm{l,max}, w_\mathrm{S} \ll \frac{W_\mathrm{g}}{2\varepsilon_\mathrm{max}}, \\ \sqrt{\frac{W_\mathrm{l,max}^2}{w_\mathrm{S}}\frac{W_\mathrm{g}}{2\varepsilon_\mathrm{max}}} & \left(W_\mathrm{l,max}^2\frac{W_\mathrm{g}}{2\varepsilon_\mathrm{max}}\right)^{1/3}, \frac{W_\mathrm{g}}{2\varepsilon_\mathrm{max}} \ll w_\mathrm{S}, \\ \left(W_\mathrm{l,max}^2\frac{W_\mathrm{g}}{2\varepsilon_\mathrm{max}}\right)^{1/3} & \frac{w_\mathrm{S}^3}{W_\mathrm{l,max}^2} \ll \frac{W_\mathrm{g}}{2\varepsilon_\mathrm{max}} \ll \frac{W_\mathrm{l,max}}{2\varepsilon_\mathrm{max}}. \end{cases} \tag{6.C.37}$$

Chapter 7

Redox Flow Batteries

Redox flow batteries are reversible fuel cells or integrated fuel cell-electrolyser combinations. They typically use liquid electrolyte flow, normal to the current density. Properly describing the mass transport parallel to the current, coupled to the current distribution parallel to the flow, inherently requires two-dimensional models. We will take a decoupled approach where we consider these directions independently. The resulting models will also be useful for describing fuel cells.

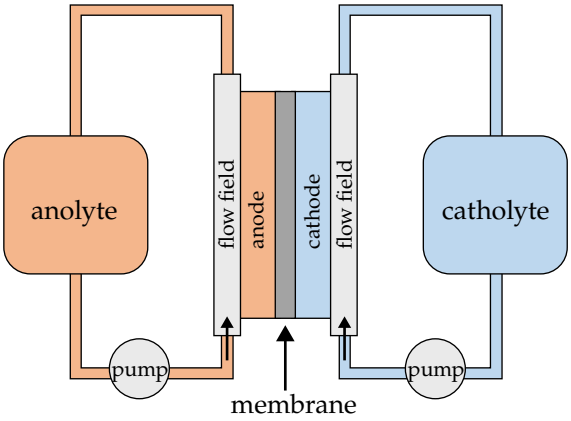

Figure 7.1: *A schematic of a generic redox flow battery where the reactants, oxidant and reductant, are stored in separate tanks and pumped into the cell that can be operated both galvanically and electrolytically.*

7.1 Introduction

Redox flow batteries are essentially fuel cells and electrolysers made into one device. They use redox couples that are reversible enough so that, with low activation overpotentials, they can be both oxidised and reduced. The most commonly used reaction is with Vanadium due to its stability, relatively low toxicity, and ability to be used to both anode and cathode, minimising problems with crossover. However, its high cost, low energy, and power density leave room for the development of different types of flow batteries.

The two redox couples, with or without additional supporting electrolytes, are usually stored in two separate tanks, see Fig. 7.1. A pump supplies them to the cell at the desired rate. Most often, redox flow batteries work with aqueous solutions, although sometimes non-aqueous solvents, gases, or even suspended solid particles are used. See section 7.2 for a classification of the various types of flow batteries.

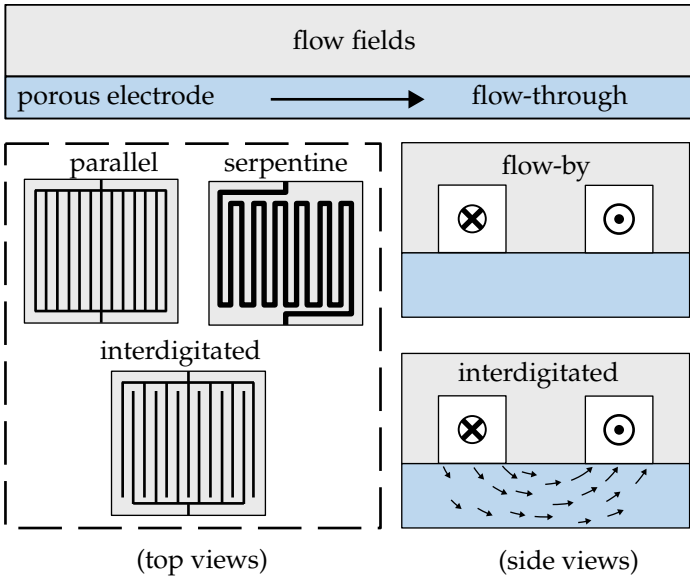

Figure 7.2: *The three main flow modes of redox flow batteries are flow-through (top), flow-by (middle), and interdigitated (bottom). In flow-through cells, there is no flow field, and the electrolyte flows through the porous electrode. In a flow-by configuration, there is little to no flow inside the electrodes, and reactants diffuse in. A serpentine flow field may be used to increase the flow path length. Interdigitated designs combine the advantages of both flow-through and flow-by properties.*

A potential advantage compared to batteries is that the reactants in flow batteries can flow and, therefore, can be conveniently stored in a tank outside of the electrochemical cell. This decoupling of the power, determined by the cell design, and the storage capacity, determined by the external tanks, gives additional design

freedom. It makes redox flow batteries suitable for storing energy for the day-night cycle variations in electricity supply and demand.

Inside the cell, the reactants are sometimes pumped directly through a porous electrode, in what is called a *flow-through* configuration, shown in Fig. 7.2.[1] The small pores in the carbon paper, mesh, or cloth electrode can cause large pressure drops. Therefore, the middle row of Fig. 7.2 shows the *flow-by* alternative, in which the flow passes by the electrode through channels engraved in the current collector/bipolar plate. In this case, the flow inside the electrode will be very small, and reactants primarily diffuse towards their reaction sites. If additional channel length is desired, for example, to ensure that a large fraction of the reactants is converted, a *serpentine flow field* forms a suitable alternative to a *parallel flow field*.

A third option, shown at the bottom of Fig. 7.2, is an interdigitated configuration. Here, the inlet and outlet channels are not connected, so the electrolyte has to flow through the electrode to reach the outlet. This gives the same advantage of advective mass transport as in a flow-through configuration but with much smaller pressure drops since the distance over which the fluid travels is much smaller.

7.2 *Types of redox flow batteries **

While most commercial systems are based on Vanadium, research on many other chemistries and cell designs exists. While there may be overlap and combinations possible, we can distinguish the following broad classification of flow battery types.

- Traditional: this comprises the most common Vanadium-based redox flow batteries, such as the all-Vanadium type, see Tbl. 7.1, but also, for example, the Vanadium-Bromine alternative. Vanadium-Oxygen redox flow batteries have the advantage that air can be used, which does not have to be stored. Also in this category is the unitised regenerative fuel cell, a H_2/O_2 fuel cell and water electrolyser combined in the same device. When one of the reactants is gaseous, for example in the H_2/Br_2 flow battery, a gas-breathing electrode is used.

- Hybrid: sometimes, a flow battery half-cell is combined with a normal battery half-cell. Most commonly, Zinc is used for the battery electrode. Halogens like Bromine or Iodine are often used for the flow battery electrode. The energy density of a Zinc-air battery could potentially be similar to that of Li-ion batteries. Making this type of battery rechargeable has proven to be challenging.

- Organic: potentially more eco-friendly and versatile, organic redox couples are intensively researched. Most types depend on quinones, which have a benzene ring with an even number of C-H-bonds changed to C=O double bonds.

[1] In this case, the flow is normal to the current density. Traditionally, the term flow-through electrode was also used to describe a flow parallel to the current. Contrary to modern flow-battery parlance, which we will follow here, the term flow-by was sometimes used to refer to flow through a porous electrode normal to the current density, which is now called flow-through.

- Semi-solid: To combine battery chemistries with the scalability and storage advantages of flow batteries, solid battery particles may be put into suspension. This allows pumping the battery particles in a suspension-based flow battery.
- Membraneless/microfluidic: Since liquids have relatively low diffusion coefficients, their laminar concentration boundary layers are relatively thin. In case of two reactants, by placing the one with the highest density below the one with a lower density a stably stratified laminar flow can be created. In case the reactants are miscible in each other, a diffusion boundary layer arises that can be kept thin with sufficient flow, as schematically illustrated at the top of Fig. 7.3. The bottom part of this figure shows a case of effective product separation. Membraneless cells H_2/Br_2 cells have shown high power densities, nearing 1 W/cm^2.[26].

Name	Anode	Cathode
all-Vanadium	$VO^{2+} + H_2O \longleftrightarrow VO_2{}^+ + 2\,H^+ + e^-$	$V^{2+} + e^- \longleftrightarrow V^{2+}$
Zinc/Bromine hybrid	$2\,Br^- \longleftrightarrow Br_2 + 2\,e^-$	$Zn^{2+} + 2\,e^- \longleftrightarrow Zn$
Iron/Chromium	$Fe^{2+} \longleftrightarrow Fe^{3+} + e^-$	$Cr^{3+} + e^- \longleftrightarrow Cr^{2+}$
Hydrogen/Bromine	$2\,Br^- \longleftrightarrow Br_2 + 2\,e^-$	$2\,H^+ + 2\,e^- \longleftrightarrow H_2$

Table 7.1: *An arbitrary selection of some of the more commonly investigated chemistries for redox flow batteries.*

7.3 Flow-through electrodes

As shown in Fig. 7.2, in the flow-through electrode configuration, there is no separate flow channel, and the flow goes entirely through the electrodes. This is typically used to improve the rate of mass transfer. The length scale over which reactants have to diffuse is reduced to a fraction of a pore size so that the limiting current density can be relatively high.

As discussed in the introduction and shown in Fig. 7.2, an alternative with lower pressure drops is the interdigitated design. The analysis given below will approximately hold in this case when the channel length h is replaced by some characteristic distance relevant for the flow, of the order of the distance between interdigitated channels [5].

As argued in section 7.5.1, diffusive transport in the flow direction can usually be neglected relative to advective transport. For a superficial velocity W in the z-direction, Eqs. (3.15), (3.16) and (3.18) in steady-state combine to give

$$W\frac{\mathrm{d}c}{\mathrm{d}z} = \frac{aj_\perp}{nF}. \tag{7.1}$$

Here, we assume that the concentration $c(z)$ will only be a function of the flow direction z.[2] For an anode, inserting the concentration-dependent Tafel equation (1.28) $j_\perp = j_* \frac{c}{c_{\text{in}}} \mathrm{e}^{\eta/b}$, Eq. (7.1) gives

$$W \frac{\mathrm{d}c}{\mathrm{d}z} = -kac \quad \text{where } k = \frac{j_* \mathrm{e}^{\eta/b}}{nFc_{\text{in}}}. \tag{7.2}$$

For a constant reaction rate coefficient $k = j_\perp / nFc$, the solution of Eq. (7.2) with boundary condition $c(0) = c_{\text{in}}$ reads

$$\boxed{c(z) = c_{\text{in}} \mathrm{e}^{-\frac{ka}{W} z}.} \tag{7.3}$$

So, the reactant concentration decreases exponentially in the flow, as is expected from a reaction rate that is proportional to the concentration.[3]

Integrating Eq. (7.1) over x over the electrode thickness L gives

$$WL \frac{\mathrm{d}c}{\mathrm{d}z} = \frac{j}{nF} \tag{7.4}$$

where $j = aLj_\perp$, using the conversion factor aL introduced in Eq. (3.35). It is solved by

$$c(z) = c_{\text{in}} - \frac{\int_0^z j \mathrm{d}z}{nFWL}. \tag{7.5}$$

For a constant current density j, this gives the linearly decreasing profile $c(z) = c_{\text{in}} - \frac{j}{nFWL} z$. In general, the concentration will lie somewhere in between this linearly decreasing profile and the exponential decrease of Eq. (7.5).

We define the (degree of) conversion as the fraction of inlet concentration that is converted at the exit:

$$X \equiv \frac{c_{\text{in}} - c_{\text{m}}^{\text{out}}}{c_{\text{in}}} = 1 - \mathrm{e}^{-\frac{ka}{W} h}, \tag{7.6}$$

where we evaluated Eq. (7.22) at the outlet using $\langle \mathrm{S} \rangle_{\text{out}} = \langle \mathrm{S} \rangle (z = h)$. The longer the channel length h, or the lower the flow velocity $\langle w \rangle$, the more material converts. Also, the lower the average overall dimensionless transfer resistance $1/\langle \mathrm{S} \rangle_{\text{out}}$ the higher the conversion. This will require the channel and diffusion layers to be sufficiently thin and the reaction to be sufficiently fast.

Equation 7.6 may be used to determine a suitable channel length h associated with a desired conversion X to give

$$h_{\text{opt}} = \frac{W}{ka} \ln \left(\frac{1}{1 - X} \right). \tag{7.7}$$

[2] In case there are no ohmic limitations, the electrode effectiveness factor is close to 1, and the reaction rate will be approximately constant in the transverse x-direction.

[3] Note also the similarity with Eq. (7.18), the concentration profile in a flow-by configuration under limiting current conditions when replacing k_{m} with k. The reason is that both mass transfer and the considered first-order reaction are linear in the concentration.

A high conversion may be preferable to reduce separation costs of the outlet stream and avoid having to recirculate. However, it is not always desirable. For example, for an air-fed fuel cell or CO_2 electrolyser cathode, a high velocity with a low conversion may be preferable to maximise the reactant concentration in the channel. A high reactant concentration minimises the concentration overpotential and undesirable side reactions. Flowing faster will require a higher compressor duty or pumping power, which can also be a consideration.

7.4 Optimal electrolyte channel width

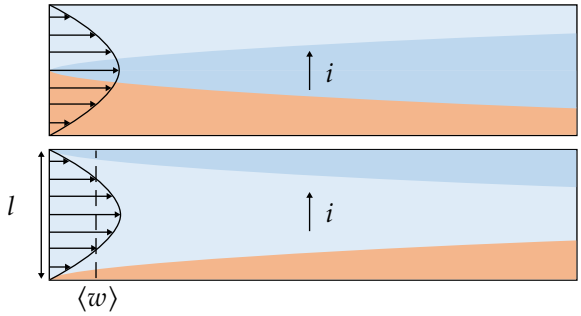

Figure 7.3: *In a membraneless flow battery, laminar electrolyte flow keeps the mixing region between two reactants (top, in this co-laminar configuration a light blue and heavier orange reactant mix in the centre) or the developing product boundary layers (bottom) away from the opposing electrodes. Note that the boundary layers are drawn in an idealised fashion and will be more spread out in reality.*

Usually, the flow channel, as seen from the membrane, is on the other side of the electrode. In this 'back-fed' configuration, the resistance is lower as ions do not have to traverse the flow channel. A front-fed configuration, in which the flow channel is on the other side, is also sometimes used. An example are *membraneless* or *micro-fluidic* redox flow batteries. When the flow is fast but still laminar, the products of the reaction can be transported out with the flow before they diffuse to the other side of the channel. The laminar boundary layers ensure separation, so that a membrane is not needed, see Fig. 7.3. Using a thin channel with a high-conductivity electrolyte, such a configuration can have a similar or lower ohmic drop compared to a configuration with a membrane without the cost, degradation and other limitations of membranes. In CO_2 electrolysers, a fluid channel between the cathode and a membrane is often used to supply water and minimise cross-over.

A thinner channel reduces the ohmic losses but increases the pumping losses. Therefore, there will be a channel width l for which the combined losses will be minimal. Here, we set out to find a relation for this optimal channel width.

For a cell thickness l_y in the direction normal to the flow and current, the electrode

area is $A = hl_y$, and the flow channel cross-sectional area reads ll_y. The power P_{res} dissipated by resistance is approximately given by the product of current $\langle j \rangle A$ and average potential drop $\langle j \rangle l/\kappa$, so[4]

$$\frac{P_{\text{res}}}{A} \approx \frac{\langle j \rangle^2 l}{\kappa}. \tag{7.8}$$

The laminar pressure drop is given by the Hagen-Poiseuille equation as[5]

$$\Delta p = 12\mu \frac{\langle w \rangle}{l^2} h. \tag{7.9}$$

The power dissipated by friction P_{fr} in the channel is given by the product of the volumetric flow-rate $ll_y\langle w \rangle$ and so

$$\frac{P_{\text{fr}}}{A} = \frac{12\mu\langle w \rangle^2}{l} = \frac{12\mu\langle j \rangle^2}{(nFXc_{\text{in}})^2 l^3}, \tag{7.10}$$

where we used Eqs. (7.15) and (7.6) to write $\langle w \rangle = \frac{\langle j \rangle}{nFlXc_{\text{in}}}$.

The optimal gap thickness l is that for which the combined power losses $P_{\text{fr}} + P_{\text{res}}$ are minimal. Solving $\frac{\partial}{\partial l}\left(\frac{P_{\text{fr}}}{A} + \frac{P_{\text{res}}}{A}\right) = 0$ for l, for constant X, gives

$$\boxed{l_{\text{opt}} = (36\mu\kappa)^{(1/4)} \sqrt{\frac{l}{nFXc_{\text{in}}}}.} \tag{7.11}$$

Using typical numbers $\mu = 1$ mPas and $\kappa = 1$ S/cm gives $l_{\text{opt}} = 140\ \mu\text{m}\sqrt{\frac{l[\text{m}]}{nc_{\text{in}}[\text{M}]X}}$ so that for $l = 1$ m and $Xc_{\text{in}} = 1$ M, the optimal gap is 140 μm wide.

7.5 Flow-by

7.5.1 Quasi-2D model

Figure 7.4 introduces a coordinate system with z along the flow and x in the perpendicular direction, from the flow channel to the catalyst layer or porous electrode. Sometimes, in the case of gaseous reactants, between the two a diffusion layer exists, as considered in chapter 5. In the case of liquid reactants, there is often no such layer.[6]

[4] We should actually average the product of the current and potential drop, instead of multiplying their averages. For not-too-large variations in $j(z)$, the difference between $\langle j^2 \rangle$ and $\langle j \rangle^2$ may be acceptably small to allow usage of this approximation.

[5] The derivation of this result proceeds similarly to the cylindrical case treated in footnote 11 of chapter 5. Using the planar Laplacian $\mathrm{d}^2/\mathrm{d}x^2$ gives a prefactor 12 instead of 8.

[6] In the case of a flow-by configuration, the porous electrode is sometimes referred to as a liquid-diffusion layer. However, on the pore surface the redox reactions take place, contrary to in a gas diffusion layer (GDL).

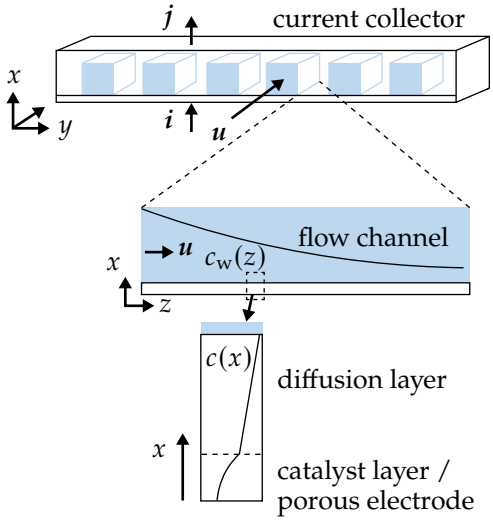

Figure 7.4: *A schematic of the metal current collector with carved-out flow channels (blue) in which the reactant concentration decreases along the flow direction (z) as well as in the direction inside the gas diffusion layer (x), towards the catalyst layer. The first and second close-ups represent the domains for the channel problem and the membrane-electrode-assembly (MEA) problem, respectively.*

The flow channels can be straight or form, for example, a serpentine *flow field* going back and forth many times, as shown in Figure 7.2. A first simplification is that we do not consider any variation in the y-direction, which is normal to both the current and the flow. There will obviously be differences in the concentration profiles directly below a flow channel or the *land area* where the current is collected; see Figure 7.4. Therefore, our model will be some sort of average over this y-direction.

The distance the fluid travels in the flow direction is typically of the order of $h \sim 0.1\text{-}10$ m. However, the flow channels ($l \sim 1$ mm) and porous electrodes (or diffusion layer with catalyst layer) (~100 μm) are generally much thinner in the x-direction. Therefore, typical diffusive fluxes $N_z \sim \frac{Dc}{h}$ due to the same concentration difference c in the z-direction are several orders of magnitude smaller than those $N_x \sim \frac{Dc}{l}$ in the x-direction: $\frac{N_z}{N_x} \sim \frac{l}{h} \ll 1$. So we can usually safely neglect diffusion parallel to the flow (N_z) and take the flux in this direction to be solely due to advection. In the x-direction, on the other hand, we will neglect any advection.

Considering advection only in the z-direction and diffusion only in the x-direction allows making separate models for each direction and coupling them afterwards. Respectively, these two decoupled problems are sometimes referred to [15] as

1. The *Channel problem* or *along-the-channel problem*, and
2. The membrane-electrode-assembly or *MEA problem*.

In the former we solve for the mean concentration $c_m(z)$, or the wall concentration $c_w(z)$, inside the flow channel as a function of the streamwise coordinate z. In the latter problem, we take these profiles as a given and calculate for each z the concentration profile $c(x)$ throughout the electrode (or diffusion and catalyst layers) and possibly the membrane. In the following sections, we will subsequently consider how to model these two problems analytically.

7.5.2 Channel problem

Figure 7.5 introduces again the x, z coordinate system, the channel dimensions (a streamwise 'height' h and channel thickness l) and flow channel velocity profile ($w(x)$, with average velocity $\langle w \rangle$). Neglecting the diffusion term ($D\frac{\partial^2 c}{\partial z^2}$) in the z-direction, as discussed in the previous section, the two-dimensional steady-state advection-diffusion equation (2.3) reads

$$0 = -w\frac{\partial c}{\partial z} + D\frac{\partial^2 c}{\partial x^2}\,. \tag{7.12}$$

The boundary conditions are: zero flux at the top wall, representing the current collector at $x = l$; and a prescribed but yet unknown flux $\frac{j}{nF} = D\frac{\mathrm{d}c_w}{\mathrm{d}x}$ at the flow channel-diffusion layer interface at $x = 0$. The channel problem consists of finding the concentration $c_w = c(x = 0)$. This concentration will provide the connection with or input to the MEA model.

Integrating Eq. (7.12) from $x = 0$ to $x = l$ gives for the wall flux[7]

$$\frac{j(z)}{nF} = -\frac{\mathrm{d}}{\mathrm{d}z}\int_0^l wc\mathrm{d}x = -\langle w \rangle l\frac{\mathrm{d}c_m}{\mathrm{d}z}, \tag{7.13}$$

where the integral $\int_0^l D\frac{\partial^2 c}{\partial x^2}\mathrm{d}x = D\frac{\partial c}{\partial x}\big|_l - D\frac{\partial c}{\partial x}\big|_0$ is evaluated using the boundary conditions shown in Figure 7.5. We defined the *cup-mixing concentration* as

$$c_m(z) \equiv \frac{1}{\langle w \rangle l}\int_0^l wc\mathrm{d}x. \tag{7.14}$$

This represents the average concentration that is obtained when letting liquid at a position x flow into a cup. It weights the concentration with the local velocity since faster-flowing liquid contributes more to what is collected.

Integrating Eq. (7.13) once more, but now in the z-direction, gives for the average current density $\langle j \rangle = \frac{1}{h}\int_0^h j\mathrm{d}z$

$$\boxed{\frac{\langle j \rangle h}{nF} = \langle w \rangle l\,(c_{in} - c_{out})\,.} \tag{7.15}$$

[7]Here, n is the positive number of electrons consumed or generated per molecule of reactant.

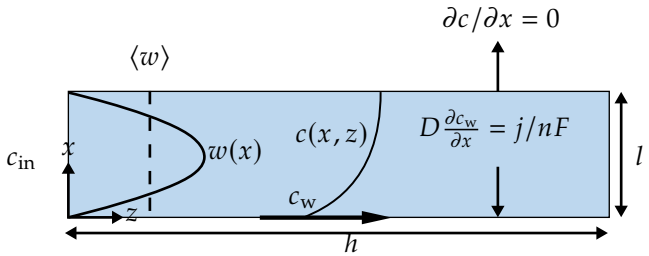

Figure 7.5: *A schematic drawing, introducing the (Neumann) boundary conditions at the two walls and the (Dirichlet) boundary condition c_{in} at the entrance of the flow channel, its dimensions (h and velocity profile ($w(x)$, with average velocity $\langle w \rangle$) in the flow channel. The channel problem consists of determining the 'wall' concentration c_{w} at the flow channel-diffusion layer interface at $x = 0$.*

Here, c_{in} and c_{out} are the cup mixing concentrations, at the inlet at $z = 0$ and at the outlet $z = h$.[8]

Using the definition in Eq. (7.17) gives for the molar flux

$$\boxed{\frac{j}{nF} = -l\langle w \rangle \frac{\mathrm{d}c_{\text{m}}}{\mathrm{d}z} = \text{Sh}\frac{D\,(c_{\text{m}} - c_{\text{w}})}{l}.} \tag{7.16}$$

Here, we introduced the *Sherwood number* Sh, representing the ratio between the flux $N = j/nF$ and a characteristic diffusion flux $D\frac{c_{\text{m}} - c_{\text{w}}}{l}$ so that

$$\text{Sh} \equiv \frac{Nl/D}{c_{\text{m}} - c_{\text{w}}}. \tag{7.17}$$

This is a dimensionless number, analogous to the *Nusselt number* for heat transport. In terms of the mass transfer coefficient $k_{\text{m}} = N/\Delta c$ used in chapter 4, we have $\text{Sh} = k_{\text{m}} l/D$. Near the entrance, the concentration profile is developing so that Sh will be very large.[9]

When $c_{\text{w}} = 0$, the flux cannot be further increased so that a limiting current arises. In this case, Eq. (7.16) is solved by

$$c_{\text{m}} = c_{\text{in}} \mathrm{e}^{-\frac{\langle \text{Sh} \rangle D}{\langle w \rangle l^2} z}. \tag{7.18}$$

Here, $\frac{\langle \text{Sh} \rangle D}{\langle w \rangle l^2} z = \frac{\langle k_{\text{m}} \rangle}{\langle w \rangle l} z$ and the running-average Sherwood number $\langle \text{Sh} \rangle (z) = \frac{1}{z}\int_0^z \text{Sh}\,\mathrm{d}z$. If the Sherwood number is constant, the cup-mixing average concentration c_{m} decreases exponentially over a length scale $\frac{\langle w \rangle l^2}{\text{Sh}D}$, independent of h. Because the rate

[8] With l_y the width in the y-direction, the number of moles $l l_y \langle w \rangle (c_{\text{in}} - c_{\text{m}})$ that leave the channel equate to $\langle j \rangle h l_y / nF$, giving Eq. (7.15).

[9] For a constant velocity $\langle w \rangle$ this is similar to the Sands solution $\text{Sh} = l/\delta = \sqrt{\pi l^2/4tD}$ but with $z/\langle w \rangle$ instead of t. Further down the channel, as the concentration profile fully develops, Exercise 7.3 shows that Sh becomes $35/13 \approx 2.7$.

at which concentration is removed by diffusion is proportional to the concentration, an exponential decrease results. Therefore, removing the last bit of reactant concentration from the flow channel becomes increasingly difficult.

To find a general solution to Eq. (7.16), also valid under non-limiting current conditions, requires an expression for c_w. We know it will be lower than c_m to provide the required diffusion flux towards $x = 0$, see Figures 7.5 and 7.6. Finding an expression for c_w will be the goal of the MEA problem, which we will consider in the next section.

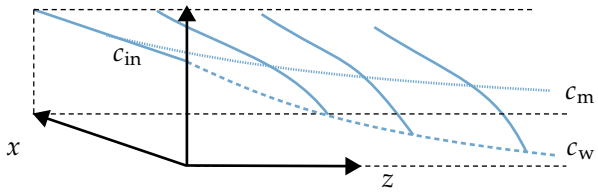

Figure 7.6: *An example concentration profile showing that the cup-mixing average concentration c_m and wall concentration c_w decreases in the streamwise z-direction. The concentration profile also decreases towards $x = 0$, where reactants enter the porous electrode or gas diffusion layer. The wall concentration c_w is always lower than c_m providing the necessary diffusion flux.*

7.5.3 MEA problem

Here, we focus on modelling the porous electrode, or the diffusion and catalyst layer, in the case of gaseous reactants. Figure 7.7 depicts these layers as resistances in series, sandwiched between the flow channel and the membrane. As nothing reacts in the diffusion layer, the reactant flux from the flow channel can be equated to that over the diffusion layer and to that entering the catalyst layer. Equation (7.16) is then extended to

$$\frac{j}{nF} = -l\langle w\rangle \frac{\mathrm{d}c_m}{\mathrm{d}z} = \mathrm{Sh}\frac{D\,(c_m - c_w)}{l} = \mathrm{Sh}_d \frac{D\,(c_w - c_r)}{l} = \kappa c_r = \mathrm{S}\frac{D c_m}{l}. \tag{7.19}$$

Applying Fick's law $\frac{j}{nF} = D_d \frac{c_w - c_r}{l_d}$ over the diffusion layer gives

$$\mathrm{Sh}_d = \frac{D_d}{D}\frac{l}{l_d}. \tag{7.20}$$

In the third equation of Eq. (7.19), we assumed a reaction that is first order in the concentration c_r, with an integral reaction rate coefficient κ (see Fig. 7.7).[10] As no reactants enter the membrane, the flux can be equated to this reaction flux.

[10] We introduce a new different symbol $\kappa = j/nFc_r$ here, because this rate-constant is an integral value for an entire reactive layer. Unlike the previously used local rate coefficient $k = N_\perp/c$, it does not multiply

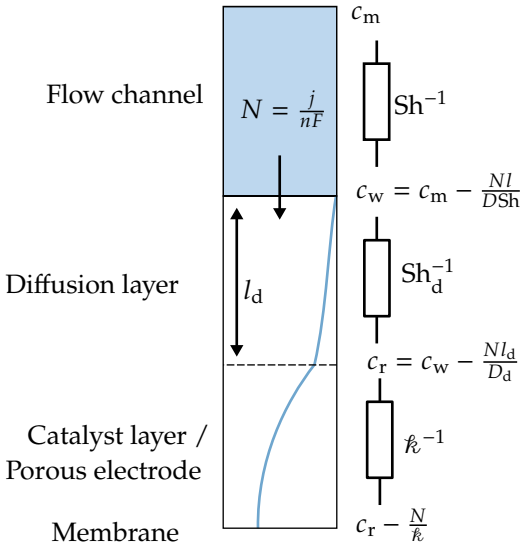

Figure 7.7: *A membrane electrode assembly (MEA) consists of from top to bottom: (sometimes) a diffusion layer in which reactants enter from the flow channel (in blue) with a concentration c_w and leave after a distance l_d to the porous electrode or catalyst layer (below the dotted line which is entered with a concentration c_r. The membrane is not shown and would be below this figure.*

The final expression of Eq. (7.19) is actually a definition of the *overall dimensionless transfer coefficient* S. Since the preceding equations constitute three linear equations for the three unknowns c_w, c_r, and c_m, these may be solved for c_m to give

$$\frac{1}{\mathrm{S}} = \frac{1}{\mathrm{Sh}} + \frac{1}{\mathrm{Sh}_\mathrm{d}} + \frac{D}{kl}. \tag{7.21}$$

The molar flux and concentration differences in Eq. (7.19) are analogous to the current density and potential differences in Ohm's law, Eq. 1.8, respectively. The dimensionless *mass transfer resistances* $1/\mathrm{Sh}$ and $1/\mathrm{Sh}_\mathrm{d}$ and the reaction resistance D/kl then form a series circuit as shown in Figure 7.8. The combined resistance $\frac{1}{\mathrm{Sh}} + \frac{1}{\mathrm{Sh}_\mathrm{d}}$ is the overall resistance to mass transfer. When it is much smaller than kl/D, mass transfer is 'limiting' and provides the dominant resistance. When, on the other hand, it is much smaller than kl/D, the process is said to be *reaction-limited*.

Eq. (7.19) is solved by

$$\boxed{c_\mathrm{m} = c_\mathrm{in} \mathrm{e}^{-\frac{\langle S \rangle D}{\langle w \rangle l^2} z},} \tag{7.22}$$

the local concentration c but a boundary value c_r and is defined relative to the electrode area rather than the solid-electrolyte interfacial area.

where the running-average value $\langle \mathrm{S} \rangle (z) = \frac{1}{z}\int_0^z \mathrm{S}\mathrm{d}z$. The only difference with Eq. (7.18) is that the dimensionless mass transfer coefficient for the channel, Sh, is replaced by the overall transfer coefficient S, which also includes the transfer resistance of the diffusion layer, if present, and that of the reaction.[11]

The current density will decrease as the concentration c_m depletes along the channel. Using Eq. (7.22), Eq. (7.19) gives the local current density as

$$j = nF\mathrm{S}\frac{Dc_\mathrm{in}}{l}\mathrm{e}^{-\frac{\langle \mathrm{S} \rangle D}{\langle w \rangle l^2} z}. \tag{7.23}$$

Upon integrating this, or Eq. (7.19), the channel average flux $\langle j \rangle \equiv \frac{1}{h}\int_0^h j\mathrm{d}z$ gives again Eq. (7.15):

$$\langle j \rangle = nF\langle w \rangle l\,(c_\mathrm{in} - c_\mathrm{m}) = nF\langle w \rangle l c_\mathrm{in}\left(1 - \mathrm{e}^{-\frac{\langle \mathrm{S} \rangle D}{\langle w \rangle l^2} z}\right), \tag{7.24}$$

where in the second expression, we inserted Eq. (7.22).

7.5.4 Cell model

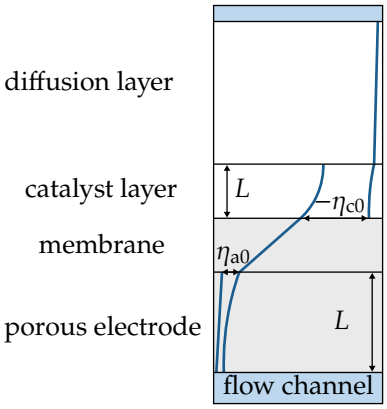

Figure 7.8: *The potential profiles throughout a cell at a given streamwise coordinate z. Reactants diffuse from the cathode flow channel (in blue) through a diffusion layer into the catalyst layer. In this example, the anode consists of a porous electrode.*

Besides its effect on conversion, reactant depletion in the streamwise direction also impacts the current distribution and energy efficiency, which we will investigate here. In the case of first-order Tafel kinetics, Eq. (3.B.104) gives

[11] In the absence of mass-transfer limitations, $S = \mathrm{k}l/D$ and, with $\mathrm{k} = aLk$, Eq. (7.3) is retained upon replacing l with L. Similar to Eq. (7.7), Eq. (7.22) gives an optimal channel length $h_\mathrm{opt} = \frac{\langle w \rangle l^2}{\langle \mathrm{S} \rangle_\mathrm{out} D} \ln\left(\frac{1}{1-X}\right)$.

$$j = \mathcal{E}\frac{c_\mathrm{r}}{c_\mathrm{in}} J_* \mathrm{e}^{\eta_0/b}. \tag{7.25}$$

Here $\eta_0 = \eta_{a0} > 0$, or $-\eta_{c0} > 0$ is the activation overpotential of the electrode under consideration at the membrane-electrode interface at $x = 0$, see Fig. 7.8.

Adding the second and third expression in Fig. 7.7, and using Eq. (7.21), gives

$$c_\mathrm{r} = c_\mathrm{m}\left(1 - \frac{j}{j_\mathrm{lim}}\right) \quad \text{where } j_\mathrm{lim} = nF\frac{1}{\frac{1}{\mathrm{Sh}} + \frac{1}{\mathrm{Sh}_\mathrm{d}}}\frac{Dc_\mathrm{m}}{l}. \tag{7.26}$$

Equations (7.25) and (7.26) combine to give

$$\boxed{\eta_0 = b\ln\left(\frac{j/\mathcal{E}J_*}{\frac{c_\mathrm{m}}{c_\mathrm{in}}\left(1 - \frac{j}{j_\mathrm{lim}}\right)}\right).} \tag{7.27}$$

This relation is similar to Eq. (4.27), which we derived for a battery particle. Also in that case, diffusion and reaction resistances acted in series.

In chapter 3 on porous electrodes, we derived approximate expressions for the effectiveness factor $\mathcal{E}$ in the presence of diffusion limitations or ohmic limitations that we can insert here.[12]

In case of no ohmic limitations but strong diffusion limitations, Eq. (3.59) gives for the effectiveness factor $\mathcal{E} = \frac{nFDc_\mathrm{r}}{jL}$. Inserting in Eq. (7.27) and using Eq. (7.26), gives

$$\eta_0 \approx 2b\ln\left(\frac{j/\sqrt{j_D J_*}}{1 - \frac{j}{j_\mathrm{lim}}}\right), \tag{7.28}$$

where $j_D = nFDc_\mathrm{m}/L$ is based on the channel cup-mixing concentration. Note that the entire activation overpotential, including the concentration overpotential $b\ln\left(\frac{1}{1-\frac{j}{j_\mathrm{lim}}}\right)$, is doubled.

A schematic overview of the potential and overpotential profiles is shown in Figure 7.8. The flow channel-electrode or flow channel-diffusion layer interface can be assumed to have a spatially constant electrostatic potential, because it is connected to a well-conducting current collector, see Fig. 7.4. The constant cell voltage can thus be taken as the difference between the potentials in the two current collectors. From Eq. (3.39), we can write the overpotential at the electrode-membrane interface as[13]

$$\eta_\mathrm{a0} - \eta_\mathrm{c0} = V_\mathrm{eq} - V_\mathrm{cell} - jAR. \tag{7.29}$$

[12] Equation (3.67), for combined ohmic and diffusion limitations will not be applicable in case of the 'back-fed' electrode considered here, where reactants and ions come from opposite sides because it was derived for the case that reactants and ions come from the side. In the case of strong ohmic limitations, a low effectiveness factor gives a narrow reaction zone on the membrane side of the electrode. This will add approximately the electrode thickness L to l to determine the limiting current.

[13] This is always positive, noting that $\eta_\mathrm{c} < 0$. Under galvanic conditions $V_\mathrm{eq} > V_\mathrm{cell} > 0$ and under electrolytic conditions $V_\mathrm{cell} < V_\mathrm{eq} < 0$.

We will consider a single porous electrode and neglect the activation overpotential of the other electrode.[14] The overpotential may vary throughout the electrode/catalyst layer. Therefore, as discussed in the porous electrode chapter 3, the overpotential value at the interface with the membrane, where the ionic current comes from, should be used.

Note that since AR, V_{cell} and V_{eq} are constant, Eq. (7.29) implies that, while the reactant concentration goes down and the concentration potential goes up in the stream-wise z-direction, $\eta + jAR$ remains constant. This forces the current density $j(z)$ to go down with increasing z.

Using Eqs. (7.27) and (7.22) in Eq. (7.29) gives

$$\boxed{V_{\text{cell}} \approx V_{\text{eq}} - \left(ARj + b \ln\left(\frac{j/J_* \mathcal{E}}{1 - j/j_{\text{lim}}} \right) + \frac{\langle \text{S} \rangle D}{\langle w \rangle l^2} z \right),} \tag{7.30}$$

where Eqs. (7.25) and (7.21) combine to give for the reaction rate coefficient $k = j/nFc_{\text{r}}$

$$\text{S} = \left(\frac{1}{\text{Sh}} + \frac{1}{\text{Sh}_{\text{d}}} + \frac{nFDc_{\text{in}}/l}{\mathcal{E} J_* \text{e}^{(V_{\text{eq}} - V_{\text{cell}} - jAR)/b}} \right)^{-1}. \tag{7.31}$$

The quasi-two-dimensional cell model of Eq. (7.30) succinctly summarises many of the concepts we considered in this book. The equilibrium potential V_{eq} and ohmic losses ARj, considered in chapter 1. The concentration overpotential $b \ln(c_{\text{m}}/c_{\text{r}}) = -b \ln(1 - j/j_{\text{lim}})$ studied in chapter 2 is extended in this chapter to include both the flow channel and diffusion layer, using the series expression of Eq. (7.26). The porous electrode activation losses $b \ln(j/J_* \mathcal{E})$ were discussed in chapter 3. The final term represents a second part of the concentration overpotential $b \ln(c_{\text{in}}/c_{\text{m}})$ and is due to the decrease in the cup-mixing average concentration c_{m} with increasing z. The approximately exponential decrease in concentration results in a linearly increasing overpotential.[15]

Providing you with an understanding of this and similar equations has been a major aim of this book. In general, this equation has to be solved numerically for $j(z)$. Section 7.3 considers the simplest case, in which there are concentration variations only in the z-direction.

7.6 Summary

- Due to the large aspect ratio of most flow channels, streamwise diffusion can be neglected, so that a 1D+1D modelling approach allows solving the *along the*

[14] Or assume it can be linearised and included in AR. Alternatively, in case the anode and cathode happen to have the same thickness and exchange current density, their Tafel slopes may be added in b so Eq. (7.27) represents the combined activation losses.

[15] This is similar to the second term in Eq. (4.29), which we derived for a battery particle. Here, a concentration that linearly decreases in time led to a linearly increasing activation overpotential.

channel and MEA problems independently. Along the channel, the reactant cup-mixing concentration decreases, viz. $\frac{\mathrm{d}c_\mathrm{m}}{\mathrm{d}z} = -\mathrm{Sh}\frac{D(c_\mathrm{m}-c_\mathrm{w})}{l^2\langle w\rangle}$ (7.16) so that $c_\mathrm{m} = c_\mathrm{in}\mathrm{e}^{-\frac{\langle \mathrm{S}\rangle D}{\langle w\rangle l^2}z}$, (7.22), where the dimensionless transfer resistance $\frac{1}{\mathrm{S}}=\frac{1}{\mathrm{Sh}} + \frac{1}{\mathrm{Sh_d}} + \frac{D}{\hat{k}l}$ (7.21) consists of the sum of those in the channel, diffusion layer, and due to the reaction, respectively.

- Inserting this exponentially decreasing solution into the expression for the electrode activation overpotential gives, see Eqs. (7.27) and (7.30):

$$\eta_0 = b\ln\left(\frac{j/\mathcal{E}J_*}{\frac{c_\mathrm{m}}{c_\mathrm{in}}\left(1-\frac{j}{j_\mathrm{lim}}\right)}\right) = b\ln\left(\frac{j/J_*\mathcal{E}}{1-\frac{j}{j_\mathrm{lim}}}\right) + \frac{\langle \mathrm{S}\rangle D}{\langle w\rangle l^2}z, \tag{7.32}$$

  gives a concentration polarisation that linearly increases along the channel.

- For a flow channel in between the electrode and membrane, a larger width increases the ohmic drop, while a smaller width increases the power dissipated in pumping. At constant conversion, an optimal gap width $l_\mathrm{opt} = (36\mu\kappa)^{(1/4)}\sqrt{\frac{l}{nFc_\mathrm{in}X}}$ (7.11) is obtained.

- In a flow-through electrode, neglecting streamwise diffusion, the porous electrode advection-reaction equation $W\frac{\mathrm{d}c}{\mathrm{d}z} = \frac{aj_\perp}{nF}$ gives an exponentially decreasing concentration $c(z) = c_\mathrm{in}\mathrm{e}^{-\frac{ka}{W}z}$ in case of constant first-order reaction rate coefficient k.

Exercise 7.1

Often in electrolysers and flow batteries it will be beneficial to have a high conversion, in order to avoid the process of separating the products from the reactants, or reach a low state of charge in a single pass, respectively.

a. Assuming a constant overall transfer coefficient S = 0.5, what value for the dimensionless (Graetz) number $\frac{\langle w \rangle l^2}{hD}$ gives a conversion of 99 %?

b. What is the ratio between the average current density and the current density near the inlet in this case?

c. If a flow field is used of length h = 0.1 m and channel thickness l=1 mm, and the diffusivity $D = 2{\cdot}10^{-5}$ m^2/s. What flow velocity is required to reach this desired conversion?

d. What is the conversion that can be reached if a serpentine flow field is used instead, with n turns so that the total channel length becomes nh. Give your answer in the form of a formula containing only n as a free parameter

Exercise 7.2

Consider a unitised regenerative fuel cell running on hydrogen and air (f = 21 % oxygen by volume, assume ideal gas behaviour) at 80 °C and atmospheric pressure. The electrode dimensions h and w are both 10 cm, giving an area $A = hw = 100$ cm^2. A current I = 100 A is used so that the current density $j = I/A = 1$ A/cm^2. For a l = 1 mm wide single cathode flow channel without a flow field, what average inlet air velocity $\langle w \rangle$ is minimally required to supply enough oxygen?

Exercise 7.3

a. Assuming $\frac{\partial c}{\partial z}$ is constant, give the solution $c(x)$ of Eq. (7.12) for $c(x)$ for a parabolic laminar flow profile $w(x) = 6\langle w \rangle \frac{x}{l}\left(1 - \frac{x}{l}\right)$ using the boundary conditions $\frac{\partial c}{\partial x} = 0$ at $x = l$ and $c = c_\mathrm{w}$ at $x = 0$.

b. Calculate the cup-mixing concentration $c_\mathrm{m} \equiv \frac{1}{\langle w \rangle l}\int_0^l wc\mathrm{d}x$ in terms of c_w and $\frac{\partial c}{\partial z}$.

c. Assuming $\frac{\partial c}{\partial z} = \frac{\partial c_\mathrm{m}}{\partial z}$, calculate the Sherwood number from Eq. (7.16).

Exercises 7.4-7.15

Fill in the missing steps in the main text, indicated by the symbol .

*Appendices **

7.A *Dimensionless transport equations*

The Sherwood number of Eq. (7.A.33) can also be defined as the ratio between dimensionless flux and dimensionless concentration difference as

$$\mathrm{Sh} \equiv \frac{\bar{j}_l}{\bar{c}_\mathrm{m} - \bar{c}_\mathrm{w}}, \tag{7.A.33}$$

where $\bar{c} = c/c_\mathrm{in}$ and

$$\bar{j}_l = \frac{j}{J_l} \quad \text{where } J_l = nF\frac{Dc_\mathrm{in}}{l}, \tag{7.A.34}$$

is relative to the characteristic diffusion driven flux $nFDc_\mathrm{in}/l$. Note that J_l is similar to J_D used in porous electrode modelling, except that the length scale used is that of the flow channel, l, rather than that of the catalyst layer, L. Introducing also a non-dimensional axial coordinate $\bar{z} = z/h$, running from zero at the inlet to 1 at the outlet, we can write Eq. (7.16) as

$$\mathrm{Gz}\frac{\mathrm{d}\bar{c}_\mathrm{m}}{\mathrm{d}\bar{z}} = -\bar{j}_l = -\mathrm{Sh}\left(\bar{c}_\mathrm{m} - \bar{c}_\mathrm{w}\right), \tag{7.A.35}$$

where the *Graetz* number

$$\mathrm{Gz} \equiv \frac{\langle w\rangle l^2}{hD}, \tag{7.A.36}$$

is similar to the *Péclet* number[16] $\mathrm{Pe} = \frac{\langle w\rangle l}{D}$, but with a different length scale l^2/h rather than l. From Eq. (7.12), the characteristic magnitude of the advection and diffusion terms are $\langle w\rangle c/h$ and Dc/l^2 respectively. The Graetz number provides the ratio of these two characteristic values. If $\mathrm{Gz} \gg 1$, advection dominates. If $\mathrm{Gz} \ll 1$, transverse diffusion dominates.

Non-dimensionalising all concentrations with c_in, Eq. (7.19) becomes

$$\bar{j}_l = \mathrm{Sh}\left(\bar{c}_\mathrm{m} - \bar{c}_\mathrm{w}\right) = \mathrm{Sh}_\mathrm{d}\left(\bar{c}_\mathrm{w} - \bar{c}_\mathrm{r}\right) = \bar{k}\bar{c}_\mathrm{r} \equiv \mathrm{S}\bar{c}_\mathrm{m}, \tag{7.A.37}$$

[16] This is in turn similar to the *Reynolds number* $\mathrm{Re} = \frac{\langle w\rangle l}{\nu}$, but with the diffusivity D instead of the kinematic viscosity $\nu = \mu/\rho$.

where the dimensionless reaction rate constant is

$$\bar{k} = \frac{k}{D/l}. \tag{7.A.38}$$

Using Eq. (7.A.37) in Eq. (7.A.35) gives the dimensionless form of Eq. (7.A.39) as

$$\mathrm{Gz}\frac{\mathrm{d}\bar{c}_\mathrm{m}}{\mathrm{d}\bar{z}} = -\bar{j}_l = -\mathrm{S}\bar{c}_\mathrm{m}. \tag{7.A.39}$$

This is solved by

$$\bar{c}_\mathrm{m} = \mathrm{e}^{-\frac{\langle \mathrm{S} \rangle}{\mathrm{Gz}}\bar{z}}. \tag{7.A.40}$$

Eqs. (7.A.40) and (7.A.39) give the flux at $\bar{z}$ as

$$j = j_l \mathrm{S}\mathrm{e}^{-\frac{\langle \mathrm{S} \rangle}{\mathrm{Gz}}\bar{z}}. \tag{7.A.41}$$

Upon integration, the channel average flux $\left\langle \bar{j}_l \right\rangle \equiv \int_0^1 \bar{j}_l d\bar{z}$ reads

$$\left\langle \bar{j}_l \right\rangle = \mathrm{Gz}\left(1 - \bar{c}_\mathrm{m}^\mathrm{out}\right) = \mathrm{Gz}\left(1 - \mathrm{e}^{-\frac{\langle \mathrm{S} \rangle_\mathrm{out}}{\mathrm{Gz}}}\right). \tag{7.A.42}$$

This is the dimensionless version of Eq. (7.24). Finally, the conversion in dimensionless notation reads

$$X \equiv 1 - \bar{c}_\mathrm{m}^\mathrm{out} = 1 - \mathrm{e}^{-\frac{\langle \mathrm{S} \rangle_\mathrm{out}}{\mathrm{Gz}}}. \tag{7.A.43}$$

7.B *Dimensionless cell model*

With $j/nF = k c_\mathrm{r}$ and Eq. (7.A.38), Eq. (7.25) gives with $\bar{\eta}_0 = |\eta_0|/b$:

$$\bar{k} = \frac{\mathcal{E} J_* e^{\bar{\eta}_0}}{J_l}. \tag{7.B.44}$$

Non-dimensionalising Eq. (7.29) gives, neglecting as in the main text one of the overpotentials

$$\bar{\eta}_0 = \Delta\bar{V} - \bar{j}_l \bar{R}, \tag{7.B.45}$$

where $\bar{R} = \frac{AR j_l}{b}$ and $\Delta\bar{V} \equiv \frac{|V_\mathrm{eq} - V_\mathrm{cell}|}{b}$. With Eqs. (7.A.38) and (7.B.44), Eq. (7.21) becomes

$$\frac{1}{\mathrm{S}} = \frac{1}{\mathrm{Sh}_\mathrm{tot}} + \frac{1}{\frac{J_*}{J_l}\mathrm{e}^{\Delta\bar{V} - \bar{j}_l\bar{R}}}, \tag{7.B.46}$$

where we define $\frac{1}{\mathrm{Sh}_\mathrm{tot}} \equiv \frac{1}{\mathrm{Sh}} + \frac{1}{\mathrm{Sh}_\mathrm{d}}$. This can then be used in Eq. (7.A.39) to give

$$\mathrm{Gz}\frac{\mathrm{d}\left(\bar{j}_l/\mathrm{S}\right)}{\mathrm{d}\bar{z}} = -\bar{j}_l. \tag{7.B.47}$$

In general, this ordinary differential equation has to be solved numerically.

Chapter 8

Additional exercises

Exercise 8.1 constitutes an exercise encompassing knowledge from various chapters. Exercises 8.2-8.8 constitute a 3-hour closed-book practice exam of 40 points in total. You may use only the formula sheet. The answers are provided from page 203 onwards. A pass requires a minimum of 22 points.

Exercise 8.1

In this additional exercise we will build up an analytical cell model, including much of the theory discussed in the various chapters. For definiteness, let's consider a water electrolyser, for making hydrogen. Try initially to answer the questions without referring to the text. Towards the end of the questions, you may have to look up a few things.

a. Give an expression for the cell voltage as a function of current density j, considering only the equilibrium potential V_{eq} and the area-specific resistance AR.

b. When the resistance is purely due to the finite conductivity κ of a liquid electrolyte in a microporous separator with thickness l and porosity ϵ, give an expression for AR, assuming Bruggeman's relation.

c. What term has to be added to the cell voltage model when we include the activation overpotential of a smooth planar anode (neglecting that of the cathode) satisfying Tafel kinetics with Tafel slope b and exchange current density j_*?

d. If the same anode material is turned into a porous electrode with volumetric surface area a and thickness L, what is the effective total exchange current density?

e. If the effectiveness factor of the electrode is $\mathcal{E}$, give an expression for the activation overpotential.

f. Give an expression for the effectiveness factor $\mathcal{E} \ll 1$ in terms of the Thiele modulus M.

g. If the effective electrode conductivity is κ, give an expression for the Thiele modulus in case of ohmic limitations inside the electrode.

h. In alkaline water electrolysis, per electron, one hydroxide ion (OH^-) is produced at the cathode and consumed at the anode. Consider two electrodes with a gap of thickness d in between them, in the presence of a large surplus of supporting electrolyte that does not contain OH^-. Give an expression for the limiting current density due to the finite concentration c and diffusivity D of OH^-.

i. Also give an expression for the limiting current density in the absence of a supporting electrolyte.

j. The oxygen evolution reaction at the anode is first-order in the OH^- concentration. Assuming Tafel kinetics on a planar electrode, provide an expression for the concentration overpotential in terms of the limiting current density j_{lim}.

k. Due to the supporting electrolyte, ohmic limitations inside the electrode have disappeared, while diffusion limitations due to OH^- exist. Assuming the concentration at the 'entrance' of the porous electrode is c, give an expression for $\mathcal{E} \ll 1$.

l. Give also the expression for $\mathcal{E} \ll 1$ in the absence of a supporting electrolyte when the charge transfer coefficient of the oxidation reaction is α.

m. Assume that the anode consists of porous particles with small nanopores that cause the hydroxide diffusivity to decrease to a value D. If the current is switched on at $t = 0$ and we approximate the resulting concentration profile with a region of constant concentration gradient, give an expression for the limiting current density.

n. In a conventional 'gap electrolyser' configuration, a flow parallel to the electrodes in the gap of thickness d between anode and cathode is added to remove the heat of the reaction. When the flowing electrolyte contains a contaminant that reacts very rapidly at the anode surface, and the Sherwood number can be approximated by a constant Sh, after what distance is its concentration reduced by a factor $1/e = 0.368$?

o. If the majority of the losses are due to ohmic resistance in the cathodic gap, at what height do hydrogen bubbles decrease the current density by 1% compared to that at the bottom? Assume that Bruggeman's relation holds and that the liquid velocity can be neglected.

Exercise 8.2

Air with $f = 21$ vol% oxygen at ambient conditions enters a PEM fuel cell cathode flow channel of thickness $l = 1$ mm and length $h = 0.1$ m, sufficiently long to approximate the channel Sherwood number with a constant value $\mathrm{Sh} = 2.7$. The hydrophobic diffusion layer between the flow channel and the catalyst layer has a thickness $l_\mathrm{d} = 0.6$ mm, porosity $\epsilon_\mathrm{d} = 0.8$, and squared tortuosity $\tau^2 = 1.7$, and can be assumed to be devoid of water. The molecular diffusion coefficient of oxygen in air $D_\mathrm{m} = 2 \cdot 10^{-5}\ \mathrm{m}^2/\mathrm{s}$. The catalyst layer consists of wet agglomerates of approximately equal and spherical shape, with radius $R = 10^{-6}$ m, and an effective oxygen diffusion coefficient $D_\mathrm{agg} = 10^{-9}\ \mathrm{m}^2/\mathrm{s}$. The dissolved oxygen concentration will be $c = 1\ \mathrm{mol}/\mathrm{m}^3$ at the agglomerate surface. The fuel cell is operated at $1\ \mathrm{A}/\mathrm{cm}^2$.

a. (3) Neglecting all other transport losses, give a rough approximate value for the effectiveness factor $\mathcal{E}_\mathrm{a}$ inside an agglomerate near the diffusion layer.

b. (3) What average airflow velocity $\langle w \rangle$ in the flow channel will be minimally required to supply enough oxygen to sustain the cathodic reaction?

c. (5) Assuming $\langle w \rangle$ is much larger than the value calculated in the previous question, give an estimate of the limiting current density j_lim.

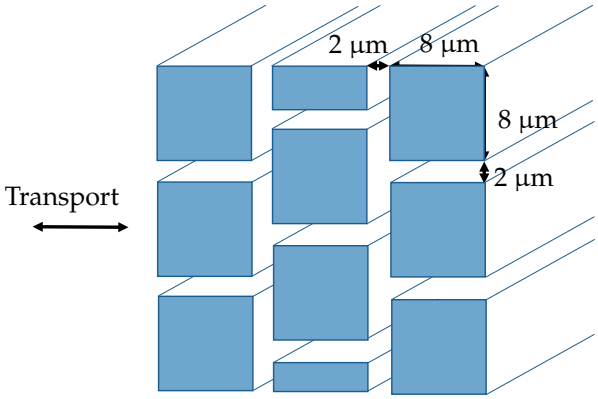

Exercise 8.3

Consider the medium schematically depicted above. The indicated pattern extends into *all three* directions x, y, and z indefinitely. The transport takes place in the horizontal direction as indicated by the arrow.

a. (1) Use its definition to estimate the tortuosity of this porous medium in the indicated transport direction.

b. (1) Calculate the porosity of this material.

c. (1) Using your values at a) and b), does this medium satisfy Bruggeman's relation numerically? Why (not)?

d. (1) In case of transport normal to the indicated transport direction, into the paper, parallel to the beam-like structure, can a higher, lower, or equal diffusion flux be obtained with equal concentration gradient and why?

e. (1) Calculate the volumetric surface area a of this material.

Exercise 8.4

A special type of membraneless alkaline water electrolyser consists of two parallel plates, a very small distance $l = 0.01$ mm apart, so that it can operate with low ohmic losses even at low electrolyte concentrations. Assume an electrolyte with concentration $c = 0.1$ M, consisting of potassium cations K^+ with diffusion coefficient $D_+ = 2 \cdot 10^{-9}$ m^2/s and hydroxide anions OH^- with diffusion coefficient $D_- = 5 \cdot 10^{-9}$ m^2/s. The effects of electrode end-effects, water consumption, flow, and bubbles can be neglected, so you can consider a one-dimensional concentration profile between $x = 0$ at the anode and $x = l$ at the cathode. Assume ambient conditions.

a. (5) Give the steady-state electrolyte potential drop $\Delta\phi$ between the electrodes when operating at a current density j, equal to 80 % of the limiting current density j_{lim}. *Hint: the total amount of electrolyte will remain constant after switching on the current. Consider what will be the relation between cation concentration and potential.*

b. (4) A monovalent supporting electrolyte, with anion and cation diffusivities both equal to 10^{-9} m^2/s, is added to give a supporting electrolyte concentration of 1 M. What will be the approximate electrolyte potential drop $\Delta\phi$ over the gap between the electrodes at a current density equal to 80 % of the *new* limiting current density?

Exercise 8.5

a. (2) Explain under what assumptions the moving reaction zone model and the single particle model for porous battery electrodes can be used, respectively. Illustrate your explanation with quantitative criteria in the form of formulas.

Exercise 8.6

Consider a planar anode for a redox reaction, satisfying concentration-independent Butler-Volmer kinetics with an exchange current density j_* and charge transfer coefficient α.

a. (1) Under what condition(s) does the activation overpotential η increase linearly with increasing current density? Provide criteria in the form of a formula, or formulas.
b. (2) Derive an expression for the equivalent area-specific resistance AR in this case.

Exercise 8.7

Consider a high-pressure zero-gap electrolyser with electrolyte flowing up near the electrodes due to natural convection of bubbles produced in the reaction, and back through a downcomer after removal of these bubbles. The laminar flow in between the electrodes of height h and their respective current collectors at a distance l can be assumed to be laminar and described by the planar Hagen-Poiseuille equation.

a. (4) At very low gas fractions, neglecting bubble slip, and friction in the downcomer, the superficial liquid recirculation velocity W_l near the electrodes increases proportional to the square root of the current density j. Why? Use formulas to explain your answer.
b. (2) Will viscous friction in the downcomer increase or decrease the gas fraction near the electrodes? Why?

Exercise 8.8

a. (4) Consider a porous anode of volumetric surface area a and thickness L whose pores are filled with a supporting electrolyte, giving an effective ionic conductivity κ. The oxidation reaction under consideration satisfies concentration-independent Tafel kinetics with a Tafel slope b and exchange current density j_*. Give an approximate equation for the activation overpotential η_0 at the location where the ionic current leaves the electrode, as a function of current density j, including the effect of ohmic limitations. Use it to derive that for high current densities the effective Tafel slope $\frac{\partial \eta_0}{\partial \ln j} = j\frac{\partial \eta_0}{\partial j}$ equals $2b$. Also, explain, in words, the reason for this Tafel slope doubling.

Answers to exercises

CHAPTER 1

***1.1*:** -0.3 V

***1.2*:** $\frac{V_{\mathrm{eq}}-\eta}{2AR}$

***1.3*:**

a. $b_{\mathrm{a}} + b_{\mathrm{c}}$
b. $\frac{1}{1/\alpha_{\mathrm{a}}+1/\alpha_{\mathrm{c}}} = \frac{\alpha_{\mathrm{a}}\alpha_{\mathrm{c}}}{\alpha_{\mathrm{a}}+\alpha_{\mathrm{c}}}$
c. $j_{*\mathrm{a}}^{b_{\mathrm{a}}/b}\, j_{*\mathrm{c}}^{b_{\mathrm{c}}/b} = j_{*\mathrm{a}}^{\alpha/\alpha_{\mathrm{a}}}\, j_{*\mathrm{c}}^{\alpha/\alpha_{\mathrm{c}}}$

***1.4*:**

a. $7.2 \cdot 10^3$ m^2
b. 63 %

CHAPTER 2

***2.1*:**

a. 4
b. $4F\frac{Dc}{L}$
c. $4F\frac{Dc}{L}\epsilon$

***2.2*:**

a. $\frac{D_{\mathrm{a}}}{2(1-t_+)}$
b. $\frac{j(1-t_+)}{FD}\left(\frac{L}{2}-x\right)+c$
c. 2.1×10^{-10} m^2

d. Minutes, yes, $\frac{2FDc/L}{1-t_+}$

***2.3*:**

a. Dc/L
b. $c_0 \frac{\mathrm{e}^{ux/D} - \mathrm{e}^{uL/D}}{1-\mathrm{e}^{uL/D}}$
c. $N = N_0 \frac{\mathrm{Pe}}{\mathrm{e}^{\mathrm{Pe}}-1} e^{\mathrm{Pe}}$
d. $3.2 \cdot 10^{-6}$ m/s

CHAPTER 3

***3.1*:**

a. 0.4
b. 10 μm

***3.2*:** 1.93 A/cm^2

***3.3*:**

a. $|\eta| \ll \mathcal{R}T/F$
b. $\frac{\mathcal{R}T/F}{aLj_*}$
c. $j \frac{\sinh(\nu(1-x/L))}{\sinh(\nu)}$
d. $\frac{\tanh(\nu)}{\nu}$

***3.4*:** 0.18 V

CHAPTER 4

***4.1*:**

a. 12E
b. 600 kW

***4.2*:**

a. $\frac{jL}{\kappa_\mathrm{s}}$
b. $x_\mathrm{d} = \frac{jt}{q}$
c. $\Delta\phi_\mathrm{d} = \frac{jx_\mathrm{d}}{\kappa_\mathrm{d}} = \frac{j^2 t}{q\kappa_\mathrm{d}}$
d. $V_\mathrm{eq} - \frac{jL_\mathrm{s}}{\kappa_\mathrm{s}} - \frac{j^2 t}{q\kappa_\mathrm{d}}$

e. $jV_{\mathrm{eq}}t - \frac{j^2 L_{\mathrm{s}}}{\kappa_{\mathrm{s}}}t - \frac{j^3}{2q\kappa_{\mathrm{d}}}t^2$

f. $\frac{V_{\mathrm{eq}}\kappa_{\mathrm{d}}}{j} - L_{\mathrm{s}}\frac{\kappa_{\mathrm{d}}}{\kappa_{\mathrm{s}}}$

***4.3*:**

a. 0.01 A

b. 75%

CHAPTER 5

***5.1*:**

a. $\frac{4FDc_L}{L}$

b. 13 $\mathrm{A/cm^2}$

c. $\frac{k_1 k_2}{k_1 + k_2}$

d. $\frac{nFc_L}{1/k + L/D}$

***5.2*:**

a. $\frac{\mathrm{d}s}{\mathrm{d}x} = -\frac{\lambda}{p_{\mathrm{t}}K}\left(\frac{\mu_{\mathrm{g}}U_{\mathrm{g}}}{(1-s)^3} + \frac{\mu U_{\mathrm{l}}}{s^3}\right)$

b. $\frac{1}{1+(\mu_{\mathrm{g}}\mathcal{V}_{\mathrm{m,g}}/2\mu\mathcal{V}_{\mathrm{m,l}})^{1/3}} \approx 0.36$

***5.3*:**

a. $3\varphi/R$

b. 0.12 $\mathrm{A/cm^3}$

c. 0.49 V

d. $b\ln(10)$

e. 0.2

CHAPTER 6

***6.1*:**

a. $\frac{nFl}{j\mathcal{V}_{\mathrm{m}}}\frac{\varepsilon_{\mathrm{c}}}{1-\varepsilon_{\mathrm{c}}/\varepsilon_{\max}}(w_{\mathrm{S}} + W_{\mathrm{l}})$

b. 0.7 m

***6.2*:**

a. $\frac{jl}{\kappa_{\mathrm{m}}(1-\varepsilon)^2}$

b. $\frac{jl}{\kappa_{\mathrm{m}}}\left(1 + \frac{h}{z_{\mathrm{c}}}\right)$

c. $\frac{j^2 l}{\kappa_\mathrm{m}} \frac{h}{z_\mathrm{c}} A$

d. $j \left(\frac{l h^2}{24 \mu \kappa_\mathrm{m}} \frac{\mathcal{V}_m}{nF} \right)^{1/3}$

e. 2.4 m/s

***6.3*:**

a. $j\mathcal{V}_\mathrm{m}/nF$

b. $j\mathcal{V}_\mathrm{m} z/nF\varepsilon w_\mathrm{g}$

c. 4.3 mm

***6.4*:**

a. $jL/\kappa\epsilon(1-\varepsilon)$

b. $jL/2b\kappa\epsilon(1-\varepsilon)$

c. 0.57

d. $b \ln\left(\frac{1}{1-\varepsilon}\right)$

CHAPTER 7

***7.1*:**

a. 0.11

b. 0.215

c. 0.22 m/s

d. $1 - 0.01^N$

***7.2*:** 7.6 cm/s

***7.3*:**

a. $c_\mathrm{w} + \frac{\langle w \rangle l^2}{hD} \left(\left(\frac{x}{l}\right)^2 \left(1 - \frac{x}{2l}\right) - 1 \right) \frac{\partial c}{\partial \bar{z}} \frac{x}{l}$

b. $35/13 \approx 2.7$

CHAPTER 8

***8.2*:**

a. To a rough approximation we can use $\mathcal{E}_\mathrm{a} \sim \frac{1}{1+j/J_D}$, where $J_D = nFD_\mathrm{agg}c/R$. With $n = 4$ electrons per oxygen molecule $j/J_D = 26$ so $\mathcal{E}_\mathrm{a} \sim 0.04$.

b. Conservation of oxygen volume gives $\langle w \rangle = jh/nFlc_\mathrm{in}$. Using the ideal gas law gives $c_\mathrm{in} = fp/\mathcal{R}T = 8.6\ \mathrm{mol/m^3}$ so $\langle w \rangle = 0.3$ m/s.

c. The assumed high velocity makes the channel concentration approximately constant and equal to c_{in}. Adding the mass transfer resistances of the channel and diffusion layers in series gives $j_{\text{lim}} = \frac{nFc_{\text{in}}}{l_{\text{d}}/D_{\text{d}} + l/\text{Sh}D_{\text{m}}}$. Using the effective diffusion layer diffusivity $D_{\text{d}} = D_{\text{m}}\epsilon_{\text{d}}/\tau^2 \approx 9.4 \cdot 10^{-6}$ m^2/s gives $j_{\text{lim}} = 4 \cdot 10^4$ A/m^2.

***8.3*:**

a. Follow a path through the 'channels' in between the solid from left to right until the pattern repeats. This gives a horizontal distance $l = 20$ μm and a vertical translation of 5 μm up and 5 μm down so that the total distance covered is $l_{\parallel} = 30$ μm and $\tau = l_{\parallel}/l = 1.5$.

b. Considering a repetitive unit cell of cross-sectional area $A = 100$ μm^2 around one solid 'beam' of depth 1 m, the cross-sectional pore area $A_{\text{pore}} = 8$ μm $\times 4$ μm $= 32$ μm$^2 + 4 \times 1$ μm$^2 = 36$ μm^2, so that $\epsilon = A_{\text{pore}}/A = 0.36$.

c. Bruggeman's approximation asserts that $\tau^2 \approx \epsilon^{-\mathcal{B}}$ with $\mathcal{B} = 1/2$ for a random arrangement of polydisperse spheres or $\mathcal{B} = 1$ for cylinders. Neither of these results describes our answers at (a) and (b), which is also not expected. We find $\mathcal{B} \approx 0.8$, somewhere in between the result for spheres and cylinders.

d. In the direction parallel to the beam-like structure, the tortuosity $\tau = 1$ is lower, giving a higher effective diffusion coefficient, which is proportional to ε/τ^2. Therefore, a higher diffusion flux can be obtained with equal concentration gradient.

e. The unit cell considered at (b) has a surface area $A_{\text{s}} = 4 \times 8$ μm $\times 1$ m $= 32 \cdot 10^{-6}$ m^2 and a volume $V = A \times 1$ m $= 1 \cdot 10^{-10}$ m^3 so $a = A_{\text{s}}/V = 3.2 \cdot 10^5$ m^{-1}.

***8.4*:**

a. The immobile cation satisfies $N_+ = -D_+\left(\frac{\text{d}c}{\text{d}x} + c\frac{F}{\mathcal{R}T}\frac{\text{d}\phi}{\text{d}x}\right) = 0$, where ϕ is the electrolyte potential. The concentration thus satisfies a Boltzmann distribution $c \propto \text{e}^{\frac{F}{\mathcal{R}T}\phi}$. Therefore, the potential drop $\Delta\phi = \frac{\mathcal{R}T}{F}\Delta \ln c = \frac{\mathcal{R}T}{F}\ln\frac{c_{\text{c}}}{c_{\text{a}}}$, with c_{a} and c_{c} the electrolyte concentration at the anode and cathode, respectively. Since there is no reaction between the electrodes, the concentration profile varies linearly in space. At the limiting current density $c_{\text{a}} = 0$ at the anode, where the OH^- is consumed. At the cathode, where OH^- is produced, $c_{\text{c}} = 0.2$ M in order to give the average $c = 0.1$ M. At 80 % of the limiting current density, the concentration gradient will be 80 % of that at the limiting current density so $c_{\text{a}} = 0.02$ M and $c_{\text{c}} = 0.18$ M and $\Delta\phi = 0.02$ V.

b. Due to the high supporting electrolyte concentration we use Ohm's law to write $\Delta\phi = \frac{j_{\text{lim}}l}{\kappa}$. The limiting current density reads $j_{\text{lim}} = \frac{nFD_-\Delta c}{l}$. With $n = 1$ electrons per OH^- and $\Delta c = 0.2$ M this gives $j_{\text{lim}} = 7.7 \cdot 10^3$ A/m^2. The conductivity $\kappa = \frac{F^2}{\mathcal{R}T}\sum z_i^2 D_i c_i \approx 7.6$ S/m, using $z_i^2 = 1$ and $D_i = 10^{-9}$ m^2/s of the supporting electrolyte. This gives $\Delta\phi \approx 10^{-2}$ V.

***8.5*:**

The assumption of a thin reaction layer in the moving reaction zone model requires an effectiveness factor $\mathcal{E} \ll 1$. Assuming Tafel kinetics, this requires a high current density $j \gg J_\kappa = \kappa b/L$, where κ is the effective electrode conductivity, b the Tafel slope, and L the electrode thickness.

The single particle model assumes a constant overpotential and reactant concentration throughout the electrode, so $\mathcal{E} \approx 1$. A constant overpotential requires $j \ll J_\kappa$. A constant reactant concentration requires $j \ll j_D = nFDc_0/L$, where n is the number of electrons per reactant molecule, D the effective reactant diffusivity, and c_0 the reactant concentration at the 'entrance' of the electrode. For a reacting binary electrolyte these two criteria are related.

***8.6*:**

a. The exponentials in the concentration-independent Butler-Volmer equation $j_\perp = j_* \left(\mathrm{e}^{\frac{\alpha F \eta}{\mathcal{R}T}} - \mathrm{e}^{-\frac{(1-\alpha)F\eta}{\mathcal{R}T}} \right)$ can be linearized if their arguments $\frac{\alpha F\eta}{\mathcal{R}T}, \frac{(1-\alpha)F\eta}{\mathcal{R}T} \ll 1$. In this case $j_\perp$ becomes proportional to η.

b. Using the leading-order series expansion $\mathrm{e}^x \approx 1 + x$ for $x \ll 1$ gives $j_\perp \approx \eta/AR$ with $AR = \frac{\mathcal{R}T}{j_* F}$.

***8.7*:**

a. Neglecting friction in the downcomer, the hydrostatic pressure difference between top and bottom $\rho_\mathrm{l} g h$ equals that between the top and bottom of the riser $\rho_\mathrm{l}(1 - \langle\varepsilon\rangle)\, gh + 12\mu \frac{W_\mathrm{l}}{l^2}$ so that $W_\mathrm{l} = \rho_\mathrm{l}\langle\varepsilon\rangle g h l^2/12$. Neglecting slip, at very low gas fractions $\varepsilon = \frac{W_\mathrm{g}}{w_\mathrm{s} + W_\mathrm{l} + W_\mathrm{g}/\varepsilon_\mathrm{m}} \approx \frac{W_\mathrm{g}}{W_\mathrm{l}}$. We thus find that $W_\mathrm{l} \propto \langle\varepsilon\rangle \propto W_\mathrm{g}/W_\mathrm{l}$ so $W_\mathrm{l} \propto \sqrt{W_\mathrm{g}} \propto \sqrt{j}$. Because the bubbles escape faster with increasing liquid velocity, the driving force for natural recirculation is reduced with increasing liquid flow.

b. Viscous friction in the downcomer decreases W_l. Since $\varepsilon \approx W_\mathrm{g}/W_\mathrm{l}$, this will increase the gas fraction. A lower liquid velocity will transport less gas, increasing the gas fraction near the electrodes.

***8.8*:**

For concentration-independent Tafel kinetics $\eta_0 = b \ln\left(\frac{j}{\mathcal{E} J_*}\right)$ where $J_* = a l j_*$ and, allowing for ohmic limitations, the effectiveness factor $\mathcal{E} \sim \frac{1}{1 + 2j/J_\kappa}$, with $J_\kappa = \kappa b/L$. Therefore,

$$\eta_0 \approx \begin{cases} b \ln\left(\frac{j}{J_*}\right) & j \ll J_\kappa \\ b \ln\left(\frac{j^2}{2 J_* L \kappa b}\right) = 2b \ln\left(\frac{j}{\sqrt{2 J_* L \kappa b}}\right) & j \gg J_\kappa \end{cases} \tag{8.1}$$

From these limits we see that the Tafel slope $\frac{\partial \eta_0}{\partial \ln j}$ doubles from b when $j \ll J_\kappa$ to $2b$ when $j \gg J_\kappa$.

At high current densities, the effectiveness factor $\mathcal{E} \approx 2\kappa b/jL$ becomes inversely proportional to j since ohmic resistance makes the activation overpotential η decrease over a penetration-depth inversely proportional to j. Therefore, the effectively available reactive surface area, or $J_*\mathcal{E}$, decreases inversely proportional to j, causing the doubling in the Tafel slope.

Chapter 9

Formula sheet

Constants

Faraday's constant $F = 96485$ C/mol, Elementary charge $e = 1.60217662 \cdot 10^{-19}$ C, Gas constant $\mathcal{R} = 8.314$ J/mol/K.

Formulas

$$j_\perp = nFN_\perp \qquad \text{Faraday's law} \qquad (1.19)$$

$$j_\perp = j_* \left(\frac{c_\mathrm{R}}{c_\mathrm{R,eq}} \mathrm{e}^{\frac{\alpha_O F\eta}{\mathcal{R}T}} - \frac{c_\mathrm{O}}{c_\mathrm{O,eq}} \mathrm{e}^{-\frac{\alpha_R F\eta}{\mathcal{R}T}} \right) \qquad \text{Butler-Volmer equation} \qquad (1.27)$$

$$V_\mathrm{cell} = V_\mathrm{eq} + \eta_\mathrm{c} - \eta_\mathrm{a} - \Delta\phi - \Delta V \qquad \text{Cell voltage} \qquad (1.35)$$

$$\boldsymbol{N}_i = c_i \boldsymbol{u} - D_i \left(\nabla c_i + z_i c_i \frac{F}{\mathcal{R}T} \nabla\phi \right) \qquad \text{Nernst-Planck} \qquad (2.25)$$

$$\kappa = \frac{F^2}{\mathcal{R}T} \sum z_i^2 D_i c_i \qquad \text{Ionic conductivity} \qquad (2.31)$$

$$D_\mathrm{a} \equiv t_- D_+ + t_+ D_- = \frac{2D_+ D_-}{D_+ + D_-} \qquad \text{Ambipolar diffusivity} \qquad (2.42)$$

$$k_\mathrm{m0} = \sqrt{\frac{\pi D}{4t}}, \quad k_\mathrm{m\infty} = \frac{5D}{R} \qquad \text{Sand's / developed spherical} \qquad (2.57)$$

$$\frac{\partial \epsilon c}{\partial t} = -\nabla \cdot \boldsymbol{N} + aN_\perp \qquad \text{Conservation equation} \qquad (3.15)$$

$$\mathcal{E} \approx \frac{1}{1 + j/J_D + j/2J_\kappa} \qquad \text{Effectiveness factor} \qquad (3.67)$$

$$\frac{\langle C\rangle}{C_{\max}} = \mathrm{e}^{-\int \frac{a_{\mathrm{S}}}{1/k+1/k_{\mathrm{m}}}dt} \qquad \text{SOC single battery particle} \qquad (4.24)$$

$$p_{\mathrm{c}} = p_{\mathrm{l}} - p_{\mathrm{g}} = \frac{2\gamma\cos\vartheta}{r} \qquad \text{Laplace} \qquad (5.5)$$

$$-\frac{\mathrm{d}p_{\mathrm{l}}}{\mathrm{d}x} = \frac{\mu U_{\mathrm{l}}}{Kk} \qquad \text{Darcy} \qquad (5.11)$$

$$\frac{\mathrm{d}s}{\mathrm{d}x} = -\frac{\lambda\mu}{p_{\mathrm{t}}K}\frac{U_{\mathrm{l}}}{s^3}, \qquad \text{Water saturation neglecting } p'_{\mathrm{g}} \qquad (5.13)$$

$$F_D = 3\pi\mu d\left(w_{\mathrm{g}} - w_{\mathrm{l}}\right) \qquad \text{Stokes drag force} \qquad (6.4)$$

$$\varepsilon = \frac{W_{\mathrm{g}}}{w_{\mathrm{S}} + W_{\mathrm{l}} + W_{\mathrm{g}}/\varepsilon_{\mathrm{m}}} \qquad \text{Bubble gas fraction} \qquad (6.9)$$

$$\Delta p_{\mathrm{f}} = \frac{12\mu W_{\mathrm{l}}}{l^2}h \qquad \text{Planar Hagen-Poiseuille} \qquad (7.9)$$

$$\eta_0 = b\ln\left(\frac{j/\mathcal{E}J_*}{\frac{c_{\mathrm{m}}}{c_{\mathrm{in}}}(1-j/j_{\mathrm{lim}})}\right) \qquad \text{Activation overpotential} \qquad (7.27)$$

The porous electrode equations, associated with the characteristic current densities $J_D = nFDc_0/L$, $J_\kappa = b\kappa/L$, and $J_* = aLj_*$, respectively

$$c' = i/nFD \qquad (3.44)$$

$$\eta' = i/\kappa \qquad (3.45)$$

$$i' = aj_*\frac{c}{c_0}\mathrm{e}^{\eta/b} \qquad (3.46)$$

Not in the formula sheet

The above equations represent a selection of what may be considered the most important formulas of this book. However, there are many relevant equations not given here, either because they are assumed to be widely known, should be learned by heart, or can be derived from the above. Here, we will consider these categories in some detail.

Assumed background knowledge

This category includes, for example, the area (πd^2) and volume ($\pi d^3/6$) of a sphere of diameter d, the ideal gas law ($p\mathcal{V}_\mathrm{m} = \mathcal{R}T$), Ohm's law ($\boldsymbol{i} = \kappa \boldsymbol{E}$), the buoyancy force ($F_\mathrm{b} = \rho g \mathcal{V}$) on a volume $\mathcal{V}$, a general conservation equation ($\frac{\partial c}{\partial t} = -\nabla \cdot \boldsymbol{N} + S$), an advection-diffusion equation ($\frac{\partial c}{\partial t} + \boldsymbol{u} \cdot \nabla c = D\nabla^2 c$), and the hydrostatic pressure $p_\mathrm{h} \approx (1-\varepsilon)\rho g h$.

Memorise from this course

Things that should be memorised include the conventions and definitions discussed at the end of the Nomenclature section, or in section 4.1.2, the definition of an activation overpotential ($\eta = \left(E - \phi\right) - \left(E - \phi\right)_\mathrm{eq}$), Bruggeman's relation $\tau^2 \approx \epsilon^{-1/2}$ for spheres and $\tau^2 \approx \epsilon^{-1}$ for cylinders, some relations like $\alpha_O + \alpha_R = 1$, the definition of energy/voltage efficiency $\varphi_\mathrm{e} = V_\mathrm{cell}/V_\mathrm{eq}$ for Galvanic or $\varphi_\mathrm{e} = V_\mathrm{eq}/V_\mathrm{cell}$ for electrolytic cells, and:

$$\boldsymbol{i} = \sum z_i F \boldsymbol{N}_i \qquad \text{Ionic current density} \qquad (2.28)$$

$$\eta_0 = b\ln\left(\frac{j}{J_*\mathcal{E}}\right), \qquad \text{Overpotential entrance porous electrode} \qquad (3.42)$$

$$\mathcal{E} \approx \frac{1}{1 + j/J_D + j/2J_\kappa} \qquad \text{Effectiveness factor} \qquad (3.67)$$

$$N_\perp = kc^\nu \qquad \text{Reaction of order } \nu \qquad (1.20)$$

$$D = \frac{\epsilon}{\tau^2} D_\mathrm{m} \qquad \text{Effective transport coefficients} \qquad (3.11)$$

$$a = (1-\epsilon)\, a_\mathrm{s} \qquad \text{volumetric surface area} \qquad (3.4)$$

$$0 = -\nabla \cdot \boldsymbol{i} - a j_\perp \qquad \text{Charge conservation} \qquad (3.19)$$

Inserting Eq. (3.67) in Eq. (3.42) gives

$$\eta_0 \approx 2b\ln\left(\frac{j}{\sqrt{\frac{a j_*}{\frac{1}{2\kappa b} + \frac{1}{nFDc_0}}}}\right). \qquad (3.69)$$

The expression for the effectiveness factor can also be derived from the formulas in the formula sheet,[1] but it may be easier to memorise these. In the next paragraph we will consider a few relations that can be derived from the formula sheet, so do not necessarily have to be memorised.

Derive from the formula sheet

- From the Nernst-Planck equation (2.25), you can derive the advection-diffusion flux for neutral particles $\boldsymbol{N} = \boldsymbol{u}c - D\nabla c$, Ohm's law $\boldsymbol{i} = -\kappa\nabla\phi$, the ionic conductivity $\kappa = \frac{F^2}{\mathcal{R}T}\sum z_i^2 D_i c_i$, and the Boltzmann distribution ($c \propto \mathrm{e}^{-z_i F\phi/\mathcal{R}T}$ for a zero-flux ion i).
- From Faraday's and Fick's law $N_\perp = D\Delta c/\delta$, the limiting current density $j_{\mathrm{lim}} = D\Delta c/nF\delta$ follows. From Sand's equation (2.57) we find the mass transfer coefficient of a growing boundary layer as $k_{\mathrm{m}} \equiv N_\perp/\Delta c = D/\delta = \sqrt{\pi D/4t}$, which is Eq. (4.19).
- The Stokes rise velocity $w_{\mathrm{S}} = \rho g d^2/18\mu$ follows from equating $F_{\mathrm{b}} = \rho g \pi d^3/6$ to the Stokes drag force, which is valid for $\rho w_{\mathrm{S}} d/\mu \lesssim 1$.
- The state-of-charge of a battery particle $S_{\mathrm{oC}} = \frac{\langle C\rangle}{C_{\mathrm{max}}}$ is provided, including $k_{\mathrm{m}} = N_\perp/(C_{\mathrm{max}} - \langle C\rangle)$ for small and large values of time. The first-order reaction rate coefficient k can be obtained as $k = N_\perp/c = j_* \mathrm{e}^{\eta/b}/nF$ for concentration-dependent Tafel kinetics.
- From the Butler-Volmer equation (1.27) you can derive the equations for concentration-independent Butler-Volmer kinetics $j_\perp = j_*\left(\mathrm{e}^{\frac{\alpha_O F\eta}{\mathcal{R}T}} - \mathrm{e}^{-\frac{\alpha_R F\eta}{\mathcal{R}T}}\right)$, symmetric kinetics $\eta = b\,\mathrm{asinh}\left(\frac{j_\perp}{2j_*}\right)$, Tafel kinetics $j_\perp = j_*\frac{c}{c_0}\mathrm{e}^{\eta/b}$, and concentration-independent linear kinetics $j_\perp = j_* F\eta/\mathcal{R}T$ [2], and the Nernst equation $V_{\mathrm{eq}} = \phi_{\mathrm{eq}} + \frac{\mathcal{R}T}{F}\ln\left(\frac{k_O c_{\mathrm{R,eq}}}{k_R c_{\mathrm{O,eq}}}\right)$. For concentration-dependent Tafel expressions for the activation and concentration-overpotential follow as

$$\eta = b\ln\left(\frac{j}{j_*}\frac{c_{\mathrm{eq}}}{c}\right) = b\ln\left(\frac{j}{j_*}\right) + b\ln\left(\frac{c_{\mathrm{eq}}}{c}\right). \tag{2.10}$$

[1] Taking the derivative of the porous electrode equation Eq. (3.B.96) with respect to x and inserting Eq. (3.B.97) gives $\mathrm{d}^2c/\mathrm{d}(x/L)^2 = \mathrm{M}^2 c$ with $\mathrm{M}^2 = J_*\mathrm{e}^{\eta/b}/J_D$ which for constant $\mathrm{M}^2 \gg 1$ leads to the solution $c = c_0\mathrm{e}^{-\mathrm{M}x/L}$ with effectiveness factor $\mathcal{E} = \frac{\langle c\rangle}{c_0} = \frac{1}{\mathrm{M}} = \frac{J_D}{j}$ using Eq. (3.42). For ohmic limitations $\mathrm{M} \approx j/2J_\kappa$ and for a binary electrolyte $\mathrm{M} = \frac{1+r+\alpha}{2}\frac{j}{J_D}$.

[2] Using for small arguments $\mathrm{e}^{\frac{\alpha_O F\eta}{\mathcal{R}T}} \approx 1 + \frac{\alpha_O F\eta}{\mathcal{R}T}$ and using $\alpha_O + \alpha_R = 1$.

Index

Bibliography

[1] J. B. Allen and R. F. Larry. *Electrochemical methods fundamentals and applications*. John Wiley & Sons, 2001.

[2] L. G. Austin. Tafel slopes for flooded diffusion electrodes. *Transactions of the Faraday Society*, 60:1319–1324, 1964.

[3] A. J. Bard, L. R. Faulkner, and H. S. White. *Electrochemical methods: fundamentals and applications*. John Wiley & Sons, 2022.

[4] M. Z. Bazant. Electrochemical Energy Systems, Massachusetts Institute of Technology: MIT OpenCourseWare. https://ocw.mit.edu/. License: Creative Commons BY-NC-SA., 2014. Accessed: 2021.

[5] A. Bhadra and J. W. Haverkort. The optimal electrode pore size and channel width in electrochemical flow cells. *Journal of Power Sources*, 579:233240, 2023.

[6] P. M. Biesheuvel, S. Porada, and J. E. Dykstra. The difference between faradaic and non-faradaic electrode processes. *arXiv preprint arXiv:1809.02930*, 2018.

[7] E. L. J. Coenen and L. J. J. Janssen. Voidage of bulk solution in a tall vertical gasevolving cell. *Journal of applied electrochemistry*, 27(10):1143–1148, 1997.

[8] COMSOL Multiphysics (R) v. 6.2.

[9] Effective diffusivity in porous materials, application id: 978. https://www.comsol.nl/model/effective-diffusivity-in-porous-materials-978. Accessed: 2021.

[10] M. Doyle, T. F. Fuller, and J. Newman. Modeling of galvanostatic charge and discharge of the lithium/polymer/insertion cell. *Journal of the Electrochemical society*, 140(6):1526, 1993.

[11] N. Epstein. On tortuosity and the tortuosity factor in flow and diffusion through porous media. *Chemical engineering science*, 44(3):777–779, 1989.

[12] T. F. Fuller and J. N. Harb. *Electrochemical engineering*. John Wiley & Sons, 2018.

[13] J. W. Haverkort. A theoretical analysis of the optimal electrode thickness and porosity. *Electrochimica Acta*, 295:846–860, 2019.

[14] A. A. Kulikovsky. How important is oxygen transport in agglomerates in a pem fuel cell catalyst layer? *Electrochimica Acta*, 130:826–829, 2014.

[15] A. A. Kulikovsky. *Analytical modelling of fuel cells*. Elsevier, 2019.

[16] C. Lamy and P. Millet. A critical review on the definitions used to calculate the energy efficiency coefficients of water electrolysis cells working under near ambient temperature conditions. *Journal of power sources*, 447:227350, 2020.

[17] X. Liu, F. Peng, G. Lou, and Z. Wen. Liquid water transport characteristics of porous diffusion media in polymer electrolyte membrane fuel cells: A review. *Journal of Power Sources*, 299:85–96, 2015.

[18] T. Maoka. Electrochemical reduction of oxygen on small platinum particles supported on carbon in concentrated phosphoric acid—i. effects of platinum content in the catalyst layer and operating temperature of the electrode. *Electrochimica acta*, 33(3):371–377, 1988.

[19] N. Nagai, M. Takeuchi, T. Kimura, and T. Oka. Existence of optimum space between electrodes on hydrogen production by water electrolysis. *International journal of hydrogen energy*, 28(1):35–41, 2003.

[20] R. Parsons. General equations for the kinetics of electrode processes. *Transactions of the Faraday Society*, 47:1332–1344, 1951.

[21] M. L. Perry, J. Newman, and E. J. Cairns. Mass transport in gas-diffusion electrodes: a diagnostic tool for fuel-cell cathodes. *Journal of the Electrochemical Society*, 145(1):5, 1998.

[22] D. G. L. Plett. ECE4710/5710: Modeling, Simulation, and Identification of Battery Dynamics, 2019.

[23] T. Shinagawa, A. T. Garcia-Esparza, and K. Takanabe. Insight on tafel slopes from a microkinetic analysis of aqueous electrocatalysis for energy conversion. *Scientific reports*, 5(1):13801, 2015.

[24] P. J. Sides. Phenomena and effects of electrolytic gas evolution. In *Modern aspects of electrochemistry*, pages 303–354. Springer, 1986.

[25] K. Stephan. *Heat transfer in condensation and boiling*. Springer, 1992.

[26] M. E. Suss, K. Conforti, L. Gilson, C. R. Buie, and M. Z. Bazant. Membraneless flow battery leveraging flow-through heterogeneous porous media for improved power density and reduced crossover. *RSC advances*, 6(102):100209–100213, 2016.

[27] W. Tiedemann and J. Newman. Maximum effective capacity in an ohmically limited porous electrode. *Journal of The Electrochemical Society*, 122(11):1482, 1975.

[28] B. Tjaden, S. J. Cooper, D. J. L. Brett, D. Kramer, and P. R. Shearing. On the origin and application of the bruggeman correlation for analysing transport phenomena in electrochemical systems. *Current Opinion in Chemical Engineering*, 12:44–51, 2016.

[29] C. W. Tobias. Effect of gas evolution on current distribution and ohmic resistance in electrolyzers. *Journal of the Electrochemical society*, 106(9):833, 1959.

[30] B. Vijayaraghavan, D. R. Ely, Y.-M. Chiang, R. García-García, and R. E. García. An analytical method to determine tortuosity in rechargeable battery electrodes. *Journal of The Electrochemical Society*, 159(5):A548, 2012.

[31] F. Y. Zhang, X. G. Yang, and C. Y. Wang. Liquid water removal from a polymer electrolyte fuel cell. *Journal of the Electrochemical Society*, 153(2):A225, 2005.

Electrolysers, Fuel Cells and Batteries:
Analytical modelling

J.W. Haverkort

Electrochemical engineering deals with electrochemical devices like electrolysers, fuel cells, and batteries. While several excellent books exist in this long-standing and still growing field, their focus is usually on chemistry or phenomenology. In this textbook, we focus on mathematical modelling of the physical phenomena involved. Instead of resorting to numerical modelling, the aim is to derive simplified analytical models that maximise understanding.

Porous electrodes, ion mass transport, and multiphase flow are central themes in this book. Examples include modelling the water saturation in a fuel cell diffusion layer, the gas fraction and current distribution in an alkaline water electrolyser, the potential distribution in a binary electrolyte inside a porous battery electrode, and the concentration distribution in the flow channel of a redox flow battery. This makes for a diverse, challenging, and stimulating journey, for both students and researchers.

J.W. (Willem) Haverkort
Delft University of Technology, Faculty of Mechanical Engineering

After a PhD in computational nuclear fusion plasma physics, I worked for several years in industry, researching a wide variety of fluid flow phenomena. Presently, I am an associate professor at Delft University of Technology. In our group we work on theoretical, computational, and experimental research, increasingly centred around multiphase flow aspects of alkaline water electrolysis.

TU Delft

ISBN 978-94-6366-855-2
DOI https://doi.org/10.59490/tb.93
textbooks.open.tudelft.nl

Cover image:
Current and potential distribution near a gas-evolving zero-gap electrode, made with COMSOL Multiphysics® by W.L. v.d. Does